High-fidelity Simulations of Rotating Detonation Engines

by

Takuma Sato

A dissertation submitted in partial fulfillment
of the requirements for the degree of
Doctor of Philosophy
(Aerospace Engineering)
in The University of Michigan
2020

Doctoral Committee:

Professor Venkat Raman, Chair
Assistant Professor Jesse Capecelatro
Professor James F. Driscoll
Associate Professor Mirko Gamba

Takuma Sato

takusato@umich.edu

ORCID iD: 0000-0002-5286-0729

ACKNOWLEDGEMENTS

First of all, I would like to thank my advisor, Professor Venkat Raman, for giving me this opportunity at the University of Michigan. I have learned a lot not only the technical skills on the computational fluid dynamics but also an attitude as a professional researcher/engineer. I am glad that we have lead the project to the current state from scratch and this project became one of the main project in the group.

I also would like to thank my committee members Professor Gamba, Professor Driscoll, and Professor Capecelatro for reviewing my thesis and providing constructive comments to improve.

Furthermore, I would like to thank Professor Gamba's experimental group, Professor Gamba, Fabian, Logan, and Alex. I believe that our collaboration made the progress in the past few years possible although there are still a lot of work as future work!

My graduate student colleagues were also instrumental part of my Ph.D program. Alex always helped me how to use supercomputer when I just joined the group. Malik always make him available and showed me how to conduct research systematically. Yihao never hesitated to spend time discussing my research. Supraj learned very quickly about the detonation after he joined this group, and we worked together to push the project forward. Shivam and Supraj were the best drink-fellow on Friday. Negin always answered my questions about immigration matters and Rackham systems. I would like to thank Shivam, Supraj, Ral and Caleb for reviewing the thesis.

Finally, I also wish to thank my family in Japan. My parents are always concerned about my health and my life in the U.S. They always welcomed when I went back home with making my favorite Japanese food. Also, I would like to thank Saki from the bottom of my heart. You have always supported me in the grad school journey and I can never thank you enough.

TABLE OF CONTENTS

CHAPTER

LIST OF FIGURES

Figure

LIST OF TABLES

Table

LIST OF ABBREVIATIONS

RDE Rotating Detonation Engine

FVM Finite Volume Method

U of M University of Michigan

PDE Pulse Detonation Engine

DDT Deflagration to Detonation Transition

CJ Chapman Jouguet

AFRL Air Force Research Laboratory

IPM Induction Parameter Model

MUSCL Monotonic Upstream-centered Scheme for Conservation Laws

HLLC Harten-Lax-van Leer-Contact

RK Runge-Kutta

KNP Kurganov,Noelle and Petrova

ZND Zeldovich, Neumann, Döring

AMR Adaptive Mesh Refinement

CB Contact Burning

PC Parasitic Combustion

BR Buffer Region

CS Contact Surface

CTAP Capillary Tube Average Pressure

R-H Rankine-Hugoniot

ABSTRACT

RDEs have drawn increased attention throughout the world as a viable technique for pressure gain combustion. An annular cylindrical combustor is used to drive a detonation wave azimuthally, which provides a continuous detonation process. RDEs provide a promising route to substantially increasing cycle efficiency compared to traditional cycles because of their ability to use shock-based compression to increase the pressure of the fluid in the combustor. Due to these characteristics, it is expected to bring revolutionary advancements to aviation and aerospace propulsion systems such as rocket engines, ramjet engines, and turbojet engines.

The goal of this dissertation is to provide the RDE community with a comprehensive database of full-scale RDE calculations for a variety of injector designs and operating conditions which enables design teams to make rapid progress for the realization. The main design challenge emerges from a non-premixed feed system where the fuel and oxidizer are injected separately into the combustion chamber. A non-premixed injection scheme is employed not only for safety and controllability, but also for an air-breathing RDE where the air stream will not come from a plenum, but rather through an intake. The main design challenge at this stage is developing a non-premixed fuel feed system that achieves adequate mixing and minimizes pressure losses while ensuring a reliable and safe detonation process. In order to rapidly accelerate such engineering design, comprehensive RDEs physics including chemistry, effects of complex geometry on detonation structures, and the complexity of the injection scheme need to be understood. With this mind, my dissertation will focus on the detailed detonation structure affected by the mixing process with a variety of

injection geometries.

To perform large scale simulations of realistic RDEs geometry, a finite volume method (FVM)-based solver, named as UMdetFOAM, with following three key features is developed in this work: (1) implementation of schemes to reduce dispersive/dissipative errors at the detonation front where a spatial discontinuity exists, (2) the capability of dealing with complex geometries, and (3) the ability to incorporate user-specified chemical kinetics by coupling the FVM solver with a chemistry solver. These large-scale simulations using thousands of cores, validated in conjunction with the experimental group at U of M, provide detailed understanding into the performance of such detonation processes.

One of the main outcomes of this work is the development of a solver that enables the simulation of RDEs with the practical geometry. Furthermore, this dissertation demonstrated the effect of mixing-limited detonations on engine performance by identifying key sources of spurious losses. In particular, it was shown that turbulent mixing of fuel and air control the detonation processes. But, additional mixing with products of detonation can lead to premature ignition and parasitic losses. It was identified that the differential recovery of the injectors is the prime reason for the mixing-induced losses. These features were also found in other experimental studies, which validates the hypothesized flame processes.

CHAPTER I

Emerging Interest in Rotating Detonation Engines (RDEs)

Rotating detonation engines (RDEs) is drawing increased attention throughout the world as a viable technique for pressure gain combustion [1, 11]. An annular cylindrical combustor is used to drive a detonation wave azimuthally, which provides a continuous detonation process. RDEs provide a promising route to substantially increasing cycle efficiency compared to traditional cycles because of their ability to use shock-based compression to increase the pressure of the fluid in the combustor [1, 11]. Due to these characteristics, it is expected to bring revolutionary advancements to aviation and aerospace propulsion systems such as rocket, ramjet and turbojet engines (Fig. 1.1) [3, 12–17].

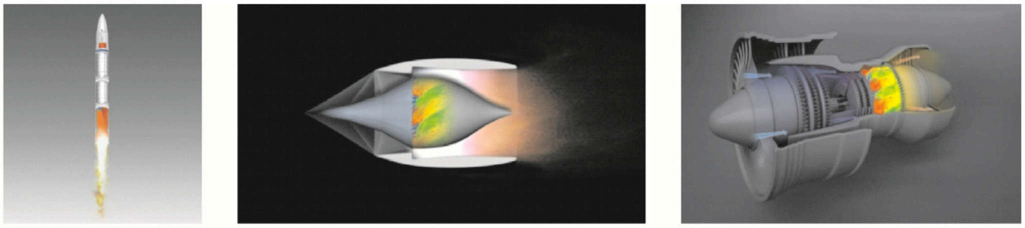

Figure 1.1: Examples of RDEs applications. Figure is reproduced from [1]

1.1 Motivation: Detonation Engines

The gas turbine system is the main energy conversion device for the aviation and power generation sectors. Driven by extensive research and development in the past century, such machines are already operating at near-theoretical limits, and only limited improvements are feasible with the current Brayton cycle based systems [1]. To break the physical constraints for the traditional thermal cycle, the detonation thermal cycle has been emerging as an alternative choice. In the detonation thermal cycle, the reactant gases can get additional compression due to the shock wave that is supported by heat release from chemical reactions [1, 11, 18]. Unlike conventional deflagration-based combustors that are nominally at constant pressure, but might have a small pressure drop, detonation-based devices generate additional compression of the product gases. For this reason, such combustors are classified as pressure gain devices. There are several practical designs of pressure gain devices [1, 19–21]. This includes pulse detonation engines (PDEs, [19]), constant volume combustion [20] and RDEs. For instance, in PDEs, a tube is filled with reactive gases that are sufficiently mixed, and a small spark is introduced from one side of the tube (Fig. 1.2). The spark is converted into a detonation wave through the deflagration to detonation transition process (DDT). The detonation-compressed post-combustion gases are exhausted from the other side of the tube, which is extracted as the thrust of the system. After a certain period of time to exhaust the product gases, the next spark will be introduced by refilling the fresh mixture. Successful PDE applications include development of a rocket system [22]. However, PDEs are inherently limited by the refresh rate, which constrains the operational frequency. In most cases, the thrust is generated intermittently at up to 200 Hz, with a significant fraction of the time gap used to ignite and transition the mixture to detonation conditions [1]. This intermittent thrust is particularly problematic when downstream components such as turbine blades are present. Hence, higher operational frequency is needed to ensure that the pressure gain can be used to effectively extract thrust. The RDE is one such concept and will be the focus of this study.

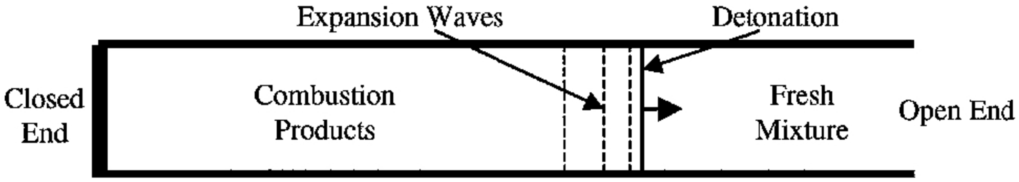

Figure 1.2: Schematic of an idealized PDEs. Figure is reproduced from [2]

1.1.1 Why rotating detonation engines?

Although RDEs were conceptualized many decades ago (including research at UM AERO by Prof. Nicholls in 1960s), recent advancements in gas turbine design and manufacturing technology have made this device a viable option for future propulsion systems [1, 11]. In RDEs, an azimuthally moving detonation wave is sustained in an annular chamber, which is fed fuel and air through ports located at one end of the cylindrical chamber. Because of the sustained waves, the operational mode of the RDE is nearly continuous unlike that of a PDE. As a result, the theoretical operational frequency could be increased to nearly 4 KHz [1].

Figure 1.3 shows the general structure of a realistic RDE configuration. The shock wave (colored by purple) induces chemical reactions in the mixture slightly behind the wave (colored by blue). The product gases (colored by yellow and red) are accelerated and expand towards the exit. Since the detonation wave creates a strong pressure wave that is supported by the chemical reaction, the fuel and air injectors behind the wave may be temporarily blocked, which causes the non-idealities in the combustion process. These non-idealities are associated with: 1) incomplete mixing of fuel/air leading to stratified mixtures encountering the detonation wave; 2) non-constant-volume combustion due to leakage of fuel/air mixture; 3) parasitic combustion, i.e., premature ignition of the mixture and/or stabilization of deflagrations [23]. These

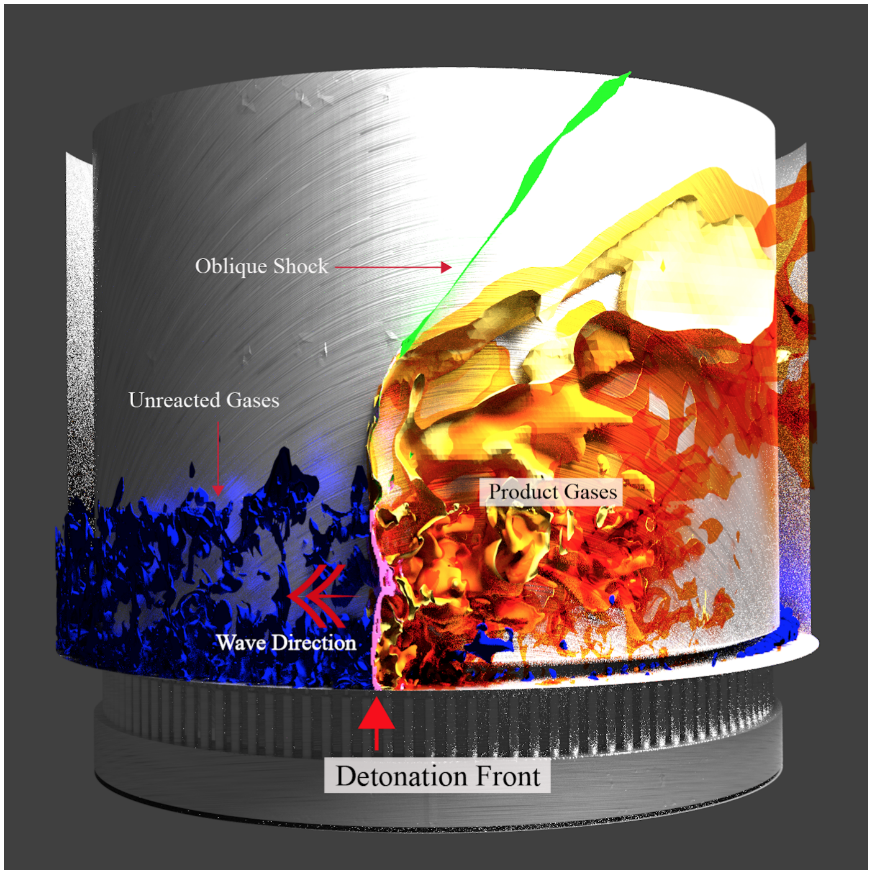

Figure 1.3: A practical RDE configuration showing the detonation wave, the unreacted gases, and the post-detonation product. The figure is generated from simulations described in Chap. 4.

non-idealities have been postulated, and some have been experimentally confirmed [6, 23], but detailed insights into the physical mechanisms that generate such spurious losses are still missing. Without a complete understanding of these loss mechanisms, it will be infeasible to translate RDEs into viable energy conversion devices.

1.1.2 Injection schemes and their effect on RDE performance

One of the main factors that causes the non-idealities is the non-premixed injection scheme. In most RDE systems, fuel and oxidizer enter the detonation chamber separately, which improves safety of operations. Hence, detonation devices inherently depend on fuel-air mixing to achieve stable combustion. As Fig. 1.3 shows, the injection behind the wave is suppressed due to the strong pressure wave. As a result, there is limited time available for fuel-air mixing. In this sense, the RDE operation is limited by the mixing efficiency of the injectors. Prior experimental studies have shown that the incomplete mixing process caused by the stratification of the fuel and the oxidizer could cause a deflagration mode where the wave speed is nearly 50% of the CJ value [5]. Thus, the injector scheme needs to be developed such that a feed system achieves adequate mixing and minimizes pressure losses while ensuring a reliable and safe detonation process. Several injector geometries have been studied, including the radial air inlet, axial air inlet, and staggered fuel and air injector (samples shown in Fig. 1.4). It is reported that all of these types of injectors successfully sustain detonation waves in the chamber [3, 6, 24, 25]. More importantly, it is also found that the injector geometry may affect the detonation structure such as the detonation height, the number of waves and the wave speed [3, 6, 12–17, 24]. With this in mind, determining the non-premixed injection effect on the detonation structure is necessary to accelerate the design optimization process. This aspect will be discussed in Chap. III – VI.

1.1.3 Fuels used in RDEs

When designing RDEs system, another important aspect is the types of the fuel. The induction length needs to be short enough that the reaction attaches behind the shock front, otherwise detonation waves fail to sustain. As prior work shows, hydrogen/air mixture are mostly used in experiments and simulations because of thier high detonability and relatively simpler chemical mechanism. However, practical applications will require hydrocarbon chemistry such as ethylene and natural gas. Prior studies with hydrocarbon reveals that very weak detonation waves are present in the chamber where the wave speed is 50% of the CJ value [5, 26] while the wave speed with hydrogen/air is found to be about 70%. In addition, experiments using

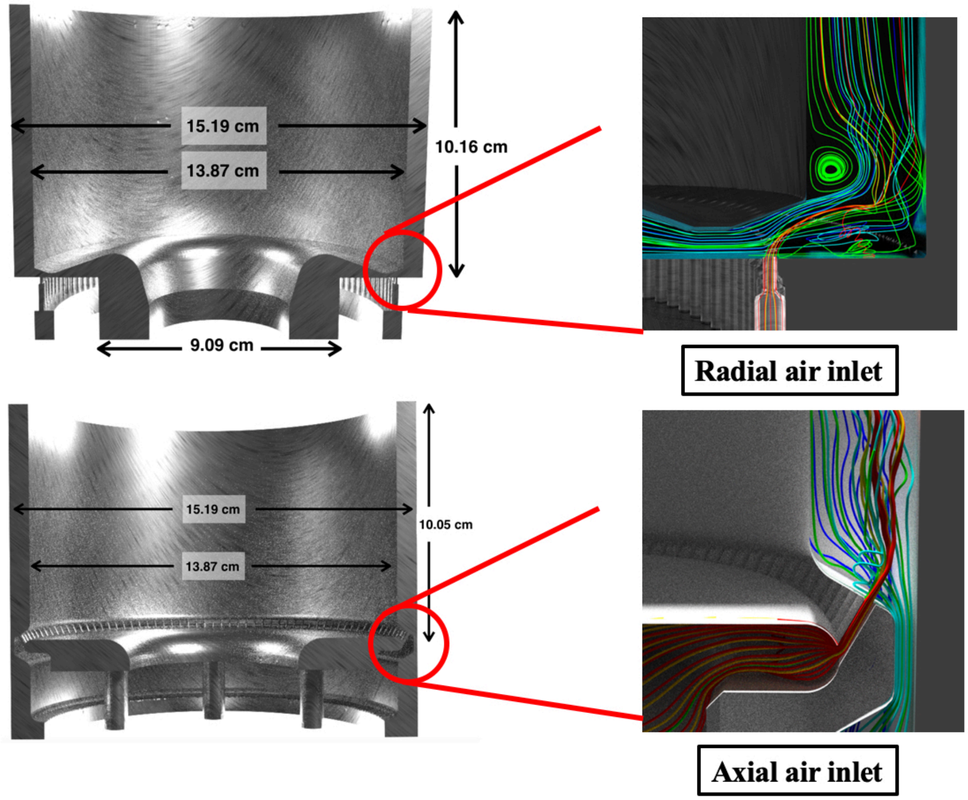

Figure 1.4: Examples of non-premixed injection types employed in RDEs. The meshes for the radial air inlet and axial air inlet are generated by the facilities at the Air force Research Laboratory [3] and the University of Michigan [4], respectively.

ethylene/air reveal a thicker reaction front than that of hydrogen/air (Fig. 1.5,[5]). For methane chemistry, oxygen is typically used as the oxidizer to increase reactivity of the mixture [15, 24]. Both experiments [15] and simulations [24] reveal stable detonation waves in the chamber, although only limited studies are available for methane RDE systems. As such, examining the dynamics depending on the fuel types is critical for the reliable and safe operation of RDEs.

1.2 Prior Research on RDEs

A series of experimental and numerical studies have been conducted in the RDEs community [1, 27]. This section will briefly introduce several studies of relevance to

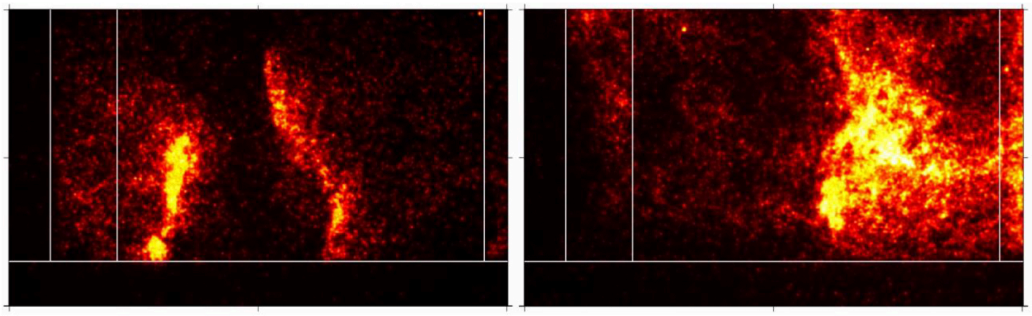

Figure 1.5: OH chemiluminescence of the RDE. Left: hydrogen/air, right: ethylene/air. Reproduced by [5]

the current work.

1.2.0.1 Experimental work

Several research groups have conducted extensive tests of practical RDE configurations [3, 6, 12, 12, 15–17, 24, 26, 28–31]. Air Force Research Laboratory (AFRL) developed a radial injection design, which was used to study RDE characteristics over a wide range of conditions, including mass flow rates, equivalence ratios, fuels, chamber and exit shapes [3, 29, 30, 32]. The AFRL studies included pressure measurements, using sensors located on the detonation chamber wall. Further, they conducted OH chemilumiensence imaging to determine the location of the wave front as a function of time. More recently, the University of Michigan experimental group led by Prof. Gamba[6, 23, 33, 34] conducted extensive studies on an axial air inlet geometry, which is considered the main candidate for translation to practical gas turbines (Fig. 1.6). Their work concluded that the main losses in the RDE are driven by inefficient mixing and inhomogeneous fuel-air mixing, which can cause premature ignition and deflagration in certain regions, while leaving behind unreacted or partially oxidized mixtures in other regions. In all of these studies, the wave velocity was found to be considerably lower than the theoretical Chapman-Jouget (CJ) speed. For instance, the Michigan experiments reported 70% of the peak speed.

For hydrocarbon fuels, Purdue University performed experiments with a high-pressure RDE facility (20 atm for ambient pressure) using methane/oxygen mixture [15]. They concluded that stable detonations were feasible, but the size of the combustion chamber should be larger to support the increased detonation cell size. Moreover, dilution with N_2 was found to decrease detonability, leading to unstable detonation waves. AFRL also performed an ethylene/air-based experiment with the same injector types as that of the hydrogen/air [5]. Similar to the Purdue experiments, it was found that mixture was not easily detonable, and the wave speed was less than 60% of the theoretical speed. Other experiments [26] have confirmed these results. In addition, a variety of low-carbon fuels including syngas mixtures have been tested [16]. Here, increasing hydrogen content ensured stable detonations. Overall, such hydrogen addition seems to be a good strategy for ensuring reliable operation.

A critical feature of this detonation engine is the presence of multiple detonation waves [35]. Depending on the configuration, for the same nominal flow rate, different numbers of waves can also be observed. The number of waves has an important effect on the performance of the device, including heat transfer rates and the magnitude of the pressure pulses traveling upstream and downstream of the combustor in the direction of the flow path. Most importantly, this parameter has a direct impact on combustion efficiency. In a non-premixed RDE, where the fuel and oxidizer enter through separate plenums, a continuous inflow of reactants is necessary to maintain the detonation structure. In particular, the local equivalence ratio should not exhibit very high fluctuations, since this could cause unstable wave propagation with large variations in wave speeds and poor combustion efficiency [36, 37]. The number of waves determines the time available for fuel and air to mix before the arrival of the detonation front. Hence, efficient design requires a method for prediction of this wave structure. In fact, there exists no reliable heuristic for determining the number of waves. While empirical correlations have been developed [38], their accuracy is highly variable.

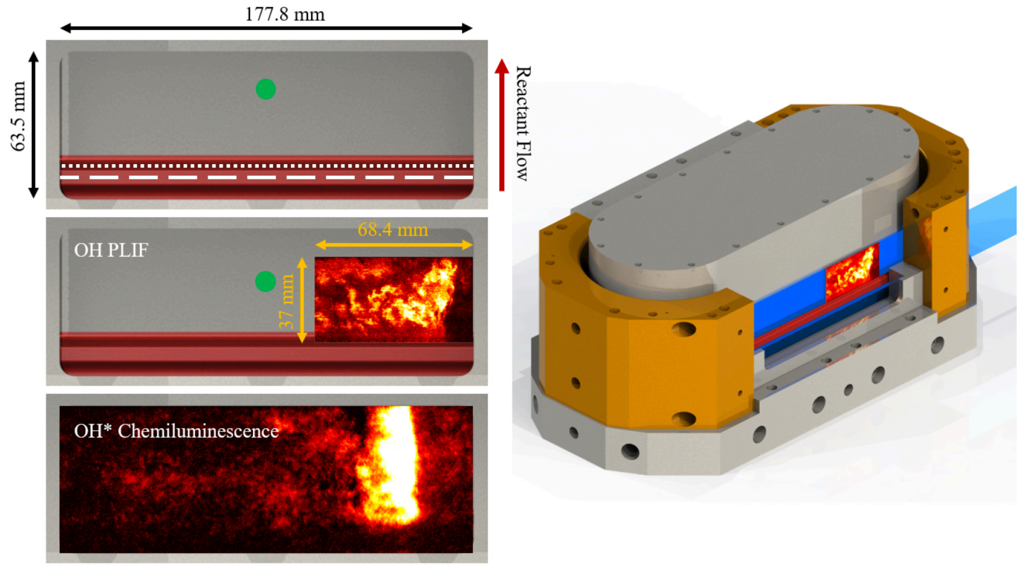

Figure 1.6: The racetrack RDEs facility at the University of Michigan and its OH PLIF visualization. Figure is reproduced from [6]

However, there is one reliable parameter that affects the number of waves, which is the total mass flow rate into the system. In particular, if the global equivalence ratio is kept constant while increasing the mass flow rate, the number of waves increases in almost all configurations studied [3, 16, 38]. A key variable in RDE performance is the refill height, which is essentially the distance the fresh fuel-air mixture penetrates in the axial direction before a detonation wave arrives. It has been hypothesized that when the refill height reaches a critical value, which is dependent on the speed of fuel-air chemistry as parameterized by detonation cell size, the detonation wave splits into two or more waves. Other mechanisms have also been proposed, including the presence of weaker secondary waves that gain strength with increasing mass flow [39].

1.2.0.2 Simulations of RDEs

Numerical simulation of RDEs require that a) the fuel-air mixing , b) the turbulent flow that affects the mixing process and the post-detonation gases, and c) the chemical processes that lead to energy release are all captured accurately. Until very recently, ensuring that all these physical processes are adequately modeled was infeasible. With the growth in computing power, more detailed simulations are starting to emerge. Regardless, full scale simulations, such as the ones to be discussed in this thesis, are still sparse.

Simulation tools for RDEs have increased in complexity with recent advances in computational power and numerical algorithms. There have been many studies of practical RDE configurations [40–42]. These calculations are mainly based on finite-volume or finite-difference techniques, such as the methods applied to detonation-to-deflagration transition [43], and utilize some form of upwinding to stabilize the dispersion errors related to the shock-based discontinuities [44]. In general, combustion kinetics are treated using global rates [45] or the induction parameter model (IPM) [46]. Figure 1.7 shows the general flow field simulated by IPM under an idealized unwrapped two dimensional configuration. This chemical model reduces the computational cost and gives the community the general physics in the RDEs system. For example, it is found that 1) the detonation wave is followed by an oblique shock wave from the top of the wave front, 2) the contact surface is created between freshly burnt gases and the old products, 3) the injection behind the wave front is suppressed due to the compressed gases. Hydrocarbon chemistry is also studied in the same configuration which reveals lower detonability than that of hydrogen chemistry [47].

When using such reduced order kinetics, the resolution requirements are relaxed, and only the shock-based discontinuity needs to be tracked by the mesh. This is achieved using conventional shock-capturing schemes used for high-speed compressible flows [48]. However, the use of detailed chemical kinetics is necessary when mixing is incomplete and the structure of the detonation wave is more complex than that invoked by global chemistry models or the IPM [49]. In this case, the resolution requirements are dictated by the fast chemical reactions, which can lead to very high computational cost.

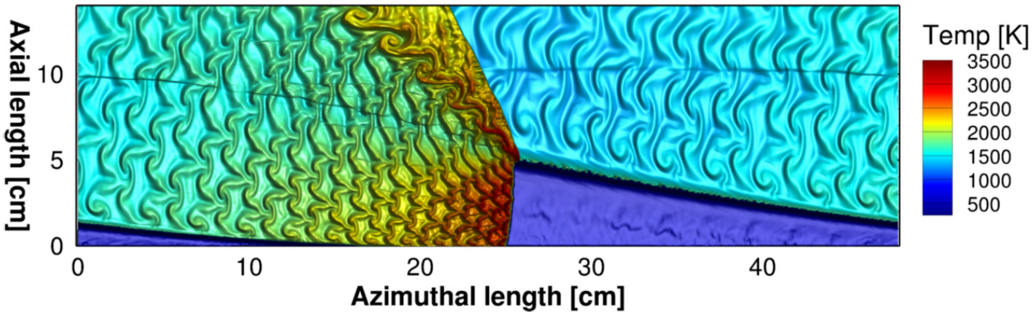

Figure 1.7: Idealized two dimensional RDE calculation. Reproduced by [7]

Computations of full-scale RDE geometries are still sparse [1, 50]. Wang and coworkers [1, 51] have conducted detailed simulations of wave initiation and stabilization but using one-step chemical kinetics with a three dimensional cylinder geometry. More recently, Cocks et al.[52] simulated the Air Force Research Laboratory (AFRL) 6-inch experimental configuration using detailed chemical kinetics and full resolution of the injector sections. This simulation showed that the injector response can affect the nature of the detonation process, but the level of interaction depends on injection and detonation pressures. Yellapantula et al. [53] simulated the same configuration focusing on the detonation chamber, but used an unsteady RANS approach to find that the detonation structure matched experimental OH luminescence images.

1.3 The Importance of the High-fidelity Simulations of RDEs

Despite a series of experimental and numerical studies, as introduced in the last section, much of the detailed physics in RDEs are still unknown. Experimental studies report that the mixing process with a non-premixed injection scheme causes incomplete combustion processes such as parasitic combustion and deflagration that are proved by the lower wave speed compared to the CJ value. More importantly, different types of fuel change the detonability, the injection response process, and the mixing process in the chamber due to the differences in inflow velocities of each flow stream. However, only limited measurements can be done due to the harsh environment in the detonation chamber, where a 30 atm pressure wave propagates at nearly 2000 m/s and 3000 K. While the idealized simulation helps understand trends due to each design factor, the following questions have not been answered: 1) what is the injection scheme effect on the detonation structure?, 2) what is the detonation structure in space (radial, axial, and the azumithal direction)?, 3) how do the injection dynamics vary depending on the injection scheme ?, 4) how does the mass flow rate affect the dynamics of the system?, 5) how is the detonation structure affected by varying the fuels? As such, it is imperative to examine the detailed dynamics in the real configuration that includes all these complexities. Thus far, much of design is driven by costly and time-consuming experiments supplemented by highly simplified one-dimensional theory. In conjunction with experimental work, reliable high-fidelity computational tools need to be developed for simulating the complex physics inside these engines to accelerate design process. The goal of this dissertation is 1) to develop a reliable and highly scalable compressible-reactive solver that enables simulation of full system RDEs, 2) examine the detailed detonation structure and injection dynamics, 3) provide the high-fidelity data to the community in conjunction with experimental groups.

1.4 Summary

This section introduced the RDE system and how it emerges as alternative gas turbine system. RDEs have the potential to overcome the limitation of the traditional thermal cycle and the other type of detonation engines such as PDEs. However, many physics remain unknown due to the limited measurement in the harsh environment in the facility and the expensive full system calculation. A reliable compressible-reactive solver needs to be developed to investigate the detailed physics that are associated with the non-premixed injector scheme. Furthermore, the high-fidelity simulation data that is validated with experimental data is imperative in the RDEs community to accelerate the design process.

1.5 Scope of the Dissertation

The goal of this dissertation is to provide the RDE community with a comprehensive database of full-scale RDE calculations for a variety of injector designs and operating conditions which enables the understanding of inhomogeneous detonations. In order to rapidly accelerate such engineering design, comprehensive RDE physics including chemistry, effects of realistic geometry on detonation structures, and the complexity of the injection scheme need to be understood. With this in mind, this dissertation will focus on a) the development of a solver that enables such simulations; b) simulating the full system RDE with a minimal set of simplifying assumptions, c) providing high-fidelity data that is validated in conjunction with Prof. Mirko Gamba's experimental group at U of M.

The outline of the dissertation is as follows:

- Chapter II will introduce the numerical methods used for solver development that enables the RDE calculations. RDEs pose unique modeling challenges: 1) the presence of detonation fronts requires special numerical tools to reduce dispersive/dissipative errors, 2) turbulent mixing that is driven by fuel/air injection needs to be captured accurately in order to predict detonation front velocity, and 3) complex injector geometries need to be handled. In order to address these challenges, a scalable RDE solver is developed in this work.

- Chapter III applies the solver to idealized two-dimensional unwrapped RDE calculations. Here, the detailed mechanism is used to examine the effect of the addition of hydrogen to the hydrocarbon chemistry, and compare with a prior study that used a global parameter or IPM. This chapter will discuss the verification of the solver in a practical application, and provide insight into the effect of operational parameters on RDE performance.

- Chapter IV considers a radial air inlet experimental RDE. The simulation target is the configuration studied at Air Force Research Laboratory. Similar geometries are widely studied in the community as it is known that the injector scheme is able to obtain stable detonation waves in the chamber. First, a grid resolution study is conducted to determine an appropriate resolution for the full scale RDE calculations. Next, two different boundary conditions, a total pressure boundary condition and a constant mass flow rate boundary condition, for the inlet are tested. The two boundary conditions match different experimental values, the effect of which will be discussed. Furthermore, the influence of the mass flow rate on the detonation structure with this type of the injector geometry is examined.

- Chapter V studies the axial air inlet RDEs facility at the University of Michigan. The purpose of the simulation is to understand how the different injector types affect the mixing process and the detonation structure. Detailed analysis of detonation behavior, including the effect of mass flow rate on RDE performance are discussed.

- Chapter VI discusses simulation of hydrocarbon-based configurations. Here, ethylene/air systems are simulated, and the effect of hydrogen addition on detonation stability analyzed. The main purpose of this simulation is to understand the cause of a steep drop in wave velocity that is observed in the experiment.

- Chapter VII summarizes the findings, and provides conclusions from this thesis. Future work is also discussed.

CHAPTER II

Development of the Computational Tools for Rotating Detonation Engines

2.1 Numerical Challenges in Simulation of RDEs

RDEs utilize detonation-driven combustion, as opposed to deflagration based combustion in conventional engines and gas turbines, to provide a pressure gain within the combustor flowpath. The main design challenge is in minimizing losses to this pressure gain, through an optimal choice of fuel/air injectors and post-combustion flow. For this purpose, an unsteady and turbulence-resolving computational tool is required. RDEs pose unique modeling challenges: 1) the presence of detonation fronts requires special numerical tools to reduce dispersive errors, 2) the mixing that is driven by fuel/air injection needs to be captured accurately in order to predict detonation front velocity, and 3) complex injector geometries need to be handled. In order to address these challenges, a RDE solver based on an open source frameworks is developed as discussed in the following sections. A preliminary numerical analysis is used to determine the appropriate choice of discretization approaches. Canonical flow problems are used to demonstrate convergence and performance of the solvers.

2.2 Governing equations

The numerical simulations solve the full set of governing equations for compressible fluid flow:

$$\frac{\partial \rho}{\partial t} + \frac{\partial \rho u_i}{\partial x_i} = 0, \tag{2.1}$$

$$\frac{\partial \rho u_i}{\partial t} + \frac{\partial \rho u_i u_j}{\partial x_j} = -\frac{\partial p}{\partial x_i} + \frac{\partial \tau_{ij}}{\partial x_j}, \tag{2.2}$$

$$\frac{\partial \rho E}{\partial t} + \frac{\partial \rho u_j H}{\partial x_j} = \frac{\partial}{\partial x_j} \alpha \frac{\partial T}{\partial x_j} + \frac{\partial \tau_{ij} u_i}{\partial x_j}, \tag{2.3}$$

$$\frac{\partial \rho Y_i}{\partial t} + \frac{\partial \rho u_j Y_i}{\partial x_j} = \frac{\partial}{\partial x_j} \rho D \frac{\partial Y_i}{\partial x_j} + \dot{\omega} M_i, \tag{2.4}$$

where ρ is the mass density, u_i is the velocity component in the i-th direction and p is the pressure. The viscous stress tensor components τ_{ij} are obtained as

$$\tau_{ij} = -2/3 \mu \frac{\partial u_k}{\partial x_k} \delta_{ij} + \mu \left(\frac{\partial u_j}{\partial x_i} + \frac{\partial u_i}{\partial x_j}\right), \tag{2.5}$$

where $\mu(T)$ is the viscosity of the fluid, and D is the species diffusion coefficient. The total energy E is give by

$$E = \int_{T0}^{T} C_p dT - p/\rho + \sum_{k=1}^{N} \Delta h_{f,k}^{0} Y_k + \frac{1}{2} u_i u_i, \tag{2.6}$$

and the total enthalpy is defined as $H = E + p/\rho$. Since the detonation wave increases the temperature up to 4000 K, the specific heat at the constant pressure C_p depends on the temperature, which is computed as a polynomial function. For each species $i = 1, \ldots, N$, where N is the number of species, Y_i is the mass fraction, $\dot{\omega}_i$ is the molar production rate given by:

$$\dot{\omega}_i = \sum_{k=1}^{N} (\nu^{''}_{i,k} - \nu^{'}_{i,k}) \Big[k_{f,k} \prod_{i=1}^{N} [A]_i^{\nu^{'}_{i,k}} - k_{b,k} \prod_{i=1}^{N} [A]_i^{\nu^{''}_{i,k}} \Big], \tag{2.7}$$

where M_i is the molecular mass, ν is the stoichiometric coefficient of each elementary reaction, k_f and k_b are the reaction rate coefficients of forward and backward elementary reactions, and $[A]$ is the mole fraction of each species.

2.3 Numerical Approach

Many of the prior detonation wave studies consider premixed inflows or Euler-equation based calculations [54–56], practical RDEs involves discrete fuel injectors that are recessed in order to shield them from the passing detonation wave. The stability and performance of the RDE is directly linked to the mixing process that occurs near the injectors. Hence, capturing this variable-density mixing in the presence of a strong detonation wave is critical. For this purpose, the Navier-Stokes equations with the diffusion terms needs to be solved.

Although the combustor pathway is annular and relatively simple, the injectors as well as the flowpath downstream of the combustor can involve complex geometries. In general, the simulation of shock-containing flow in complex geometries is non-trivial, although significant advances have been made in the last two decades [48, 57, 58]. However, the state of numerical algorithms for detonations in complex geometries has not progressed to the same extent as tools for other reacting or passive flows.

With this background, the present work analyzes the use and effectiveness of different numerical approaches for simulating full-scale RDEs. First, application to a sequence of test cases that are of relevance to RDE applications is presented. Finally, a summary of conclusions is provided.

2.4 OpenFOAM for Finite Volume Method (FVM)

The finite volume (FV) solver in this study is developed using the OpenFOAM framework [59], which provides open source tools for solving partial differential equations on complex domains. For this study, the second-order MUSCL-based HLLC scheme [60] for the convective fluxes and a four-stage Runge-Kutta method are implemented in OpenFOAM-4.1 version.

2.4.1 Implementation of HLLC scheme

The flux terms are discretized using a second-order MUSCL-based HLLC scheme [29]. This allows sharp gradients to be captured without introducing excessive numerical dissipation.

In this section, Euler Equation is considered to discuss the discretization of the non-linear convection term. Euler Equation with HLLC scheme is written as

$$U_t + F_x = 0 \tag{2.8}$$

where

$$U = \begin{bmatrix} \rho \\ \rho u_i \\ E \\ \rho Y_i \end{bmatrix}, F = \begin{bmatrix} \rho q \\ \rho u_i q + p n_x \\ (E+p)q \\ \rho Y_i q \end{bmatrix}, F_{HLLC} = \begin{cases} F_L & (if\ S_L > 0) \\ F_L^* & (if\ S_L < 0 < S_M) \\ F_R^* & (if\ S_M < 0 < S_R) \\ F_R & (if\ S_R < 0) \end{cases} \tag{2.9}$$

F_L^* and F_R^* are

$$\begin{aligned} F_L^* &= F_L + S_L(U_L^* - U_L) \\ F_R^* &= F_R + S_R(U_R^* - U_R) \end{aligned} \tag{2.10}$$

where q is defined as $q = u_i n_i$ where n_i gives the orientation of the interface separating the two states which define this Riemann problem. U_L and U_R are the states to the left (L) and right (R) of the discontinuity, respectively. S_L and S_R are the smallest and largest velocities of acoustic waves, and S_M is the velocity of the middle wave that separates the two intermediate state U_L^* and U_R^* as shown in Fig. 2.1. F_L and F_R are the fluxes F with the state to the left and right of the discontinuity.

The most well known approach for estimating bounds for the minimum and maximum signal velocities present in the solution of the Riemann problem is to provide, directly, wave speeds S_L and S_R [8, 58]. The most robust choice of wave speed is as follows

$$\begin{aligned} S_L &= min[q_L - c_L, \tilde{q} - \tilde{c}] \\ S_R &= max[q_R + c_R, \tilde{q} + \tilde{c}] \end{aligned} \tag{2.11}$$

where

$$\begin{aligned} &\tilde{q} = \tilde{u_i} n_i \\ &\tilde{u_i} = (u_{Li} + u_{Ri} R_\rho)/(1 + R_\rho) \\ &\tilde{c}^2 = (\gamma - 1)\Big[\tilde{H} - \frac{1}{2}(\tilde{u_i}^2)\Big] \\ &\tilde{H} = (H_L + H_R R_\rho)/(1 + R_\rho) \\ &R_\rho = \sqrt{\rho_R/\rho_L} \end{aligned} \tag{2.12}$$

and c is the speed of sound and R is the gas constant. Once wave speeds are computed, the wave speed S_M in the region between S_L and S_R can be found as follows

$$S_M = \frac{\rho_R q_R (S_R - q_R) - \rho_L q_L (S_L - q_L) + p_L - p_R}{\rho_R (S_R - q_R) - \rho_L (S_L - q_L)} \tag{2.13}$$

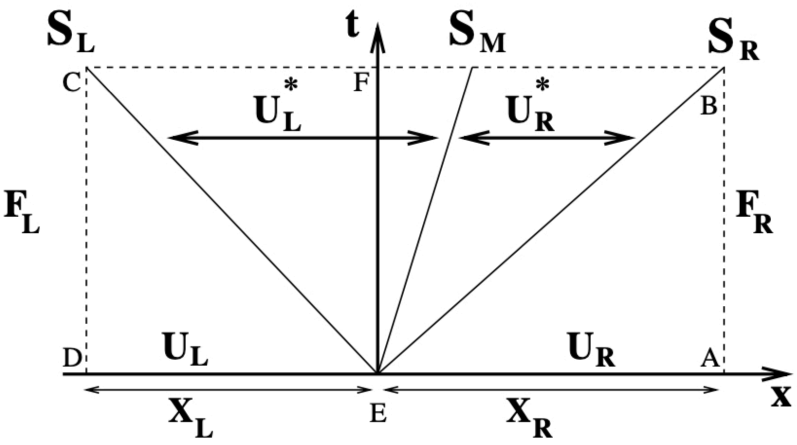

Figure 2.1: Simplified Riemann fan with two intermediate states. Reproduced by [8].

The states in the star region, for example, U_L^*, can be computed as

$$
\begin{aligned}
\rho_L^* &= \rho_L \frac{S_L - q_L}{S_L - S_M} \\
p_L^* &= \rho_L (q_L - S_L)(q_L - S_M) + p_L \\
(\rho u_i)_L^* &= \frac{(S_L - q_L)\rho_L u_{Li} + (p^* - p_L) n_x}{S_L - S_M} \\
E_L^* &= \frac{(S_L - q_L) E_L - p_L q_L + p^* S_M}{S_L - S_M} \\
(\rho Y_i)_L^* &= \rho_L Y_{Li} \frac{S_L - q_L}{S_L - S_M}
\end{aligned}
\tag{2.14}
$$

Note that $p^* = p_L^* = p_R^*$. In the case where $S_M < 0$, the equations for F_R^* follow by simply changing the L subscripts to R, respectively.

2.4.2 Implementation of diffusion terms

To solve the Navier-Stokes equations, a discretization of the diffusion terms is needed. The Kurganov, Noelle and Petrova (KNP) method is used as the diffusion discretization in UMdetFoam [61]. The implementation of rhoCentralFoam, which is one of the defaut compresible solver utilizing the KNP method in OpenFOAM framework, is referred to for the implementation. The basic idea of the KNP method is 1) to compute the local propagation speed at faces, 2) to compute the weighting factor based on those local propagation speed, 3) to interpolate the fluxes with these weighting factors.

2.4.2.1 Implementation of the viscous term

From Eqn. 2.2, the viscous term is

$$\begin{aligned} \frac{\partial \tau_{ij}}{\partial x_j} &= \nabla \cdot \left[\mu\left[\nabla \mathbf{u} + (\nabla \mathbf{u})^T\right] - \frac{2}{3}\mu tr(\mathbf{D})\mathbf{I}\right] \\ &= \underbrace{\nabla \cdot \Big[\mu\big[\nabla \mathbf{u}\big]}_{Laplacian} + \nabla \cdot \underbrace{\mu\Big[(\nabla \mathbf{u})^T\Big] - \frac{2}{3}tr(\mathbf{D})\mathbf{I}\Big]}_{\xi} \end{aligned} \tag{2.15}$$

where $\mathbf{D} = \frac{1}{2}\left[\nabla \mathbf{u} + (\nabla \mathbf{u})^T\right]$ and $\mathbf{u}$ is the velocity.

The Laplacian term is computed by a native function within OpenFoam. ξ term is also computed by a native function in OpenFoam that is called *dev*2. The implementation is shown in Fig. 2.2.

2.4.2.2 Implementation of the diffusion terms for the energy equation

From Eqn. 2.3, the diffusion terms for the energy equation can be rewritten as

$$\begin{aligned} &\frac{\partial}{\partial x_j}\alpha\frac{\partial T}{\partial x_j} + \frac{\partial \tau_{ij} u_i}{\partial x_j} \\ &= \underbrace{\nabla \cdot \mathbf{T} \cdot \mathbf{u}}_{\Phi} - \underbrace{\nabla \cdot [\alpha \nabla \cdot T]}_{Laplacian} \end{aligned} \tag{2.16}$$

where

$$\mathbf{T} = \mu\left[\nabla \mathbf{u} + (\nabla \mathbf{u})^T\right] - \frac{2}{3}\mu tr(\mathbf{D})\mathbf{I} \tag{2.17}$$

The laplacian term is computed with the native function in OpenFOAM. Φ can be computed by applying the KNP method to the integral form of the term as follows,

$$
\begin{aligned}
&\int\limits_V \nabla \cdot \big(\mathbf{T} \cdot \mathbf{u}\big) dV \\
&= \int\limits_S d\mathbf{S} \cdot \big(\mathbf{T} \cdot \mathbf{u}\big) \approx \sum_f \mathbf{S}_f \cdot \big(\mathbf{T} \cdot \mathbf{u}\big) \\
&= \sum_f \mathbf{S}_f \cdot \Big(\Big[\mu\big[\nabla\mathbf{u} + (\nabla\mathbf{u})^{\mathbf{T}}\big] - \mathbf{\frac{2}{3}}\mu\mathbf{tr}(\mathbf{D})\mathbf{I}\Big] \cdot \mathbf{u}\Big) \\
&= \sum_f \Big[\big[\mathbf{S}_f \cdot \big(\mu\nabla\mathbf{u}\big)\big] + \big[\mathbf{S}_f \cdot \underbrace{\big(\mu\nabla(\mathbf{u})^T - \frac{2}{3}\mu tr(\mathbf{D})\mathbf{I}\big)}_{\xi}\big]\Big] \cdot (\beta\mathbf{u}_{f+} + (1-\beta)\mathbf{u}_{f-})
\end{aligned}
\tag{2.18}
$$

where $\mathbf{S}_f$ is the surface vector of the face area. The interpolation procedure is split into two directions corresponding to flow outward and inward of the face owner cell, which is denoted as $f+$ and f, respectively. With the KNP method [61], β can be computed as

$$\beta = \frac{a_p}{a_p - a_m} \tag{2.19}$$

where

$$
\begin{aligned}
a_p &= max(\phi_{f+} + c_{f+}S_f, \phi_{f-} + c_{f-}S_f, 0) \\
a_m &= min(\phi_{f+} - c_{f+}S_f, \phi_{f-} - c_{f-}S_f, 0)
\end{aligned}
\tag{2.20}
$$

Here, $c_{f\pm} = \sqrt{\gamma R T_{\pm}}$ are the speeds of sound of the gas at the face, outward and inward of the owner cell, S_f is the face area, and $\phi_{f\pm} = \mathbf{S}_{f\pm} \cdot \mathbf{u}_{f\pm}$. $\mathbf{S}_f$ and $\mu\nabla\mathbf{u}$ can be computed by native functions in OpenFOAM, $magSf()$ and $snGrad()$ respectively. ξ term can be computed in the save way as the viscous term in Sec 2.4.2.1. $u_{f\pm}$ are

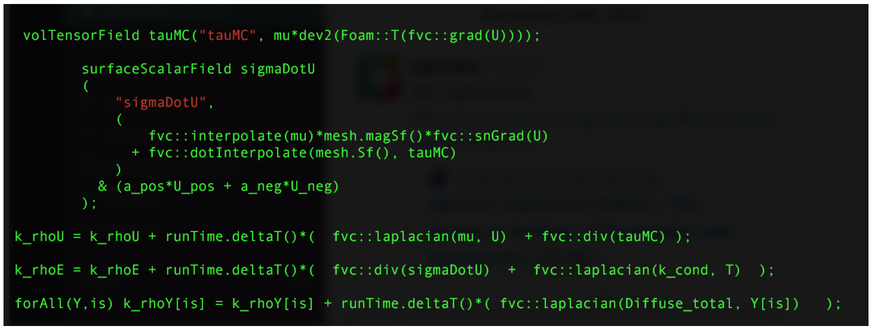

```
 volTensorField tauMC("tauMC", mu*dev2(Foam::T(fvc::grad(U))));

        surfaceScalarField sigmaDotU
        (
            "sigmaDotU",
            (
                fvc::interpolate(mu)*mesh.magSf()*fvc::snGrad(U)
              + fvc::dotInterpolate(mesh.Sf(), tauMC)
            )
          & (a_pos*U_pos + a_neg*U_neg)
        );

k_rhoU = k_rhoU + runTime.deltaT()*(  fvc::laplacian(mu, U)  + fvc::div(tauMC) );

k_rhoE = k_rhoE + runTime.deltaT()*(  fvc::div(sigmaDotU)  +  fvc::laplacian(k_cond, T)  );

forAll(Y,is) k_rhoY[is] = k_rhoY[is] + runTime.deltaT()*( fvc::laplacian(Diffuse_total, Y[is])   );
```

Figure 2.2: Implementation of diffusion terms in the solver.

the velocity interpolated to faces from cell values. The detailed implementation is shown in Fig. 2.2.

2.4.2.3 Implementation of the diffusion terms for the transportation equations

From Eqn. 2.4, the diffusion term for the transportation equations is

$$\underbrace{\frac{\partial}{\partial x_j}\rho D\frac{\partial Y_i}{\partial x_j}}_{Laplacian} \tag{2.21}$$

The laplacian term is computed with a native function in OpenFOAM. The detailed implementation is shown in Fig. 2.2.

2.4.3 Coupling between FVM solver and Cantera

The Cantera package [62] is integrated to handle chemical source term evaluations. The Cantera package in the C++ version is used for this purpose. Cantera utilizes a chemical mechanism and thermophysical data to compute chemical source terms, thermophysical properties, and transport properties.

The brief coupling algorithm is shown in Fig. 2.3. First, Cantera reads in a user-specified chemistry file from the case directory, that contains the chemical mechanism and thermophysical data. The FVM solver automatically sets the necessary number

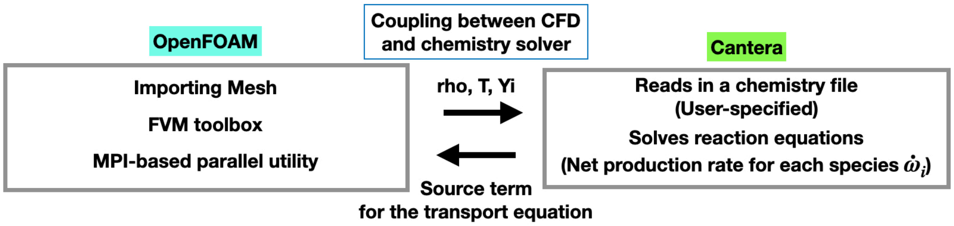

Figure 2.3: Brief algorithm between OpenFOAM and Cantera.

of species transport equations based on the number of species in the mechanism. Each iteration the solution is split into two parts. The first part consists of computing the inviscid and viscous flux without chemical reactions and updating the flow field. For each cell, the species concentration and thermodynamic state are passed to Cantera. The second part consists of Cantera using this information to compute the chemical source terms. The chemical time scales are faster than that of the flow field requiring a sub-iteration to integrate the faster chemical scales over the flow field time scale. In each sub-step, the time step is chosen such that each sub-iteration does not change the species fraction more than 5% from the old state. Finally, the FVM solver updates the thermal properties (using Cantera) as well as the species compositions at the end of the iterations.

2.5 Verification with Canonical Problems

2.5.1 1D detonation tube

The first test case involves a one-dimensional detonation problem conducted in a semi-closed tube, schematically shown in Fig. 2.4. The tube is filled with a premixed hydrogen and air mixture at 1 atm pressure and 300 K initial temperature. A small section at the left end of the tube is filled with a high pressure (27.1 atm), high temperature (3000 K) post-detonation mixture. The detonation wave then propagates towards the right over a distance of 0.3 m. After an initial transient phase, the detonation wave develops into a one-dimensional structure, which should be similar

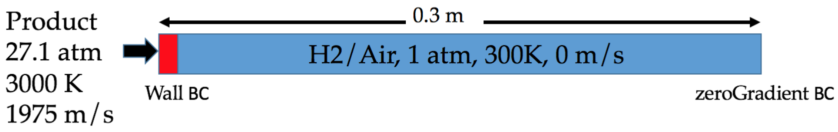

Figure 2.4: 1D detonation tube configuration.

to the ZND theoretical structure. In the past, other techniques such as the conversion of the governing equations to a set of ordinary differential equations in time have been used to solve this problem [63]. Here, the partial differential equations are directly solved on a set of computational grids.

Figures 2.5 and 2.6 show the pressure and temperature fields after the wave is fully developed. As predicted by the ZND theory, there exists a sharp jump in pressure denoting a shock wave, with a high peak pressure. An equivalent spike in temperature is also observed. After the detonation, expansion of the gases leads to a drop in pressure and temperature from approximatively 0.1 m to 0.24 m, where ignition causes consumption of the fuel-air mixture. The species profiles (Fig. 2.7) show a similar structure, where the consumption of the fuel-oxidizer mixture starts around 0.01 cm from the shock location. It is interesting to note that the H and O concentrations remain high at large distances from the shock location, indicating a slow return to equilibrium. This is caused by the expansion of the post-detonation gases that are moving at velocities slower than the wave velocity [leading to a spatially-expanding region of post-detonation products].

To understand the numerical properties of the solver, spatial convergence studies were conducted. Two different quantities of interest were considered: a) the von Neumann pressure, which is the highest pressure obtained in the post-shock region, and b) a numerically extracted Chapman-Jouguet velocity. This latter quantity is obtained as follows. At each time step, the location of 10% pressure rise from the ambient (1 atm) condition is noted. The velocity, the slope of the location versus

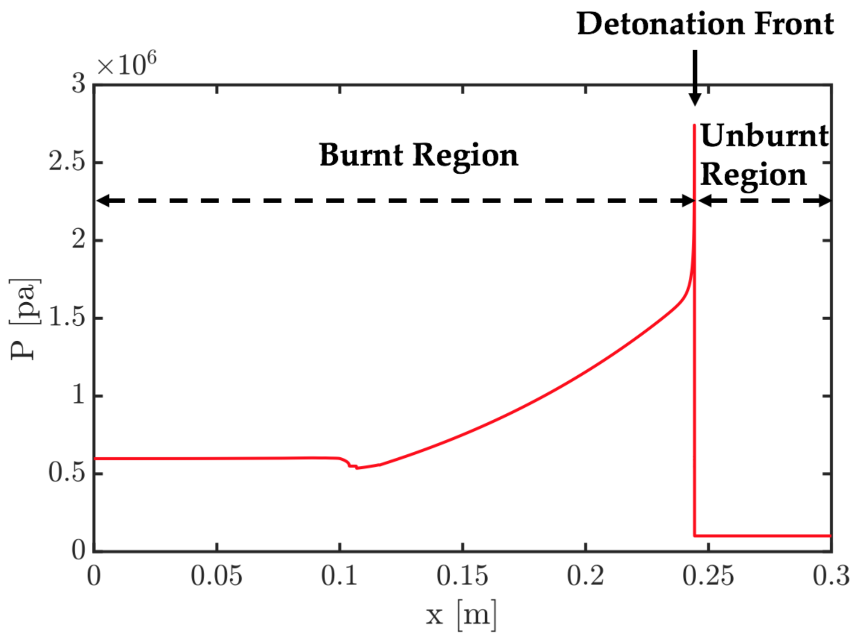

Figure 2.5: Pressure property at $P_\infty = 1$ atm, $T_\infty = 300$ K with detailed chemistry.

time curve, is obtained. It was noted that once a steady state is reached, this slope remained nearly a constant. Two different sets of simulations were conducted. One set used uniform mesh but with varying grid sizes, while the other uses AMR. A native implementation of AMR in OpenFOAM is used along with this discretization appropach. The AMR implementation uses local spatial gradients of a specified variable set to divide computational cells successively by factors of 2. The method also coarsens the grid by combining cells in regions with low spatial gradients. For the AMR cases, the initial grid is kept constant for all the simulations, but the number of levels of refinement was adjusted to obtain progressively finer grid sizes during the course of the simulation. The error is taken as the absolute difference in the quantity of interest between a specific case and the finest resolution case using that solver (AMR or uniform mesh solver). The finest mesh size for both the AMR and uniform grid solver is $\Delta x = 1.25 \times 10^{-5}$ m.

Figures 2.8 and 2.9 show the convergence of the two quantities of interest. The pressure convergence follows nearly a first-order rate, consistent with the upwinding

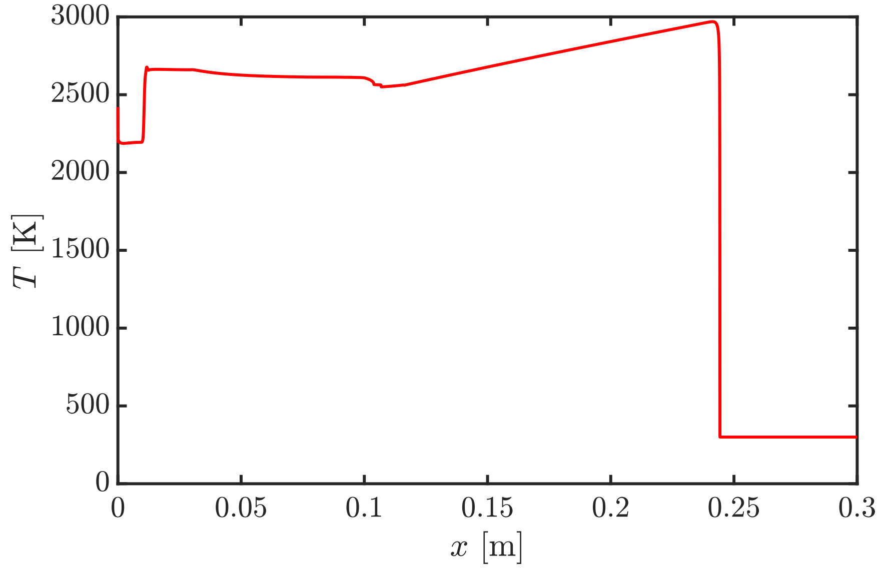

Figure 2.6: Temperature property at $P_\infty = 1$ atm, $T_\infty = 300$ K with detailed chemistry.

necessary to stabilize the solver. Interestingly, the AMR solver shows higher errors compared to the uniform grid solver. This trend is more visible in the CJ velocity convergence, where the AMR errors are significantly higher compared to the uniform grid. This can be primarily explained by the nature of the refinement used. The criteria is based on the density gradient, which is maximized near the location of the von Neumann spike. However, the post-shock reaction region is not adequately resolved. This leads to errors in the prediction of ignition, which results in increased overall error in the quantities of interest. Interestingly, even though the AMR refinement criterion is related to the initial density gradient, the lack of accuracy in predicting the reaction zone leads to errors in capturing the von Neumann pressure as well. This provides a cautionary example, where refinement without considering the inherent physics of the problem might lead to loss of accuracy. In the future, other refinement criteria will be tested in order to determine the optimal choice for detonation problems.

Although AMR is able to reduce the number of grid points for the required resolution, error convergence does not show significant improvement compared to the

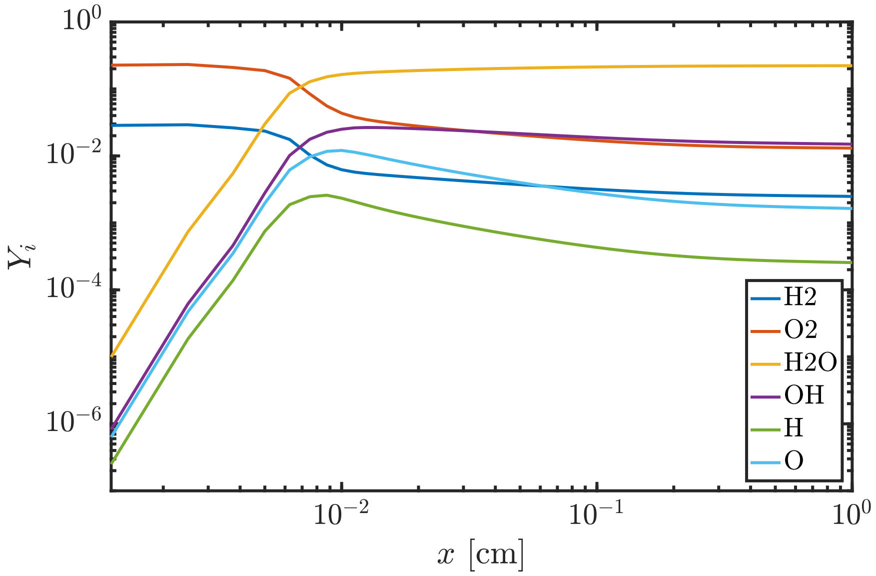

Figure 2.7: Species mass fraction VS. distance from the shock front.

uniform grids. Further, the criteria for refinement needs to be analyzed in order to optimize the computational cost of AMR and the achieved reduced error, which will be future work regarding this study. With this mind, uniform grids are utilized in the cases studied below.

2.5.2 2D detonation tube

Cellular structures formed by detonations confined to two-dimensional channels have been routinely used to understand detonation structures as well as the rates of chemical reaction. The detonation waves reflect from the channel wall and create local peak pressure points at the detonation front [43, 64, 65]. The trace of the maximum pressure on the wall forms a cellular structure, the size of which could be used to assess the strength of detonation. In particular, smaller cells are associated with highly detonable mixtures.

The simulation configuration is shown in Fig. 2.10. The stoichiometric mixture of hydrogen and air is at a pressure of 1 atm and temperature of 300 K. The domain extends 100 × 2 mm with $\Delta x = 50\mu m$. These simulation conditions have

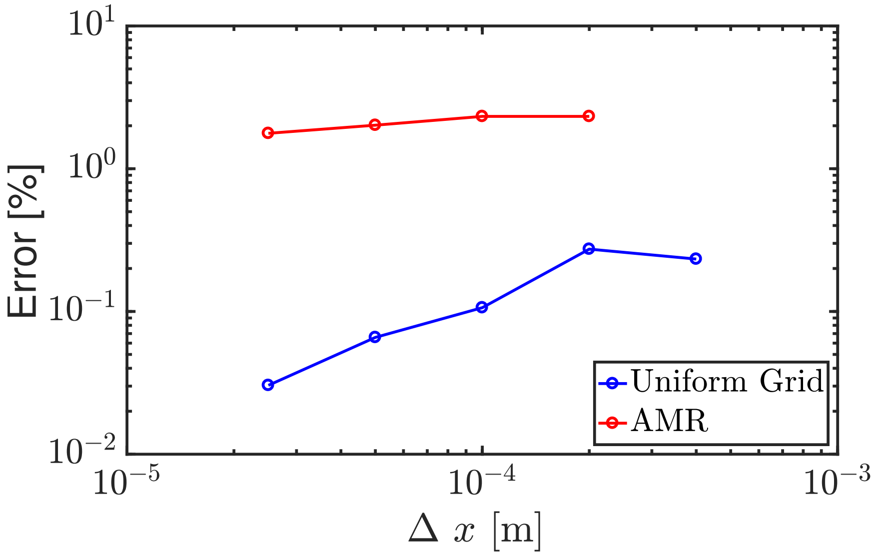

Figure 2.8: Error convergence for Chapman Jouguet velocity.

been used to represent prior studies [64]. In order to initiate the transverse wave structure, 3 discrete blocks of 0.15 × 0.5 mm are initialized at a higher temperature, and positioned equidistant from each other in the stream-normal direction at a short distance from the inflow. It is seen that the fully-developed detonation front is formed relatively quickly, and maintains the triple point structure throughout the axial distance. Figure 2.11 shows the evolution of the detonation front, including the high pressure points that are the result of the intersection of transverse waves and the detonation front. These triple points provide the ignition points for the reactive mixture. Figure 2.12 shows the trace of the peak pressure as the detonation front moves through the tube. As expected, the reflection of the triple points due to the bounding walls lead to a cellular structure with highly regular patterns. The size of these cellular structures using the Mueller mechanism is consistent with prior studies utilizing the Jachimowski mechanism [66], as shown in Figure 8 (b) in [64]. This indicates that the current solver is able to reproduce prior data, even with different chemistry mechanism.

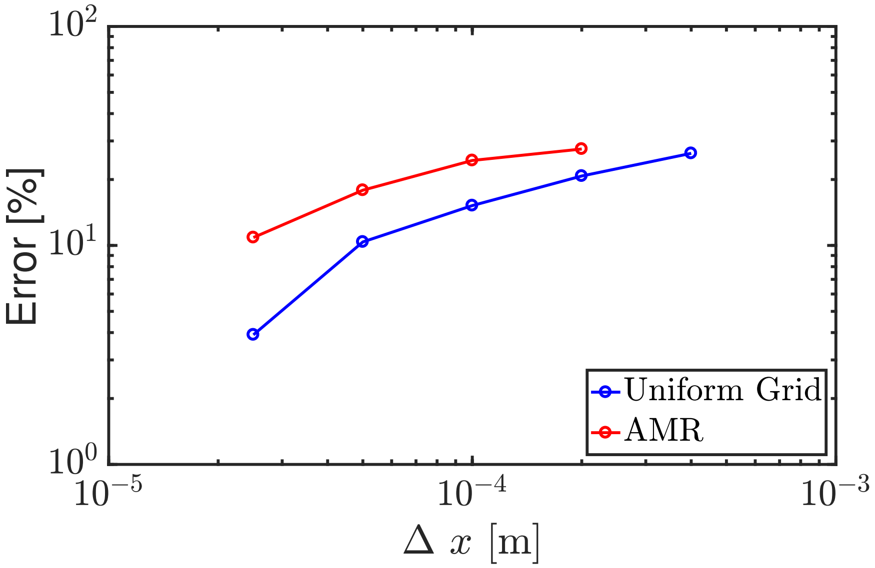

Figure 2.9: Error convergence for Von Neumann pressure.

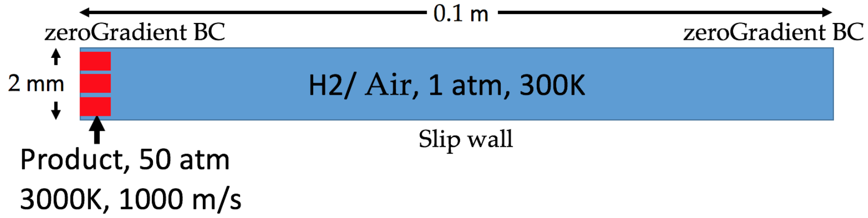

Figure 2.10: 2D detonation tube configuration.

2.6 Summary and Conclusion

This chapter summarizes the theoretical part of the solver UMdetFoam, its development and verification using canonical problems. MUSCL-based HLLC scheme and the two-stage Runge Kutta method are implemented for the flux and time integration, respectively. KNP method is implemented to discretize the diffusion terms. UMdetFoam successfully captures the peak values at the wave front that is supported by the chemical reaction. The convergence test reveals that the Von Neumann pressure and the wave speed are within 5% error with a grid spacing of 1×10^{-4}. As a further verification test, a two dimensional detonation tube case is conducted. The cellular structure, which is representative of the detailed dynamics in the induction region, is successfully captured by the developed solver. The cell size, which is used

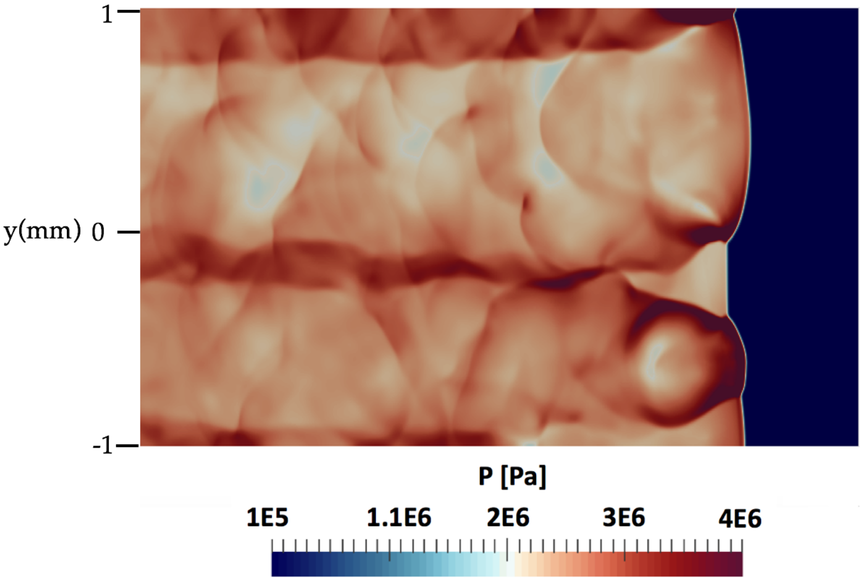

Figure 2.11: Triple points at the detonation front.

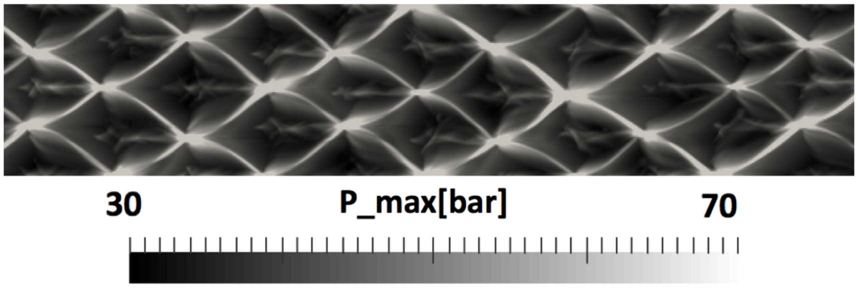

Figure 2.12: Cellular structure visualized by time history of the local maximum pressure.

to validate the reaction rate at the wave front, matches the prior study.

CHAPTER III

Simulation of Simplified RDE Configurations

3.1 Unwrapped RDE Simulation

Much of the prior RDE research has been devoted to the use of hydrogen as a fuel. More recently, however, there has been interest in the use of RDEs for stationary power generation and for rocket combustion, both of which require hydrocarbon fuels. The purpose of this chapter is to elucidate the reaction structure in canonical flows for methane and ethylene-based detonation engines. Detailed numerical simulations of an unwrapped RDE are conducted using these fuels with varying levels of hydrogen dilution. Variations in operational parameters such as inflow gas temperatures and exit pressures are also considered. Comparisons with theoretical models indicate that such analytical descriptions sufficiently capture the performance for a wide range of conditions. Detailed analysis of the reaction structure shows that there exists a critical pressure that sustains the detonation front.

3.2 Simulation Configuration

3.2.1 Flow feature

The chemistry mechanisms for these cases are as follows: a) for ethylene, the mechanism of Varatharajan et al. [67] based on 21 species and 38 reactions is used;

b) for methane, the Petersen mechanism with 22 species and 34 reactions is used [68]. Both these mechanisms allow the use of hydrogen as a species, which will be leveraged to study different levels of hydrogen addition to the fuel-air mixture.

The flow configuration considered is shown schematically in Fig. 3.1. The rectangular flow domain consists of periodic boundaries on the left and right side and outflow at the top. At the bottom, the premixed fuel-air mixture is injected based on prescribed stagnation conditions. A detonation wave is initiated by patching a one-dimensional solution in a small region of the domain. The flow then stabilizes over some initial time. All results presented here were extracted once a statistically stationary state was reached, where the detonation wave traveled at nearly constant speed across the domain. Fig. 3.1 also shows different flow features in the domain. In particular, the detonation wave separates the reactant zone from the product zone. As the product gases travel axially in the domain, they come in contact with fresh gases, leading to a region of possible deflagration. The flow then expands, gaining axial speed, and reaches the outflow. Note that the nature of the outflow depends on the imposed back pressure. When the back pressure is relatively low (compared to post-detonation pressure), the flow will expand and can become supersonic. In this case, the numerically applied back pressure has no role in the simulations. On the other hand, if the back pressure is sufficiently large, the flow will remain subsonic within the domain. The back pressure is an important quantity since it directly controls the pre-detonation pressure within the chamber. As a result, this variation in back pressure will be used to control the detonation processes in this work.

3.2.2 Dimensions and boundary conditions

The dimensions of the flow domain are based on prior studies [3, 7] and are provided in Table 3.1. While the geometry of Schwer and Kailasanath [7] is used to demonstrate validity of the current approach, the geometry of Rankin et al. [3] is

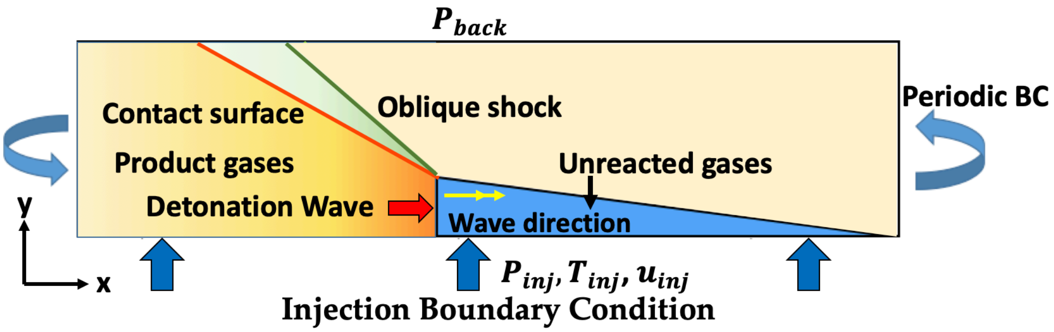

Figure 3.1: Schematic of flow structure in the unwrapped 2D RDE configuration.

used to provide baseline data for future comparisons with experimental data. The grid spacing of 2×10^{-4} m is deemed sufficient for the calculations performed here. It was observed that a reduction of this grid spacing by a factor of 2-4 did not change the results.

Configuration	Geometry size [m]	Reference	Grid size	Grid spacing
1	$0.4788 \times 0.14 \times 0.01$	Schwer et al. [7]	1776348	2×10^{-4} m
2	$0.4596 \times 0.1016 \times 0.0076$	Rankin et al. [3]	1263900	2×10^{-4} m

Table 3.1: Dimensions of the RDE configurations.

The prescription of the injection flux based on the chosen stagnation conditions requires additional details. The method used here is identical to that of Schwer and Kailasanath [69]; it is repeated for the sake of completeness. For this discussion, P^0_{inj} indicates the stagnation pressure based on the injection conditions, and P_{wall} is the pressure at the first control volume in the domain above the lower injection boundary. Further, P_{cr} denotes the critical pressure for choked flow based on the injection stagnation pressure and is obtained as

$$P_{cr} = P^0_{inj}\left(\frac{2}{\gamma+1}\right)^{\frac{\gamma}{\gamma-1}}, \tag{3.1}$$

where γ is the specific-heat capacity ratio of the fuel-air mixture at the injection temperature prescribed.

As the detonation wave progresses in the domain, the pressure at the wall will change, with peak pressure associated with the detonation wave located in the control volume. The injection flux then depends both on the inflow conditions and the conditions within the domain. Further, this flux depends on the location on the boundary and needs to be computed locally for each boundary control volume. For this reason, the injection flux is computed as follows: 1) if $P_{wall} \geqslant P^0_{inj}$, the boundary cell face is treated as a wall, 2) if $P^0_{inj} > P_{wall} > P_{cr}$, then the flow is not choked and $P_{inj} = P_{wall}$, and 3) if $P_{wall} < P_{cr}$, then the flow is choked and $P_{inj} = P_{cr}$.

Based on these conditions, the inflow quantities can be computed as

$$T_{inj} = T^0_{inj}\Big(\frac{P_{inj}}{P^0_{inj}}\Big)^{\frac{\gamma-1}{\gamma}}, \qquad u_{inj} = \sqrt{\frac{2\gamma}{\gamma-1}RT^0_{inj}\Big[1-\Big(\frac{P_{inj}}{P^0_{inj}}\Big)^{\frac{\gamma-1}{\gamma}}\Big]} \tag{3.2}$$

The flux computed based on the relations above is multiplied by an area ratio that denotes the ratio of cross-sectional area between the nozzles and the detonation chamber. This ratio is set to 0.2 for the present study. The outflow is treated either using supersonic or subsonic conditions based on the configuration. In this section, the outflow back pressure is set to 1 atm. The grid is axially stretched near the exit plane in order to remove pressure fluctuations.

3.2.3 Assessment of the system performance

To obtain performance related metrics for the RDE, the mass flow rate is computed as

$$\dot{m} = \int\limits_{inlet} \rho u_{inj} dx, \tag{3.3}$$

where ρ and u_{inj} are obtained from the boundary conditions discussed in Sec. 3.2.2. The net force is obtained as

$$F = \int\limits_{exit} \rho u^2 + (p - p_{back}) dx, \tag{3.4}$$

where p_{back} is the imposed back pressure and u indicates the face-normal velocity. Based on these quantities, the specific impulse is computed as

$$I_{sp} = \frac{F}{\dot{m}_{fuel} g}, \tag{3.5}$$

where g is the gravitational acceleration and $\dot{m}_{fuel}$ is the mass of fuel in a total flow rate of $\dot{m}$.

The simulation results are also compared against analytical results as a sanity check. The analytical model used in this study is the axial flow model proposed by Shepherd et al. [10]. The basic assumption made in this model is that the flow becomes predominantly axial far away from the detonation layer. This assumption is valid if the injection does not have a net azimuthal rotation and a sufficiently long chamber makes azimuthal flow negligible at the exit [10]. It is shown that the following analytical relation for specific impulse can be derived by applying traditional rocket motor quasi-one-dimensional theory:

$$\begin{aligned} \frac{F}{\dot{m}}\bigg|_{P_{back}} &= a_1 f(M_{CJ}, \gamma, P_{back}/P_1) \\ &= a_1 \sqrt{\frac{2}{\gamma - 1}} \Bigg[1 + \frac{1}{2(\gamma+1)} \Big(M_{CJ} - \frac{1}{M_{CJ}} \Big)^2 - \\ &\quad \Big(\frac{P_{back}}{P_1} \Big)^{(\gamma-1)/\gamma} \frac{1}{M_{CJ}^2} \Big(\frac{\gamma+1}{\gamma M_{CJ}^2 + 1} \Big)^{-(\gamma+1)/\gamma} \Bigg]^{1/2}. \end{aligned} \tag{3.6}$$

In the above equation, $\dot{m}$ is the mixture mass flow rate to the domain, a_1 is the speed of sound in the pre-detonation gases, M_{CJ} is the Mach number at CJ state, γ is the specific heat ratio, P_{back} is the back pressure at the exit and P_1 is the pressure of the pre-detonation gases. The CJ state is computed in Cantera with inputs of pre-detonation conditions obtained in the simulation. Additional details about the model can be found in [10].

3.3 Verification

In order to verify the UMdetFOAM solver, it is first compared against the geometry of Schwer and Kailasanath [7], corresponding to configuration 1 in Table 3.1. Both hydrogen/air and ethylene/air at stoichiometric conditions with a temperature of 300 K and pressure of 1 atm were simulated.

Figure 3.2 shows the general flow field structure that exhibits the characteristic zones shown in the schematic above (Fig. 3.1). The notations used by Kailasanath and Schwer [7] mark different regions of the flow. Region A denotes the detonation front, which has a characteristic curved structure. This detonation front gives rise to the oblique shock wave, B. The contact surface, C, exhibits strong shear-layer like features including vertical structures. The region G represents the unreacted gases that fill up, and the slope of the upper boundary between regions G and E is determined by the inflow flux and the speed of propagation of the detonation wave. In region F, injection is blocked due to the high post-detonation pressure based on the boundary conditions discussed in Sec. 3.2.2. Region E represents the burnt products which are convected from the detonation front in between the secondary shock wave D and the blocked injectors.

Table 3.2 shows the comparison of the results from the present study with both the simulations of Schwer and Kailasanath [7] and the theoretical model discussed above. Overall, the simulations in the current study compare well with the prior work, but produce higher force and specific impulse for all cases considered. The variations from the prior work observed here are consistent with the differences found by Schwer et

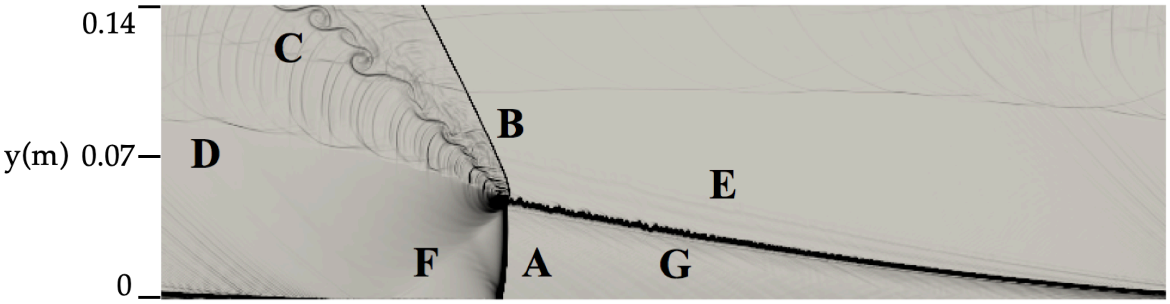

Figure 3.2: Reference flow structure for hydrogen/air detonation in the 2D unwrapped geometry.

al. [70] when using a new solver. Given that the mass flow rates are roughly equal, this implies that the outflow velocity and/or pressure are higher in the UMdetFOAM solver. This may be the result of differences in either numerical methods or in total heat release. The prior work uses an induction time based model which does not account for deflagration processes, especially at the boundaries separating regions G and E. Note that the simulations were conducted by setting viscosity and scalar diffusivities to zero to be consistent with prior work [7]. Despite this, the inclusion of these terms did not change the results significantly, as noted in the table. All simulations reported hereinafter use the viscous formulation.

Fuel	Model	Wave velocity[m/s]	Mass flow [kg/s]	F [N]	I_{sp} [1/s]
H_2	Detailed kinetics/Euler	1927	1.611	2319	5186
H_2	IPM[7]	1854	1.613	2199	4911
H_2	Analytical	1984	–	–	5463
C_2H_4	Detailed kinetics/Euler	1789	1.866	2512	2158
C_2H_4	IPM[7]	1716	1.877	2364	2022
C_2H_4	Analytical	1838	–	–	2357
C_2H_4	Detailed kinetics/Navier Stokes	1781	1.867	2511	2155

Table 3.2: Comparison of RDE characteristic quantities between present study, prior RDE simulations of Schwer and Kailasanath [7] and analytical model [10].

3.4 General Detonation Structure

The cases studied in this section are based on the geometry of Rankin et al. [3] (configuration 2 in Tab. 3.1). The full viscous/diffusive terms are included in the simulations. The cases considered include ethylene and methane with varying degrees of dilution and operating conditions. A list of mixtures and operating conditions are provided in Table 3.3. Since pure methane does not detonate at ambient inflow conditions, higher injection and back pressure, as well as increased inflow temperature, were utilized.

3.4.1 Performance of the system and detonability

For both ethylene and methane chemistry, the wave speed and the specific impulse increases with hydrogen addition. Since hydrogen is more detonable and exhibits a higher CJ speed, this trend indicates that the heat release process is increasingly dominated by the presence of hydrogen. For the 50/50 blend of methane/hydrogen, it is seen that as the back pressure increases, the thrust decreases, which is consistent with the definition of thrust in Eq. 6.3. Further, specific impulse also decreases as the ratio of the injection stagnation pressure to back pressure increases. As will be seen in the detailed images of the flow field, this reduction comes mainly through a reduction in the acceleration of the flow processed by the detonation wave. When the back pressure is low, the flow becomes supersonic whereas with increased back pressure, the flow remains subsonic. This reduction in velocity is achieved through tertiary shock waves that reduce the total pressure of the fluid.

The comparisons with theoretical specific impulse predictions show interesting trends (3.3). For large P^0_{inj}/P_{back}, the detailed calculations and the theoretical predictions are reasonably close, indicating that when the flow is expanded to supersonic conditions, the assumptions underpinning the theoretical model are valid. However, when the back pressure is increased, the differences become large since the flow at the exit plane is subsonic and might contain a significant azimuthal component to the flow.

Mixture	$P^0_{inj} : P_{back} : T^0_{inj}$ [atm]:[atm];[K]	Wave velocity [m/s]	Th.Wave velocity [m/s]	Mass flow [kg/s]	F [N]	I_{sp} [1/s]	Th.I_{sp} [1/s]
C_2H_4	10:1:300	1786	1837	1.362	1832	2156	2318
C_2H_4/H_2(75/25)	10:1:300	1798	1845	1.353	1825	2225	2513
C_2H_4/H_2(50/50)	10:1:300	1818	1858	1.329	1808	2359	2645
C_2H_4/H_2(25/75)	10:1:300	1853	1885	1.287	1777	2698	2979
CH_4/H_2(75/25)	30:6:300	N/A	N/A	N/A	N/A	N/A	N/A
CH_4/H_2(50/50)	30:6:300	1760	1864	3.881	4494	2370	2520
CH_4/H_2(75/25)	30:10:793	N/A	N/A	N/A	N/A	N/A	N/A
CH_4/H_2(50/50)	30:10:793	1697	1846	2.642	1909	1479	1760
CH_4	30:14:793	1685	1817	2.618	1537	1086	1482
CH_4/H_2(75/25)	30:14:793	1699	1830	2.601	1517	1122	1577
CH_4/H_2(50/50)	30:14:793	1723	1850	2.572	1496	1191	1675
CH_4/H_2(25/75)	30:14:793	1754	1887	2.515	1447	1342	1918

Table 3.3: Comparison of performance characteristics of the RDE for different flow conditions with analytical model.

3.4.2 Flow structure with hydrogen addition

The details of the flow field are provided in Figs. 3.3-3.6, where temperature and pressure fields from the ethylene/hydrogen and methane/hydrogen simulations are provided. The temperature plots show that the overall structure of the detonation wave does not change between the different simulations. However, for both ethylene and methane, the pure fuel simulations produce lower temperatures in the region between the contact surface and the oblique shock wave. As the hydrogen content is increased, the temperature in this region increases. For the methane case, tertiary shock structures appear, leading to striations in the temperature field. The pressure field shows similar behavior, with the pure fuel cases providing higher pressure jumps across the detonation front. Moreover, the detonation height, defined as the distance from the bottom of the domain to the highest axial point at which peak detonation pressure is observed, is found to decrease with increase in hydrogen concentration. As the hydrogen content is increased, the detonation wave speed increases, but the injection flux is still controlled by the higher density hydrocarbon content. As a result, the refill height decreases leading to shorter detonation height.

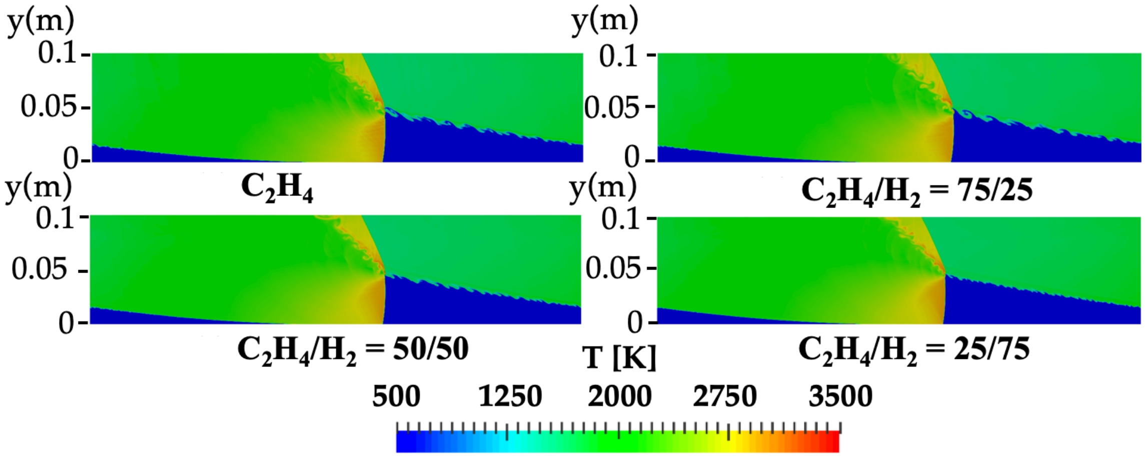

Figure 3.3: Temperature fields for different C_2H_4/H_2 mixtures detonating in air at stoichiometric conditions.

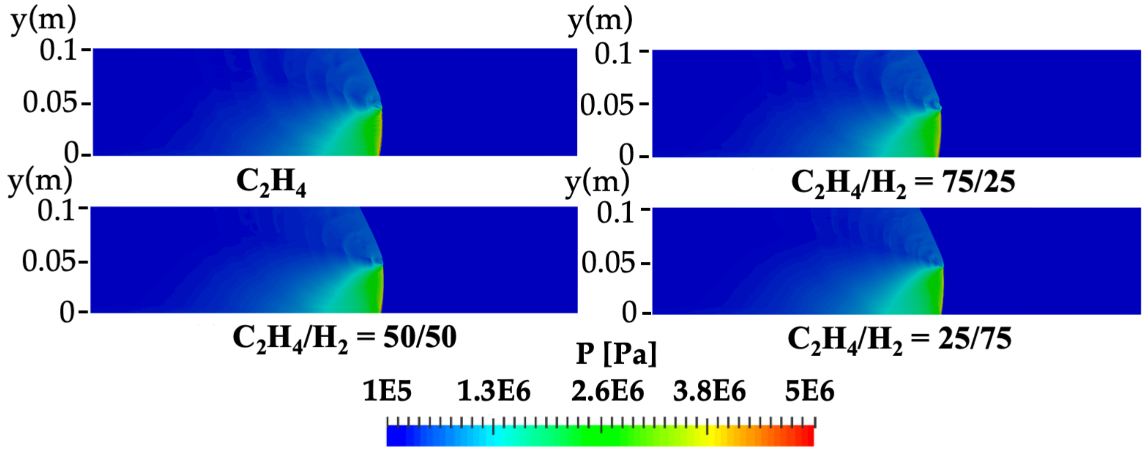

Figure 3.4: Pressure fields for different C_2H_4/H_2 mixtures detonating in air at stoichiometric conditions.

An important feature of the flow is the acceleration of subsonic or sonic incoming flow to supersonic speeds, subject to the effect of backpressure. Figures 3.7 and 3.8 show the Mach number field for the two sets of cases. The ethylene cases show remarkably similar Mach number fields, implying that the flow behavior is not substantially altered by the addition of hydrogen. Much of the flow is accelerated to

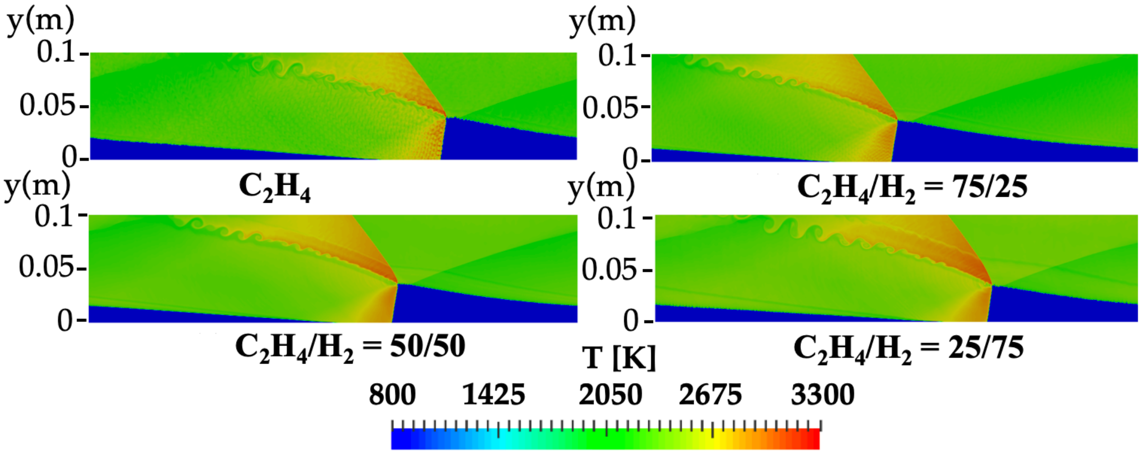

Figure 3.5: Temperature fields for different CH_4/H_2 cases with $P^0_{inj} = 30$ atm, $P_{back} =$ 14 atm and $T^0_{inj} = 793$ K.

approximately Mach 2, which is roughly the CJ speed expressed in terms of the speed of sound post detonation. Note that the ethylene cases exit to ambient conditions. On the other hand, the methane simulations show a more complex behavior. Due to the higher back pressure, the flow is restricted by tertiary shock structures that increase the static pressure (and temperature) while reducing the flow velocity. This is very clearly seen in the $P_{back} = 6$ atm case, which exhibits multiple shock structures in the post-detonation region. As the back pressure is further increased, the baseline pressure inside the combustor is higher, and the flow remains subsonic except near the contact surface and the detonation front. It is important to note that the pressure is not merely scaled when the back pressure is increased, but the flow itself is fundamentally altered.

3.4.3 Detonation structure with hydrogen addition

Further analysis is conducted using one-dimensional profiles extracted normal to the detonation front. Figure 3.9 shows the pressure profile across the detonation front for the two fuel mixtures, obtained at a height of 1cm above the bottom wall. For ethylene cases that have low back pressure, the pre-detonation pressure is slightly

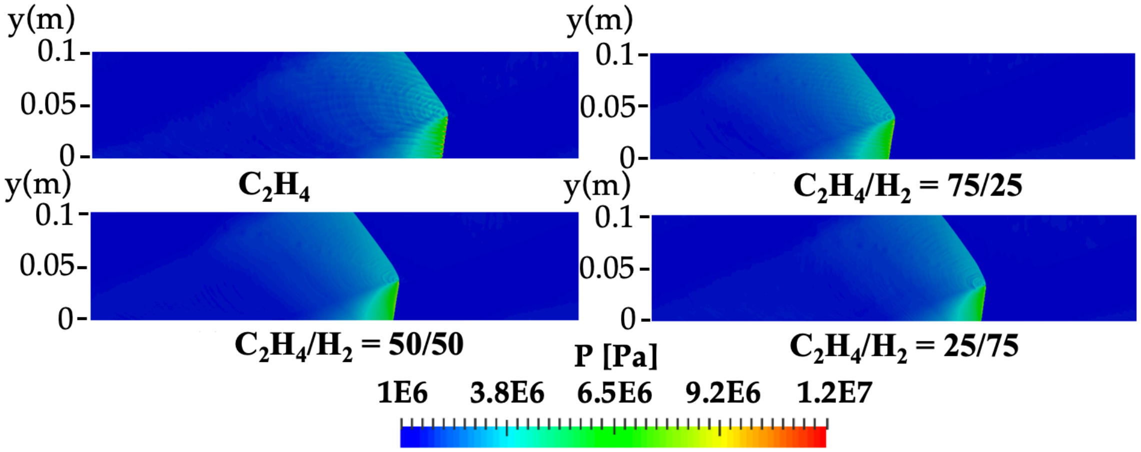

Figure 3.6: Pressure fields for different CH_4/H_2 cases with $P^0_{inj} = 30$ atm, $P_{back} = 14$ atm and $T^0_{inj} = 793$ K.

higher than 1 atm. For the methane cases, due to the high back pressure, this pre-detonation condition is closer to the back pressure value. As a result, the pressure increase across the detonation front is higher, which reduces the ignition delay time and leads to a stable detonation wave. Further, the pre-detonation pressure is invariant with distance from detonation front for the ethylene cases, but the increased back pressure leads to a change in pressure roughly 5mm ahead of the wave. It should be noted that when the back pressure is large, the flow can become unchoked leading to a reduction in mass flow rate. Figure 3.10 shows the peak pressure as a function of hydrogen content in the mixture, obtained at a height of 1cm above the bottom wall. For the ethylene case, the addition of hydrogen only leads to an 11 % decrease in peak pressure but for methane, an approximate reduction of 25 % is seen. As the peak pressure decreases, the initial acceleration of the flow past the shock wave is reduced, leading to lower Mach numbers post-shock-wave.

Figure 3.11 shows the fraction of heat release at a particular pressure range behind the detonation wave. The methane cases used $P^0_{inj} = 30$ atm, $P_{back} = 14$ atm and $T^0_{inj} = 793$ K. For the ethylene cases, the peak fraction of heat release occurs in the 35-40 atm pressure range, and is relatively unchanged with the addition of hydrogen.

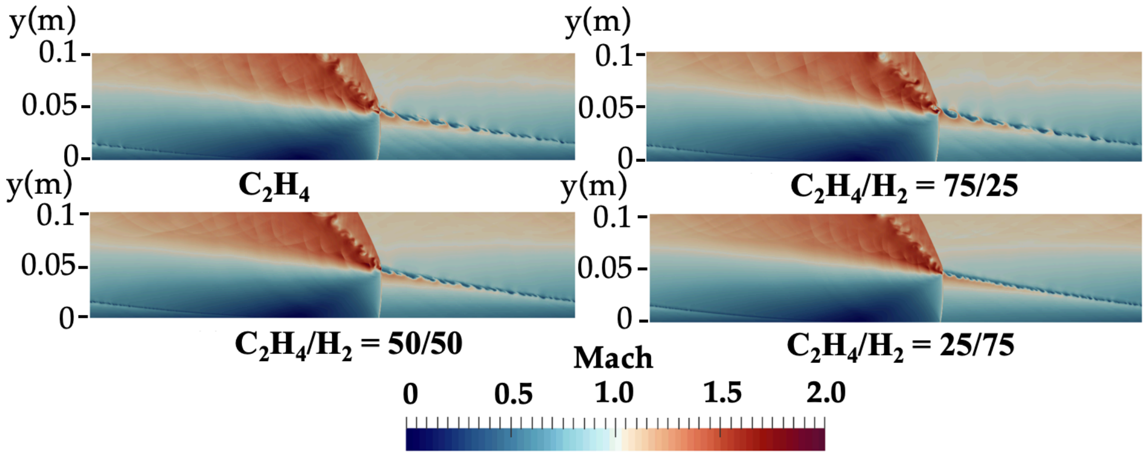

Figure 3.7: Mach number fields for the different C_2H_4/H_2 cases.

However, for methane, the peak heat release fraction switches from the 80-100 atm range to 60-80 atm range as the hydrogen content increases. Further, pure methane shows heat release at even higher pressures of 120-140 atm. Figure 3.12 shows the same heat release fraction, but for a one-dimensional detonation wave for the pure ethylene and methane cases. The ethylene/air case is described by $P_{inj}^0 = 10$ atm, $P_{back} = 1$ atm and $T_{inj}^0 = 300$ K; the methane/air case (bottom) is described by $P_{inj}^0 = 30$ atm, $P_{back} = 14$ atm and $T_{inj}^0 = 793$ K. Interestingly, the 1D case contains two peaks in heat release fraction for ethylene and a heat release fraction at lower pressure for methane. This indicates that the expansions behind the detonation wave as well as the interaction with the other regions in the domain alter the wave properties. As such, a direct use of one-dimensional models for predicting even two-dimensional detonation waves may not be accurate.

3.5 Summary and Conclusion

Numerical simulations of hydrocarbon chemistry were conducted with the ideal two dimensional configuration. The comparison between prior studies showed less than 5% error in terms of the thrust and the wave speed. With this verification,

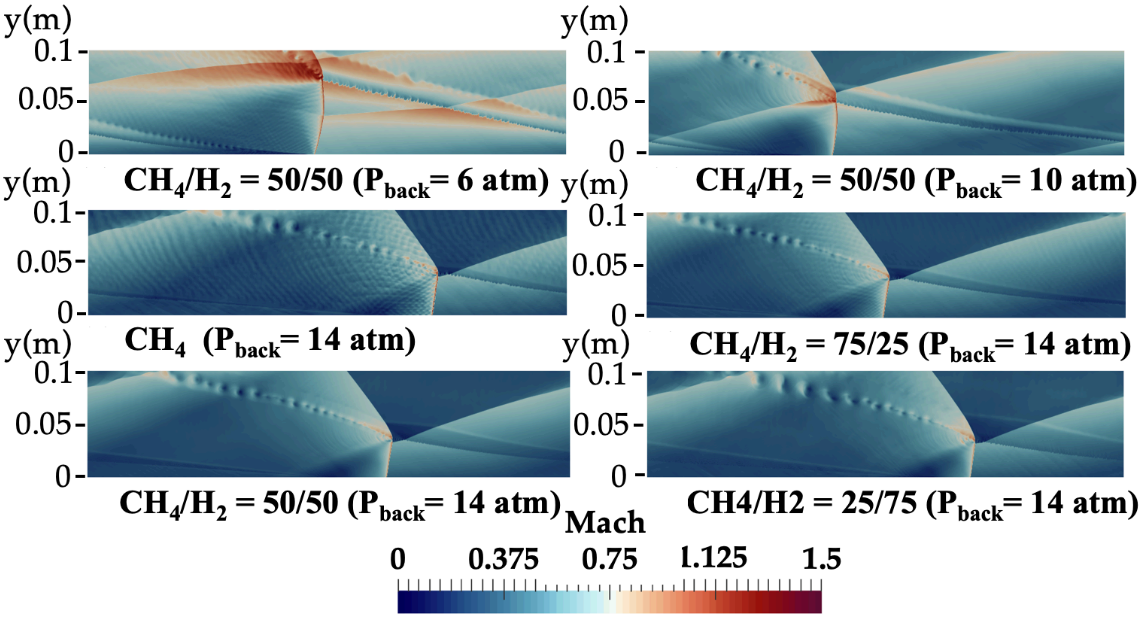

Figure 3.8: Mach number fields for the different CH_4/H_2 cases.

the ethylene and methane chemistry were simulated by adding hydrogen to asses its effect on the performance of the system and detonation structure. It was found that the methane chemistry could be detonated with only high injected pressure, likely due to its low detonability. As a general trend, it was found that adding hydrogen increases the wave speed and specific impulse due to its faster CJ velocity and small molecular weight. Furthermore, adding hydrogen decreases the peak pressure at the wave front. Lastly, the relation between heat release and pressure revealed that more heat is released in the higher pressure range with less hydrogen addition.

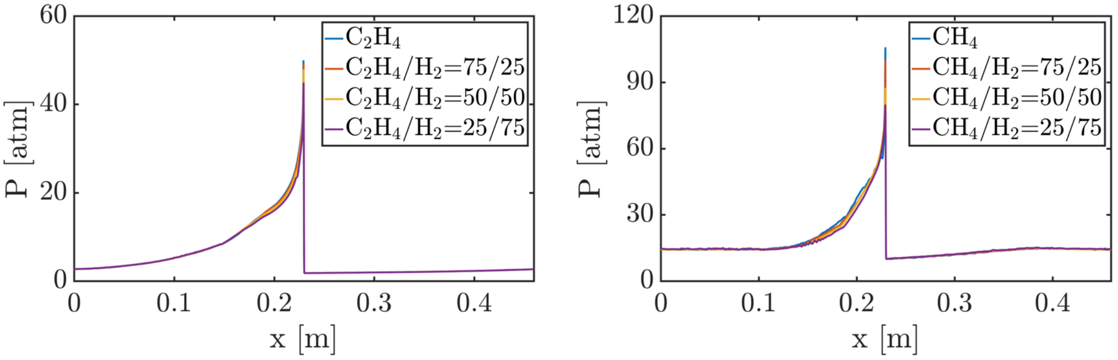

Figure 3.9: Pressure profile in the wave propagation direction obtained by time-averaging in the shock-reference frame. (Left) C_2H_4 and (right) CH_4 cases.

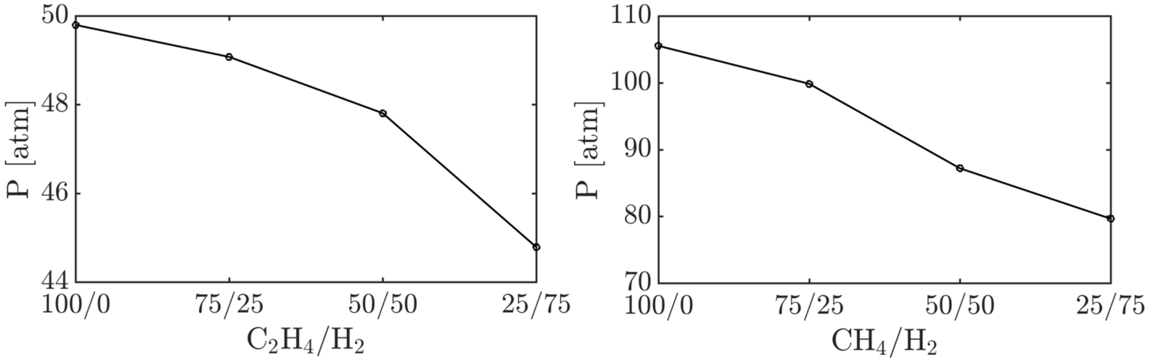

Figure 3.10: Variation of maximum pressure in the detonation region as a function of hydrogen dilution for (left) C_2H_4 and (right) CH_4.

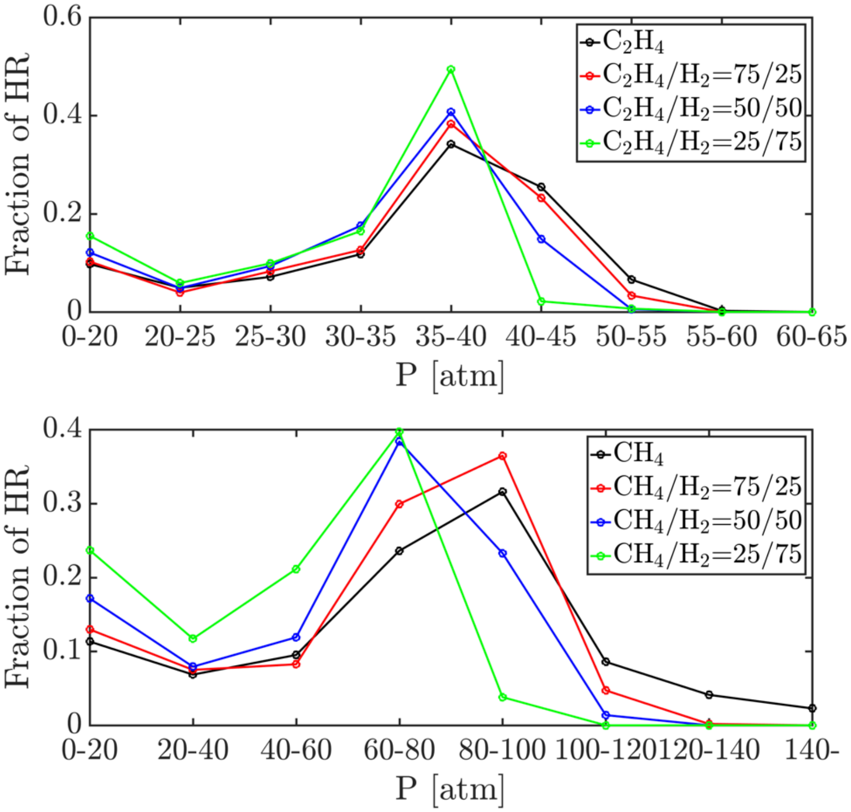

Figure 3.11: Heat release rate plotted as a function of the local pressure in the 2D RDE configuration for (top) C_2H_4 and (bottom) CH_4 cases.

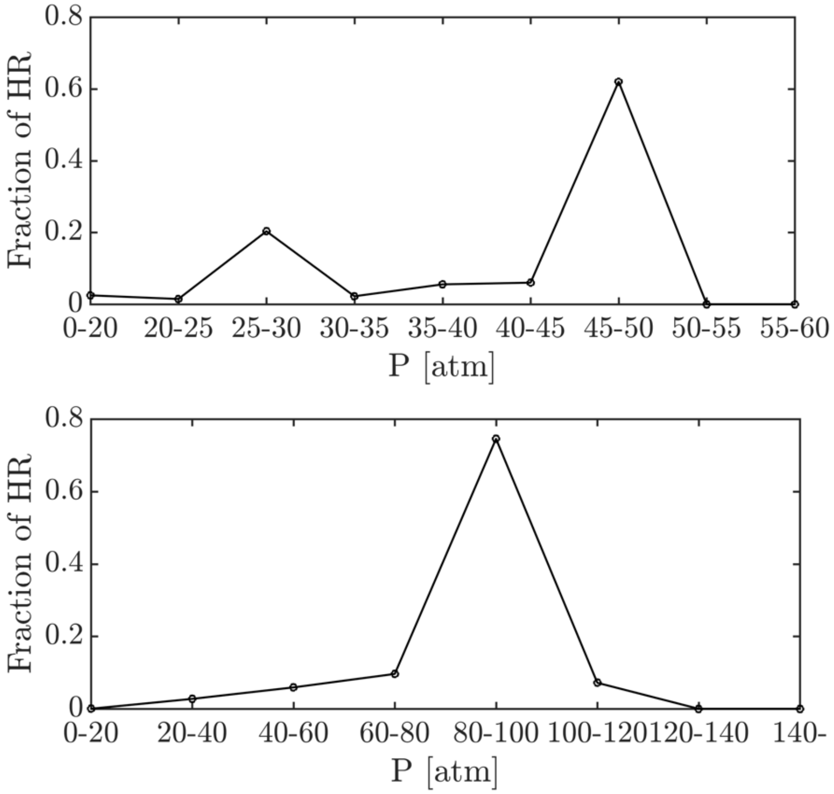

Figure 3.12: Heat release rates plotted as a function of pressure in the 1D configuration for (top) C_2H_4/air and (bottom) CH_4/air cases.

CHAPTER IV

Simulation of Radial Air Inlet Configuration

4.1 RDEs with a Radial Air Inlet

In the first application of the developed solver, a radial air inlet RDE at AFRL is simulated. In this configuration, the air is injected from the continuous inlet in the radial direction while the fuel is injected through discrete injectors at the bottom of the detonation chamber. The two flow streams intersect near the chamber bottom which creates the detonable mixture. The main focus of the current study is to extend the analysis of the AFRL experiments using high-resolution simulations of the detonation chamber and the upstream fuel/air plenums for a series of operating conditions. Hydrogen/air detonation with multiple mass flow rates but a fixed stoichiometric equivalence ratio is considered. Moreover, detailed chemical kinetics is used to ensure that mixture inhomogeneity caused by non-uniform and unsteady fuel/air flow profiles is fully captured. Finally, two kinds of the inlet boundary conditions, the total pressure boundary and the constant mass flow rate boundary, are examined. Analysis of instantaneous and cycle-averaged data is used to understand the detonation structure and injector dynamics.

4.2 Simulation Configuration for Grid Convergence

The computational grid used in this study is shown in Fig. 4.1. The simulation domain has been extended from the original experimental geometry in order to provide sufficient distance for the pressure waves at the detonation chamber exit to dissipate without reflecting back into the chamber. The main focus here is on the inflow section, where turbulent mixing as well as the reverse flow affect the dynamics of the combustor. The mesh is predominantly hexahedral. The post-detonation plenum contains very limited number of computational cells, designed specifically to numerically dissipate the waves. The minimum cell size in the detonation chamber is 2×10^{-4} m, which is smaller than the induction length for a premixed hydrogen/air detonation at these conditions. Prior analysis indicates that the detonation structures are weaker in such discrete injector configurations, with a significant deflagration region behind the shock [37, 71]. As seen in the results section that follows, the detonation structures span several grid points in the calculations. Both of the total pressure boundary condition and the constant mass flow rate boundary condition are used at the inflow planes for the oxidizer and fuel plenums, while zero gradient boundary conditions are used at the exit plane in the post-detonation plenum. No-slip and adiabatic wall conditions are applied to all simulations in this paper.

Similar to other studies [72], it was observed that the time required to reach steady detonation operations is highly dependent on the simulation initiation approach. Here, the following procedure is used. First, the fuel and oxidizer streams are allowed to propagate through the plenum into the detonation chamber without any ignition. For this purpose, the fuel and oxidizer plenums are filled with their corresponding gases, with initial conditions of boundary total pressure and boundary total temperature. At the second step, chemical reactions are suppressed and the jets allowed to mix in the detonation chamber. Once choked flow is established at the injectors, and the mixing structure does not change appreciably, high pressure, tem-

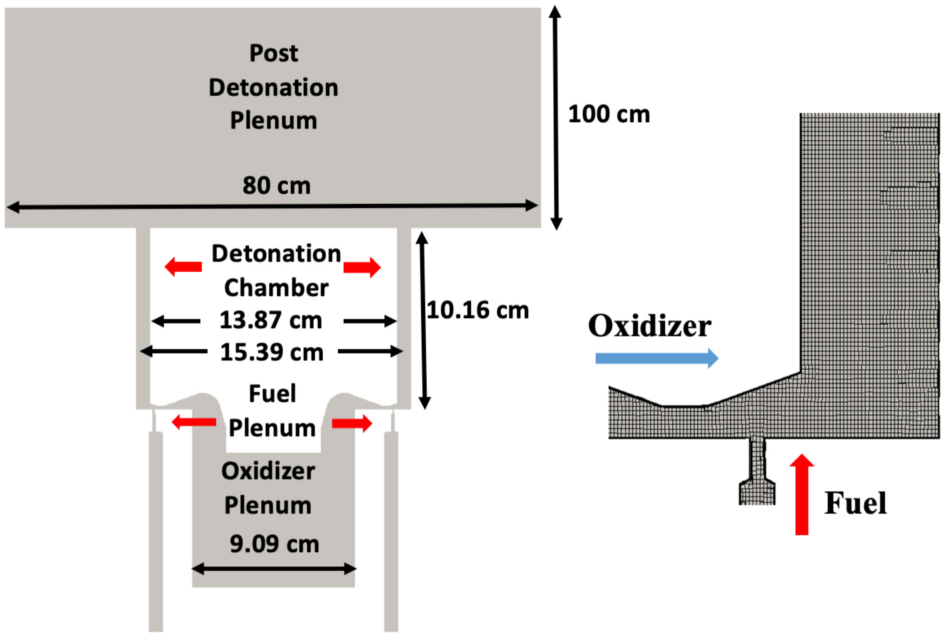

Figure 4.1: Simulated RDE configuration and computational mesh near a single injector region.

perature, and velocity conditions corresponding to one-dimensional post-detonation values are patched onto a small volumetric region inside the detonation chamber. This serves to spark a detonation wave with a chaotic flow environment. The detonation wave establishes over some transient time, after which steady operation is observed. All discussions below are based on results over 10 cycles after the first 15 cycles to ensure that the steady state mode of operation is achieved.

4.3 Results

4.3.1 Grid convergence

To author's knowledge, the refinement study for the full system RDEs simulation has not been studied in the community while it has been thoroughly evaluated for the 1D and unfolded 2D RDE configuration [47, 73, 74]. Unlike those simplified configurations, the resolution in the full system simulation would affect 1) incomplete detonation process due to the non-premixed injector, 2) the downstream flow field due to the numerical dissipation, 3) the macroscopic performance of the system such as the wave speed, thrust, and the specific impulse. With this mind, before discussing the detailed physics of the full system RDEs simulation, the grid convergence study is discussed in this section.

For the refinement study, three different grids are used. The base mesh has the 2×10^{-4} m (40 million control volumes) in the detonation chamber. This base resolution is decided based upon the convergence study of the 1D detonation tube problem [73] and prior full system RDEs simulations [52, 75–77]. The coarse mesh and fine mesh are simulated to investigate the resolution effect on the simulation RDEs. The resolution of the coarse mesh and fine mesh is 4×10^{-4} m (10 million control volumes) and 1×10^{-4} m (76 million control volumes), respectively. For the fine mesh, 1×10^{-4} m is given to 3 cm height at the chamber bottom to resolve detonation waves and the other region of the chamber is set to 2×10^{-4} m. The simulation is conducted with NS equations with non-slip and adiabatic walls. Since the flow in the chamber is dominantly supersonic due to the detonation waves and the chocked injectors, additional refinement is not given near the wall in this grid convergence test while it is taken into account for the main simulation with the total pressure boundary condition (Sec. 4.3.2). For the fuel and oxidizer inlet boundary, a total pressure boundary of 239 kPa and 276 kPa, respectively, is used as shown in Tab. 4.1.

Case	P^0_{oxi} [kPa]	P^0_{fuel} [kPa]	$\#^{waves}_{Expt.}$	$\#^{waves}_{Sim.}$	$\bar{P}^{2.54cm}_{Expt.}$ [kPa]	$\bar{P}^{2.54cm}_{Sim.}$ [kPa]	$W_{Expt.}$ (m/s)	$W_{Sim.}$ (m/s)	$F^{Sim.}$ [N]	$I^{Sim.}_{sp}$ [s]	$m^{Sim.}_{oxi}$ [kg/s]	$m^{Expt.}_{oxi}$ [kg/s]
1.coarse	239	276	1	1	139	138	1700	1768	276	4512	0.282	0.32
1.base	239	276	1	1	139	138	1700	1779	287	4494	0.278	0.32
1.fine	239	276	1	1	139	136	1700	1759	280	4333	0.284	0.32

Table 4.1: Details of the test cases of the resolution study as well as summary of macroscopic results from the simulations compared against experimental data.

4.3.1.1 General flow-field comparison

Figure 4.2 shows the pressure field on the outer wall, mid-channel, and the top view at 1 cm above from the chamber bottom for each grid. A self-sustained detonation wave is observed with all tested grids in this study. The wave vertically stands followed by an oblique shock wave. The detonation front is almost flat in the radial direction with more compression near the outer wall. With regard to the detonation height, the angle of the oblique shock wave, the vertical detonation front, the pressure propagating back to the plenum system, and the number of the waves, no particular differences are not observed although there are minor grid effects on the flow field. For example, the high-pressure region in the post-detonation gets broader as the grid is refined. This is because the sharp pressure gradient caused by detonation waves dissipate out as the grid is coarsened. The dissipation comparison in the axial direction of the chamber will be compared in the next subsection.

4.3.1.2 Axial pressure distribution

With regard to microscopic performance, the axial averaged pressure obtained in the simulation and CTAP data from the corresponding experiment is compared in this section. For the simulation data, the numerical probes are put at the same location as the experiment. The axial averaged pressure for the coarse, the base, the fine, and the experimental data is shown in Fig. 4.3. 0 cm corresponds to the bottom of the detonation chamber. Overall, all grid refinement cases are in good agreement with the experiment. Near the chamber bottom, the profile exhibits relatively higher pressure due to the detonation wave. This pressure rise gradually decreases by the 3 cm axial location which corresponds to the detonation height. The higher pressure near the bottom suggests that the mixing process is active in this region, which will be further discussed in Sec. 4.3.2.4. The pressure at the first point is under-predicted in comparison to the experiment because of the under-predicted mass flow rate at

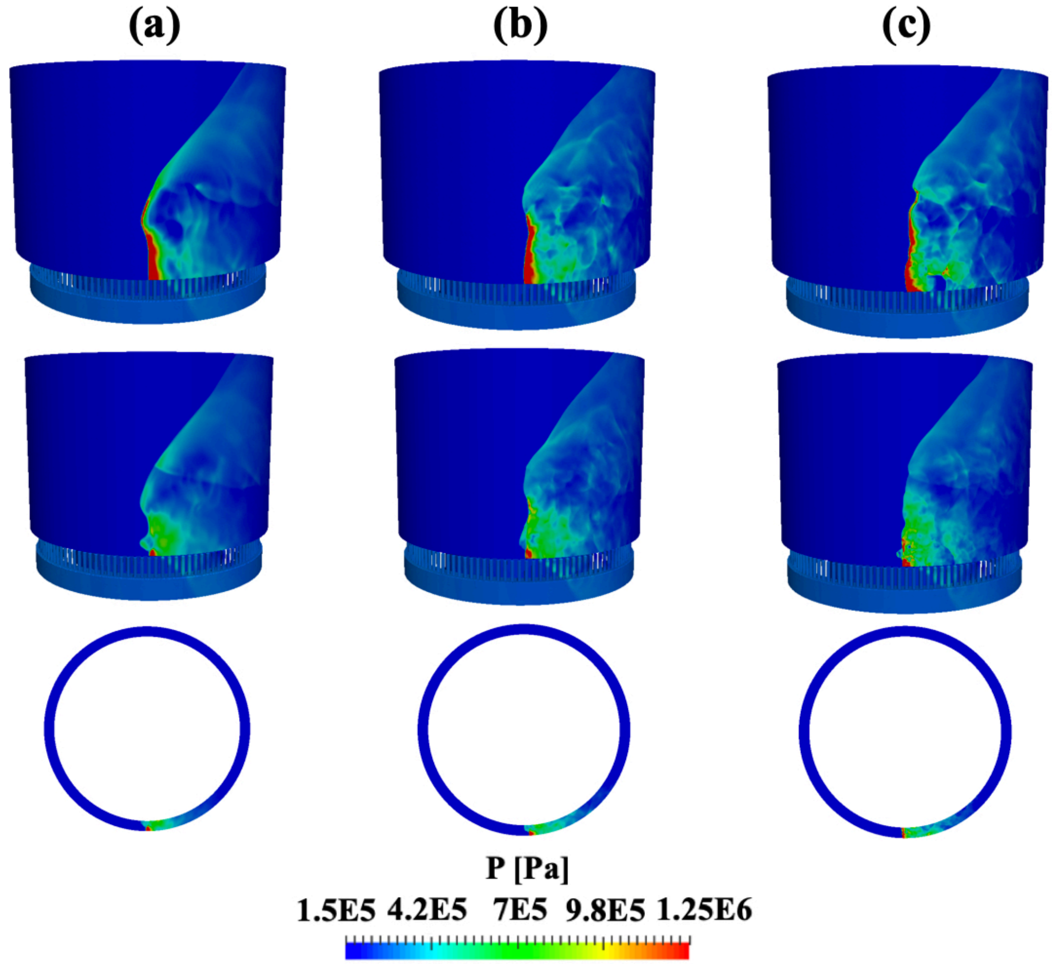

Figure 4.2: Pressure field of RDE with different resolution mesh. (a) coarse mesh case, (b) base mesh case, (c) fine mesh case

the injection exit, which will be explored in Sec. 4.3.2.6 and 4.3.2.10. Downstream of the detonation wave, the product gases expand towards the exit as pressure gradually decreases. Overall, the axially-averaged pressure for all grid resolution cases is almost indistinguishable. This result concludes that the coarse mesh (4×10^{-4} m) does not deteriorate the averaged profile of the detonation wave and the downstream flow field due to the numerical dissipation.

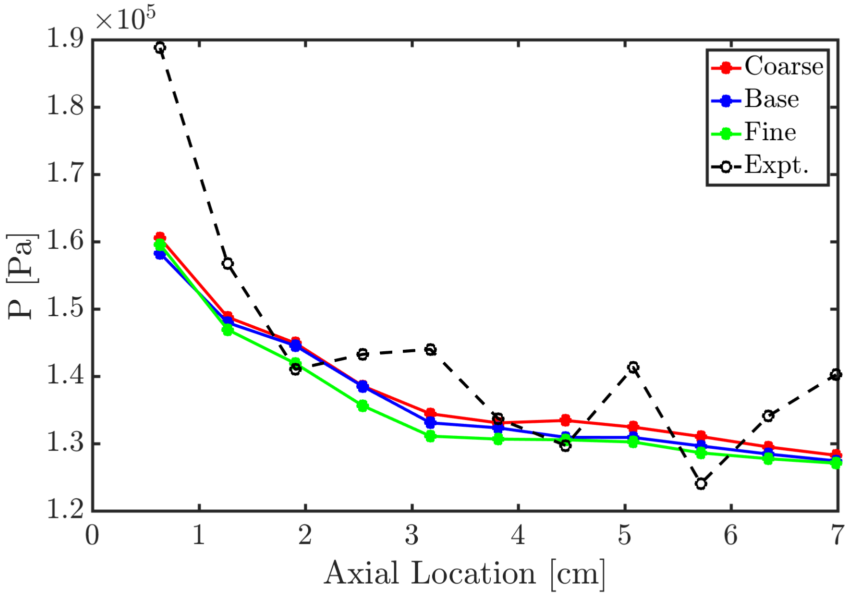

Figure 4.3: Comparison of pressure measurement on the chamber wall between simulation and experiment for the resolution study.

4.3.1.3 System performance convergence

Finally, the macroscopic performance of the system is compared for all grid resolutions. First, the averaged pressure at 2.54 cm above the chamber bottom is extracted. It is found that the values are in very good agreement with the experiment for all tested grids. Regarding the wave speed, all grid resolutions show a wave speed within 5% error of the experimental value. The wave speed is converged even with the coarse mesh which is a similar observation to the 1D detonation tube problem [73]. For the upstream and downstream comparison, the air mass flow rate, the thrust, and the specific impulse are extracted. For both of the air mass flow rate and the thrust, the errors are within 4% for each case which suggests that a mesh coarsened/refined by a factor of 2 does not affect the pressure propagation into the plenum system and the dissipation process in the downstream region. With this resolution study in mind, the base grid size ($2{\times}10^{-4}$ m) is used for the main simulation.

4.3.2 Main simulation

4.3.2.1 Simulation with the total pressure boundary

With the results from the resolution study, the grid size for the main simulation is set to 2×10^{-4} m. The geometry is the same as the resolution study as shown in Fig. 4.1. For the main simulation, two kinds of boundary conditions, total pressure boundary and constant mass flow rate boundary, are imposed on the fuel and oxidizer inlet for each case. To assess the boundary effect, layers are added near the wall to resolve the boundary layer for the total pressure boundary cases although the diffusion effects are limited in the system due to the predominantly supersonic flow [77]. A grid with a near-wall resolution is 2×10^{-5} m, stretching with a ratio of 1.15 to the base resolution, which results in the 58 million control volumes. This resolution in the layer is less than $y+ = 50$ in most of the domain. No-slip and adiabatic conditions are employed [52]. The complete mesh contains roughly 60 million grid cells. The simulations are run on the NASA Pleiades supercomputing cluster with 6,000 cores. The wall time is roughly a month to complete each case.

For RDE operation, it is critical to investigate how the plenum pressure in the plenum (i.e. the resulting mass flow rate) would affect the flow field and performance of the system. The prior experiment reveals that increasing mass flow rate impacts the detonation height, detonation strength, and the number of waves in the chamber [3]. Although these macroscopic parameters are available as experimental data, it is hard to capture the flow field due to the extremely harsh environment in the facility. With this mind, three different cases corresponding to experimental operating conditions are simulated in this study [3]. The simulations are initiated in the same manner as described in the previous section. For the total pressure boundary simulations, the total pressure is set to the values tabulated in Table. 4.2, and the total temperature on the inlet is set to 300 K. The data is extracted after the flow fields reach the steady state mode of operation (at least after 15 cycles).

Case	P^0_{oxi} [kPa]	P^0_{fuel} [kPa]	$\#^{waves}_{Expt.}$	$\#^{waves}_{Sim.}$	$\bar{P}^{2.54cm}_{Expt.}$ [kPa]	$\bar{P}^{2.54cm}_{Sim.}$ [kPa]	$W_{Expt.}$ (m/s)	$W_{Sim.}$ (m/s)	$F^{Sim.}$ [N]	$I^{Sim.}_{sp}$ [s]	$m^{Sim.}_{oxi}$ [kg/s]	$m^{Expt.}_{oxi}$ [kg/s]	$m^{Sim.}_f$ [g/s]	$m^{Expt.}_f$ [g/s]
1_{P_0}	239	276	1	1	139	139	1700	1736	287	4302	0.288	0.32	6.8	9.3
2_{P_0}	431	503	1	1	213	216	1740	1909	699	5496	0.538	0.63	13	18
3_{P_0}	611	709	2	2	311	234	1690	1797	1087	5874	0.764	0.86	18.9	25
$1_{\dot{M}}$	266	337	1	1	139	145	1700	1884	318	3402	0.32	0.32	9.5	9.3
$2_{\dot{M}}$	509	632	1	2	213	190	1740	1837	774	4338	0.62	0.63	18	18
$3_{\dot{M}}$	705	881	2	2	311	253	1690	1877	1178	4858	0.83	0.86	25	25

Table 4.2: Details of the test cases with the total pressure boundary and the constant mass flow boundary as well as summary of macroscopic results from the simulations compared against experimental data.

4.3.2.2 General behavior (total pressure boundary)

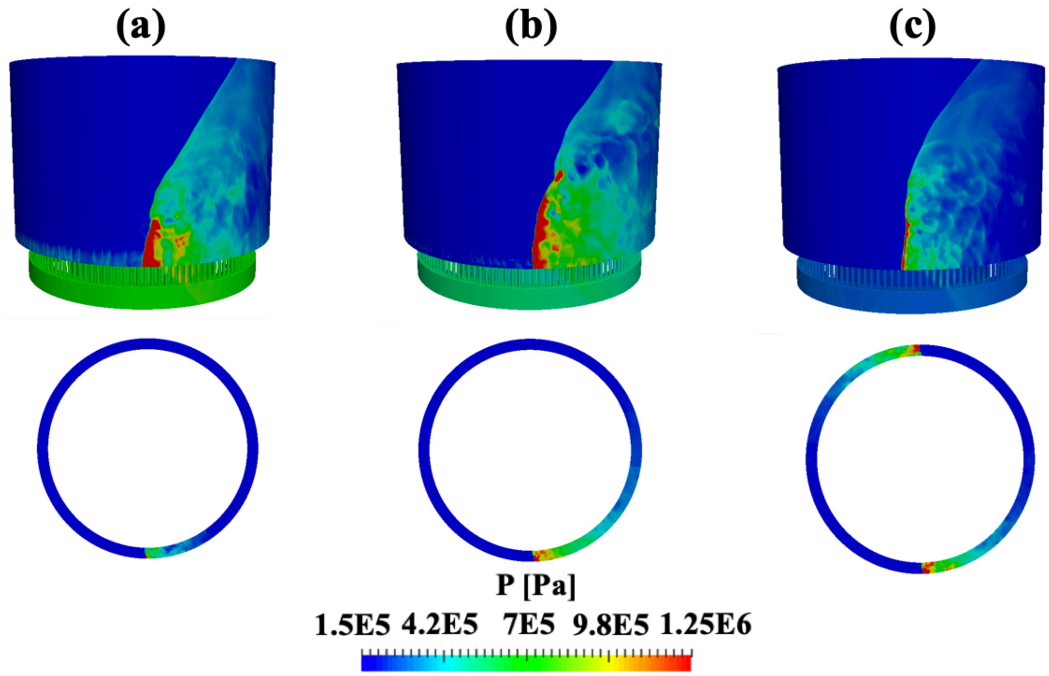

Figure 4.4: Pressure field of RDE with different injection conditions using the total pressure boundary condition. (a) case 1, (b) case 2, (c) case 3.

Figure 1.3 shows the characteristic features of the RDE flow field at a given time instant. The most notable feature is the detonation front, which shows a relatively non-smooth surface unlike a typical premixed detonation wave [47]. A linear profile of fill height is observable in the unreacted gases ahead of the wave, with the highest

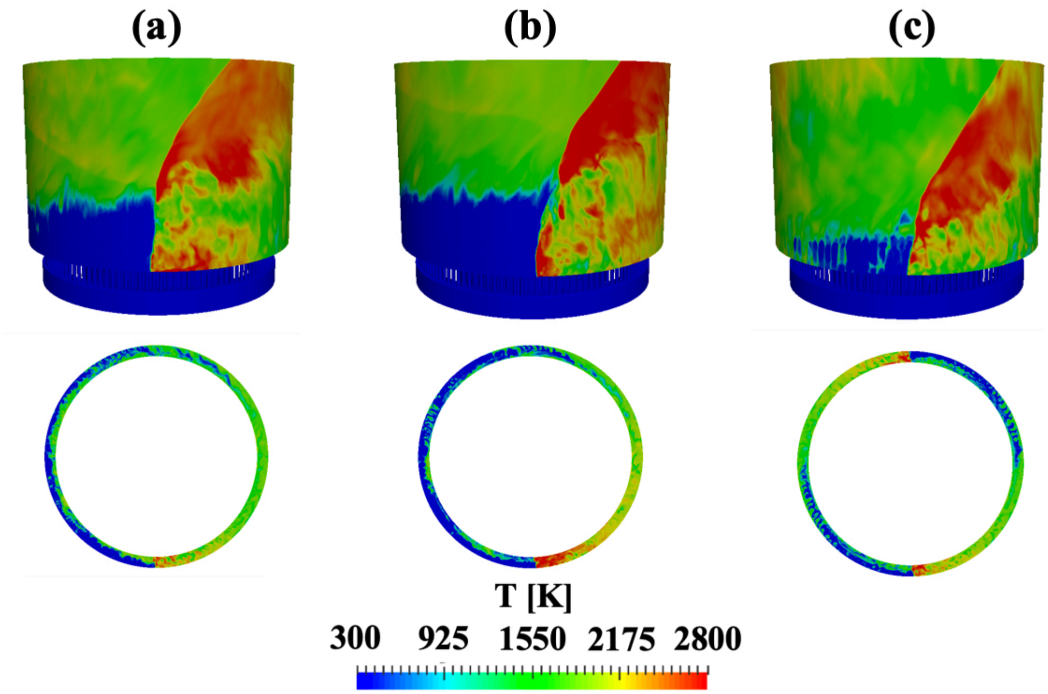

Figure 4.5: Temperature field of RDE with different injection conditions using the total pressure boundary condition. (a) case 1, (b) case 2, (c) case 3.

axial penetration observed close to the detonation front. This is due to the fact that as the detonation wave passes over the injectors, it blocks these feed streams. The expansion behind the detonation wave decreases the pressure after a finite distance, which allows the feed streams to resume the injection of fuel and oxidizer. This delayed response causes the characteristic slope of the fill heights. The product gases expand towards the outflow, which produces a change in the flow direction. Moreover, the interaction of the detonation wave with the product gases creates an oblique shock wave. Note that the effect of the passing detonation wave will be observed within the injection plenum as well, depending on the particular design. These features and the injector response will be discussed in more detail in Sec. 4.3.2.4. Since the exit to the combustion chamber is open to the atmosphere, the detonated products will be expanded out through the exit plane.

As a starting point, the instantaneous pressure field highlighting the detonation wave at the outer wall and from the axial cross-section at the 1 cm height above the chamber bottom for the three cases are shown in Fig. 4.4 at a given time instant. It is seen that cases 1 and 2 showed a single wave, while case 3 showed a two-wave system, which matches the corresponding experiments. Prior studies have postulated that the number of waves is based on the cell size and the fill height [16]. Consistent with the presence of multiple waves, the height of individual detonation waves decrease with increasing plenum pressure (mass flow rate). Figure 4.4 also shows that the detonation wave is stronger near the outer wall than the inner wall. Further, the front appears curved normal to the wall, with a trailing weaker detonation or deflagration front near the inner wall. With increasing plenum pressure, case 2 and case 3 are able to form the detonation waves in the mid-channel region. It is also seen that the pressure in the post-detonation region decreases for case 3 most likely due to the existence of multiple waves.

Figure 4.5 shows the temperature field on the outer wall for each case. For all cases, the temperature field captures the similar detonation structure to that of the unfolded 2D RDE simulations [47, 78]. The detonation waves convert the re-filled unreacted gases (the blue region near the chamber bottom) into the product gases. The oblique shock wave is formed from the top of the detonation front which propagates towards the outlet. While the unfolded 2D RDEs simulation reveals the vortex structure caused by the contact surface below the oblique shock wave, it is not clear in the full system simulations. For case 3 (two-wave mode), it is seen that the re-filling height is almost half of the other cases (one-wave mode). This height is almost the same as the detonation height, indicating that the detonation height is controlled by the re-fill height. Finally, the axial cutting planes at 1 cm above the chamber bottom are compared. Case 2 reveals a higher temperature in the broader post-detonation region than that of case 1, indicating that more heat is release across the wave front with increasing plenum pressure (the mass flow rate). However, this region becomes shorter for case 3 as splitting the waves into multiples. Detonation waves are weaker as the amount of the mixture a wave consumes becomes smaller due to the limited re-filling and lower mixing time scale with an increased number of waves. An interesting point here is that the product gases for case 3 are replaced with the freshly re-filled gases by nearly quarter cycle while it takes at least half a cycle for case 1 and case 2. This indicates that the re-filling time scales adjust to the number of waves to keep the waves self-sustained, which will be discussed in Sec. 4.3.2.4.

4.3.2.3 Detonation structure with a radial air inlet

To assess the more detailed dynamics in the chamber and compare to the idealized 2D calculation [47, 78], it is useful to look at the unwrapped flow-field extracted from the full system simulation. Figure 4.6 and 4.7 show the unwrapped flow-field of pressure, temperature, equivalence ratio, and mach number extracted at the mid-channel of the detonation chamber. Compared to the flow field on the outer wall, the unreacted region at the mid-channel shows a more stratified structure. This stratified structure is a result of two primary reasons. First, the product gases are not completely pushed away due to the freshly re-filled gases. This incomplete re-filling structure induces the weaker detonation than that of CJ values. The second reason is that the mixture is not completely mixed due to the non-premixed injector scheme. The mixing process likely depends on the mass flow rate as well as the injector types employed for the system [75].

Figure 4.6 also reveals that the mixture is pre-burnt at various locations before the wave, which is consistent with observations of a different injector scheme through both experiment and simulation [23, 75]: a contact burning region (CB) separates the parasitic combustion (PC), where the mixture begins burning in the pre-detonation region, and the buffer region (BR), where the refilling process is more dominant than the parasitic combustion. With the injector scheme in this study, BR appears near the chamber bottom while the axial air injector scheme reveals that PC occurs near the chamber bottom [23, 75]. It is reported that the parasitic combustion makes the detonation wave weaker, which reduces the wave speed and peak pressure at the wave front [23, 75–77]. This structure is seen for all cases regardless of the number of waves (mass flow rates). It is suggested that such a structure depends on the mixing process in the chamber that is enforced by a certain injector scheme.

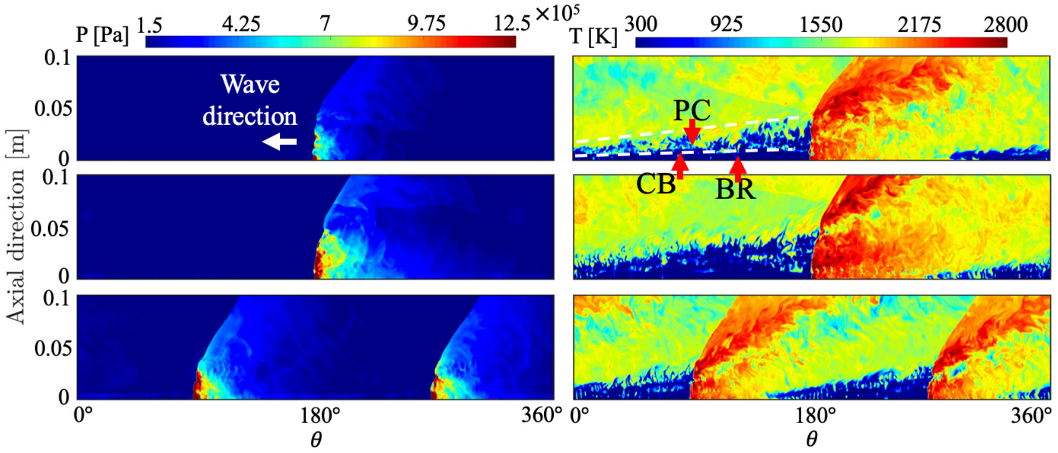

Figure 4.6: Pressure and temperature on the unwrapped plane at the mid-channel with the total pressure boundary. Top: case 1, middle: case 2, bottom: case 3.

The equivalence ratio profile in Fig. 4.7 gives more insight into the parasitic combustion region. Near the chamber bottom, the poorly-mixed fuel and air are present which correspond to the BR region. At a certain distance from the chamber, $\phi = 1$ begins appearing which can be consumed as parasitic combustion. Generally, the parasitic combustion can be induced by the residual product from the previous cycle and the secondary wave [23, 75–77]. Finally, the mach contour also reveals an interesting structure. For case 1 and 2, the contact surface (CS) can be found across which the mach number decreases. Due to the CS, both subsonic and supersonic flow comes out from the chamber depending on the azimuthal location. A structure similar to the CS is also found in the idealized 2D calculation [47, 78]. For case 3, however, the CS disappears and only supersonic flow comes out at the exit. In other words, increasing the mass flow rate enables the elimination of the CS that decelerates the expanding flow in the post-detonation region. For a real RDE system, the supersonic flow does not allow any feedback from the exhaust system attached to the exit of the chamber.

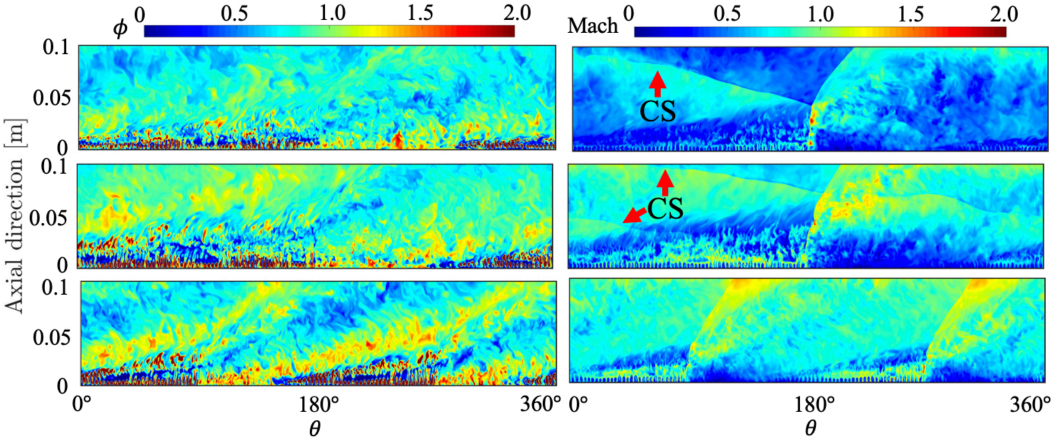

Figure 4.7: Equivalence ratio and mach number on the unwrapped plane at the mid-channel with the total pressure boundary condition. Top: case 1, middle: case 2, bottom: case 3.

4.3.2.4 Phase averaged and injection behavior

The previous section discussed the detailed detonation structure on an unwrapped flow-field in the circumferential direction. It will be useful to look at the flow-field from a different angle because of its highly three-dimensional structure. Figure 4.8 shows azimuthally averaged temperature and mixture fraction on an injection cutting plane. The color bar for the mixture fraction is limited between 0 to 0.1 because the stoichiometric mixture fraction is at $Z_{st} = 0.0284$. The temperature profile reveals a similar structure for case 1 and 2 regardless of the difference in the mass flow rate. The low temperature appears near the chamber bottom due to the re-fill mixture that is followed by gradually increasing temperature towards the exit. This temperature distribution matches the observation on an unwrapped flow field where the mixture is burned near the bottom and the product gases expand in the post-detonation region. Interestingly, case 3 reveals that the high temperature appears near the outer wall at the bottom. This is likely due to the multiple waves in the system which impose high

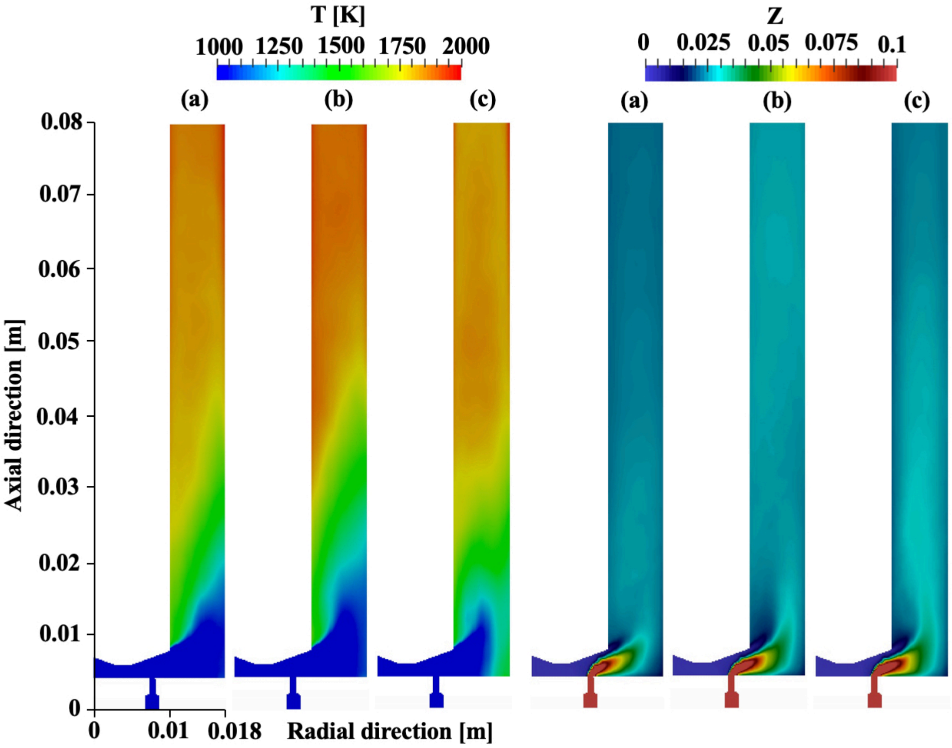

Figure 4.8: Azimuthal averaged temperature and mixture fraction for (a) case 1, (b) case 2, and (c) case 3 with the total pressure boundary condition.

temperature products gases near the outer wall more frequently.

For the mixture fraction, it is seen that the fuel stream is pushed into the chamber due to the axially flowing air stream for all cases. After flowing into the chamber, those streams start to actively get mixed. The stoichiometric region appears 1) at the intersection between the fuel and air streams and 2) at some intermediate distance between the chamber and outer wall most likely due to the recirculation in the area. It is also seen that the air stream hits the outer wall and creates the lean layer near the outer wall (note that the air inlet is circumferentially continuous across 360 degrees while the fuel injector is spaced discretely.). With increasing mass flow rate, the stoichiometric region extends to the downstream region as well.

The mixing process is highly chaotic for RDE systems due to the non-premixed injection scheme. It is not just because the fuel and air are separately injected, but also because the injector experiences momentary blocking/flashback due to the

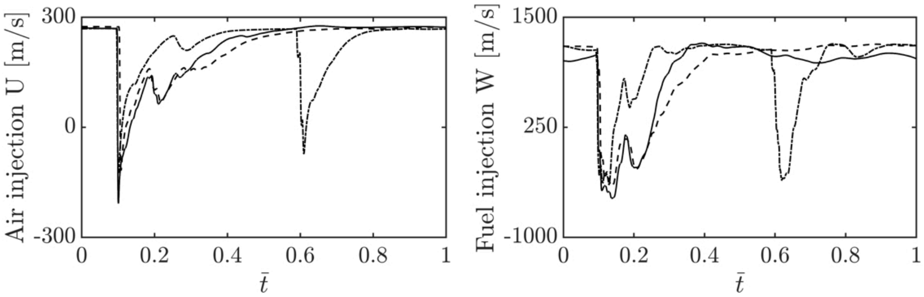

Figure 4.9: Variation in injection velocity with cycle-averaged time for oxidizer and fuel inlets with the constant mass flow boundary condition. The solid line, dashed line, and dotted line show case 1, 2, 3, respectively.

detonation wave in the chamber. After the injector is shut down, it takes some recovery time to restart the refilling process into the chamber. These dynamics adds complexity to the mixing process of RDE system. With this mind, it is critical to assess the injection dynamics over a cycle for both of the fuel and air injectors.

Figure 4.9 shows the averaged injection velocity for the fuel and air inlets as a function of cycle-normalized time. The sudden drop in the velocity shows that both injectors are blocked as the detonation wave passes. Only case 3 reveals two flashbacks over a single cycle due to the two-wave operation mode. For case 1 and 2 (one-wave mode), the velocity quickly recovers after a sudden suppression. For the air inlet, the velocity profile curve takes about a half cycle to recover to the original value. Interestingly, case 3 illuminates that the recovery time-scale adjusts to the number of waves in the chamber, and the recovery process is complete such that the system can sustain the multiple waves. This observation matches the temperature field in Fig. 4.5 and 4.6 where the refilling is sufficiently completed in order to sustain the multiple waves. For the fuel injection, flashback also can be observed although the dynamics slightly differ from that of the air injector. The diminished flow velocity state stalls at the minimum point for a certain duration. It is computed as such because the velocity of the fuel injector shows large fluctuation near the minimum point out before starting the recovery process. After the stalled point, the velocity sharply recovers to the original value rather abruptly. The stiff dynamics of the fuel injector is also seen for case 3 with the multiple wave mode. This asymmetry in the recovery process between the fuel and oxidizer injectors form a complex mixing profile in the chamber that leads to a highly chaotic detonation structure.

4.3.2.5 Averaged shock-normal profile

The last section reveals that the detonation structure is highly chaotic due to the non-premixed injection that has a different recovery time-scale. While ZND theory suggests that the sharp pressure rise at the wave front induces the high rate of chemical reaction in the post-region which makes the wave self-sustained, the structure could be different in RDE systems due to the complex dynamics mentioned above. As such, it will be useful to look at the profiles across the wave in RDE systems to understand the detailed flame structure.

To determine the structure of the detonation wave itself, a time-averaged profile in the wave reference frame is obtained. The flow properties are extracted across the wave front at the mid-channel diameter 1 cm above the lower wall of the detonation chamber. Figure 4.10 shows the profiles in terms of the distance from the shock front. The product gases from the previous cycle can be seen in the post-detonation region as mentioned in Sec. 4.3.2.3. The oxidization process can be seen for every case where the fuel and oxidizer are consumed to produce fresh products causing a sharp increase in the pressure. Nevertheless, the oxidization process is significantly weaker compared to the ideal case [73]. Comparing cases 1 and 2, the peak of the heat release is closer to the wave front for case 2. This is indicative of the stronger detonation wave with increasing mass flow rate. For case 3, the heat release reaches its peak with a sharper gradient although the peak heat release appears at the similar location to case 2. The heat released in the narrower region supplies more energy to the wave front, which results in the peak pressure which is up to nearly 15 atm for case 3.

The relation between the compression and chemical reaction can be seen in the heat release and temperature relations. For all cases, the heat release sharply increases before that of the temperature. Furthermore, the temperature is nearly at 1000 K before the wave front where the finite value of the heat release also can be seen. This structure suggests that the reaction region extends across the wave due to parasitic combustion which causes the longer induction length and lower pressure peak value ($P_{CJ} = 27$ atm) at the wave front. This extension of the reaction zone becomes shorter with increasing mass flow rate (note that the x-axis is in log-scale.).

4.3.2.6 Axial pressure and macroscopic performance of the system

Finally, the axial variation in average pressure is considered. Table 4.2 shows the average pressure measured on the outer wall at 2.54 cm above the detonation chamber bottom wall for both experiments and simulations. For case 1 and case 2, the simulation is in good agreement with the experiment within 1.5% error. A more detailed comparison of wall pressure profiles is provided in Fig. 4.11. Overall, the chamber pressures decrease with increasing axial distance due to expansion effects. Although the simulations capture the experimental trend for case 1 and case 2, case 3 (two-wave mode) underestimates the axial averaged pressure. In other words, as waves split into multiples, the pressure rise due to the detonation is underpredicted in the simulation. Despite the difference for case 3 in the axial averaged pressure, the simulated wave speed is within 10% error of the experimental value as shown in Tab. 4.2. Compared to the result of the base mesh in the resolution study, the main simulation for case 1 which incorporates boundary layer refinement does not show particular differences. This result indicates that the diffusion effects are negligible in the system due to the predominantly supersonic flow. Finally, the fuel and air mass flow rate is compared between the experiment and the simulation. Overall, the simulation is in good agreement with the experiment with nearly 10% error for the air mass flow rate while the fuel mass flow rate is under-predicted by 25%. Note that the mass flow rate is calculated at the injector exit for simulation's data while it is measured at the upstream of the plenum system in the experiment. The total pressure boundary condition does not ensure the target mass flow rate into the chamber is met. To feed the target mass flow rate, the constant mass flow rate boundary is necessary, which will be discussed in the next section.

4.3.2.7 Simulation with the constant mass flow rate boundary condition

As Table 4.2 reveals for the total pressure boundary condition, the total pressure boundary can closely match the experimental plenum pressure at cost of increased error in the mass flow rate into the chamber. The error is due to various reasons: 1) the numerical error, 2) the mass flow rate is regulated at a location much upstream of the plenum system in the experiment while the mass flow rate is calculated at the injector exit in the simulations, and 3) the experimental plenum system has more complex geometry in the upstream region that is not modeled here. Another option for the inlet boundary condition is the constant mass flow rate boundary condition. The constant mass flow rate boundary condition ensures that the targeted mass flow rate is supplied into the chamber although the plenum pressure will converge as the simulation is run. The overall differences caused by those two types of boundary conditions will be discussed in Sec. 4.3.2.10.

The simulations with the constant mass flow rate boundary condition are conducted for the same experimental runs as the total pressure boundary condition. The simulated cases are tabulated in Table 4.2. For the mesh with the constant mass flow rate boundary condition, the base cell size is 2×10^{-4} m which is the same size as the total pressure boundary condition. The boundary layer refinement is not added as the previous simulations suggest that the diffusion effect at the wall is negligible. The extended plenum region in Fig. 4.1 is restricted to 2 cm below the detonation chamber for the constant mass flow rate boundary condition. This is done so that the plenum is easily pressurized by the pressure wave propagating back from the chamber to ensure the target mass flow at the injection exit. The total number of control volumes is 40 million. Each simulation takes approximately 2 weeks to complete using 3000 CPU cores on the NASA Pleiades supercomputer. The main goal of this simulation is to understand the effect of boundary condition on the simulated results and to give more insight to the community for the choice of the inlet boundary condition.

4.3.2.8 Detonation structure with the constant mass flow rate boundary

The unwrapped flow-field is shown in Fig. 4.12 in the same manner as Fig. 4.6. The constant mass flow rate boundary reveals a structure similar to the total pressure boundary condition with elemetns such as PC, CB, and BR. For case 2, the constant mass flow rate boundary splits the wave into two waves while the experimental observation suggests one-wave mode. It should be noted that the mass flow rate into the chamber is under-predicted with the total pressure boundary while the constant mass flow rate boundary captures the target mass flow rate very well. This difference can be explained by the higher plenum pressure with the constant mass flow rate as shown in Table 4.2. The constant mass flow rate boundary allows the plenum system to be pressurized due to the pressure waves from the chamber. The higher plenum pressure locally increases the pressure of the injected gases that affects the reactivity of the mixture. Because of the higher mass flow rate, case 1 reveals the higher detonation height with a single-wave mode. Interestingly, the height of BR region does not differ from that of the total pressure boundary while the PC region becomes taller. This suggests that the recirculation region becomes taller for the same number of wave with increasing mass flow rate.

The extended mixing region is also confirmed in Fig 4.13. The equivalence ratio flow-field finds that the broad region of $\phi = 1$ appears in the same region of the

PC. It should be noted that overall the equivalence ratio flow-field gets richer than those of the total pressure boundary cases because the fuel mass flow rate is underpredicted and the system experiences lean operation with the total pressure boundary condition. The mach contour also shows a similar trend to Fig. 4.7 although case 2 for the constant mass flow rate does not reveal the CS. This observation suggests that the number of waves controls the existence of the CS which affects the mach number (subsonic or supersonic) at the exit.

Nevertheless, despite the minor difference in the flow-field, the constant mass flow rate boundary generally reveals the same structure such as PC, BR, and CS on an unwrapped field with a total pressure boundary condition. It is critical that the general structure remains regardless of the inlet boundary conditions.

4.3.2.9 Averaged flow profiles and injection dynamics

This section will discuss the averaged profile on an injection cutting plane and the injection dynamics with the constant mass flow rate boundary. Figure 4.14 shows phase-averaged temperature and heat release on an injection cutting plane. The mixture fraction profiles are not shown here because they are very similar to the total pressure boundary in Fig 4.7. For case 2 and 3, the relatively high temperature (nearly 1500 K) appears near the edge of the chamber bottom and the outer wall. This observation is seen only for case 3 with the total pressure boundary condition which is the two-wave mode. This indicates that this region experiences more heating due to the higher frequency of the flame. Interestingly, it is seen that the temperature at locations downstream of the chamber is higher for case 1 (single wave) than the other cases. This suggests that the longer time-scale of evacuating product gases leads to hotter gases at the downstream locations.

The right figure in Fig. 4.14 shows the averaged heat release on an injection cutting plane. The value is normalized by the maximum heat release on the plane.

For all cases, the heat is released near the chamber bottom where the well-mixed mixture also appears, as shown in Fig. 4.8. The heat release appears not only in the detonation chamber but also in the injector region. Nevertheless, the injector prevents the heat release from entering into the plenum system due to the choked flow condition. Furthermore, there is less heat release near the inner wall for all cases, which is indicative of the poor mixing in those regions. In fact, the heat release can be seen at the intersection between the fuel and air streams and the recirculation region in Fig. 4.8. Case 1 and 2 reveals a relatively higher fraction of heat release in the broad region near the bottom while case 3 shows the local peak value at the intersection of the two streams. It is also seen for other injection geometries that the high heat release fraction is more spatially concentrated with increasing mass flow rate [24, 39].

Figure 4.15 shows the averaged injection velocity history over one-cycle with the constant mass flow rate boundary which is plotted in the same manner as Fig. 4.9. The velocity decays to negative values due to the pressure wave from the chamber for all cases with the constant mass flow rate boundary as well. For the air injection, the recovery time scale becomes shorter than those of the total pressure. This is because the higher plenum pressure induces the quicker response of the injectors as discussed in Sec. 4.3.2.8. For case 2, the two-wave mode with the constant mass flow rate boundary reduces the recovery time scale for each wave so that the refilling process can sustain the multiple waves. For the fuel injector, a trend similar to that of the air injector is visible. For a single-wave mode (case 1), the velocity recovers to the original value within nearly $\bar{t} = 0.15$.

4.3.2.10 Comparison between the total pressure boundary and the constant mass flow rate boundary

Lastly, the comparison between the total pressure boundary and the constant mass flow rate is discussed in this section. First, the axial pressure with the constant mass flow rate boundary is plotted in Fig. 4.16 in the same manner as Fig. 4.11. Overall, the simulation is in good agreement with the experimental CTAP data. The simulation result captures the general trend that the gases are compressed near the chamber bottom and expand towards the exit. Especially for case 3, the constant mass flow rate reveals better agreement with the experiment than the total pressure boundary case. This result indicates that the under-predicted mass flow rate with the total pressure boundary makes the detonation wave weaker than experimental observations.

With regard to the macroscopic performance of the system, the plenum pressure is over-computed in comparison to the experimental value (the total pressure boundary values). This is likely because the experimental plenum system has a longer and more complex geometry in the upstream region as discussed in Sec. 4.3.2.8. In terms of the mass flow rate at the injector exit, the total pressure boundary under-predicts the value by nearly 20% for both injectors lending to the differences in the detonation structure and the injection dynamics discussed in Sec. 4.3.2.9. For the wave speed, both of the boundary conditions over-predict than the experimental values. As the general trend for both boundary conditions, the wave speed increases for a constant number of wave with increasing the mass flow rate. The error in the wave speed is within 15% against the experimental values, which is of the same order as other prior studies [24, 39, 75].

Overall, the total pressure boundary and the constant mass flow rate boundary ensures agreement with the experiment in terms of different properties. The total pressure boundary can more accurately capture the plenum pressure and the wave speed compared to the constant mass flow rate boundary. However, it under-predicts the axial pressure distribution likely due to the erroneous mass flow rate. On the other hand, the mass flow rate boundary ensures the right amount of the mass flow rate into the chamber. The downside of this boundary condition is that the plenum pressure is higher than that of the experiment - this also indicates, however, that the longer plenum system in the experiment is causing some loss between the plenum pressure probe location and the location of the mass flow rate measurement. In terms of the axial pressure distribution, the constant mass flow rate boundary conditions reveals a better agreement with the experimental CTAP data.

4.4 Conclusions

A series of high-resolution RDE simulations using detailed chemical kinetics and the discrete injection process including modeling of the plenums was conducted. The use of detailed chemical kinetics provides a full view of the detonation structure. The simulation configuration is based on the AFRL 6-inch RDE experiment using hydrogen/air at stoichiometric conditions. Three cases, corresponding to three different plenum pressures and resulting mass flow rates, were studied with the total pressure and the constant mass flow rate boundary conditions. The simulations indicate that multiple waves can be sustained as higher mass flow rates are considered. Similar to the experiments, the waves become stronger, moving with faster velocities with increasing mass flow rate for the same number of wave modes.

Spatially, the detonation waves were stronger near the outer wall but devolved into strong deflagrations near the inner wall. The reason for the radial difference in detonation structure comes from the fuel/air stratification due to incomplete mixing. Simulations showed that the different stiffness associated with the injectors lead to non-uniform fueling of the detonation chamber, even when the global flow rates are steady in long-time averages. Most importantly, the injector recovery time scale adjusts to the number of waves in the chamber.

Regarding the detonation front structure, it is found that the residual product gases from the previous cycles remain, which could cause the incomplete combustion process. The parasitic combustion appears above the buffer region near the chamber bottom that is bounded by the contact burning region. For the lower mass flow rate, the contact surface decelerates the flow, leading to a subsonic outflow. As wave-splitting occurs, the contact surface disappears which results in the supersonic outflow. The temporally-averaged profiles on an injection cutting plane highlight that the averaged temperature structure varies depending on the number of waves in the chamber. For the multiple waves mode, the temperature near the outer wall at the chamber bottom increases because flames pass more frequently. The mixture fraction suggests that the mixing happens at some distance from the chamber. It is also found that the air stream hits and flows along the outer wall where the mixing is not enforced. With increasing mass flow rate, the mixing region broadens towards the downstream as well. The averaged heat release suggests that the reaction actively happens at the intersection of the fuel and air streams and in the recirculation region.

The cycle-averaged injection velocity reveals that the fuel injector generally exhibits the more stiff dynamics than the oxidizer. With increasing mass flow rate, the recovery process becomes stiffer due to the higher plenum pressure. The recovery time-scale adjusts to the number of the wave in the chamber such that the refilling is completed before the next wave comes in. The different time-scale of the recovery process between the fuel and oxidizer leads to the complex mixing with an incomplete and highly three-dimensional detonation structure.

The shock-normal profile shows that the structure across the wave is very different from the ideal detonation tube case. For case 1, the averaged peak pressure drops by more than 60% compared to the CJ value. The product gases appear in the pre-detonation region due to the parasitic combustion and the residual gases from the previous cycle which makes the wave weaker than the ideal detonation wave. The heat release profiles suggest that the reaction region is extended across the wave as well. It is also observed that the induction length becomes shorter with increasing mass flow rate.

The resolution study reveals that the macroscopic properties such as the wave speed, the oxidizer mass flow rate, the axially-averaged pressure, and the thrust converge even with the grid size of 4×10^{-4} m. This study employed a resolution of 2×10^{-4} m to capture the detailed profile across the wave although the resolution study indicates that one can use 4×10^{-4} m only to assess the macroscopic properties.

Finally, a comparison between the total pressure boundary and the constant mass flow boundary conditions are conducted. Overall, the detonation structures and the injection dynamics reveals a similar structure with minor differences caused by the different amount of the mass flow (the higher pressure in the plenum system). The constant mass flow rate boundary allows for an adjustment of the mass flow at the injector exit due to a pressurization process in the chamber. Due to this, case 2 operates with the two-wave mode for the constant mass flow rate boundary. The constant mass flow rate boundary ensures the target mass flow rate at the injector exit plane (nearly within 2% error) while the total pressure boundary reveals a much larger error (nearly 20%). Due to the higher pressure in the plenum for the constant mass flow rate boundary, the injection dynamics get stiffer than that of the total pressure boundary. Overall, the axial pressure, the wave speed, the oxidizer mass flow rate are in good agreement with the experiment. The only exception is the axially-averaged pressure for case 3 with the total pressure boundary condition, where the averaged pressure is under-predicted by the simulation. Due to the more accurate mass flow rate, the constant mass flow rate boundary cases have a higher thrust than that of the total pressure boundary condition. To conclude, both of the boundary conditions capture the general trend of the detonation structure and the injection dynamics. However, one must choose the appropriate boundary condition for the inlet depending on the quantity of interest for the study, such as the plenum pressure or axial pressure distribution.

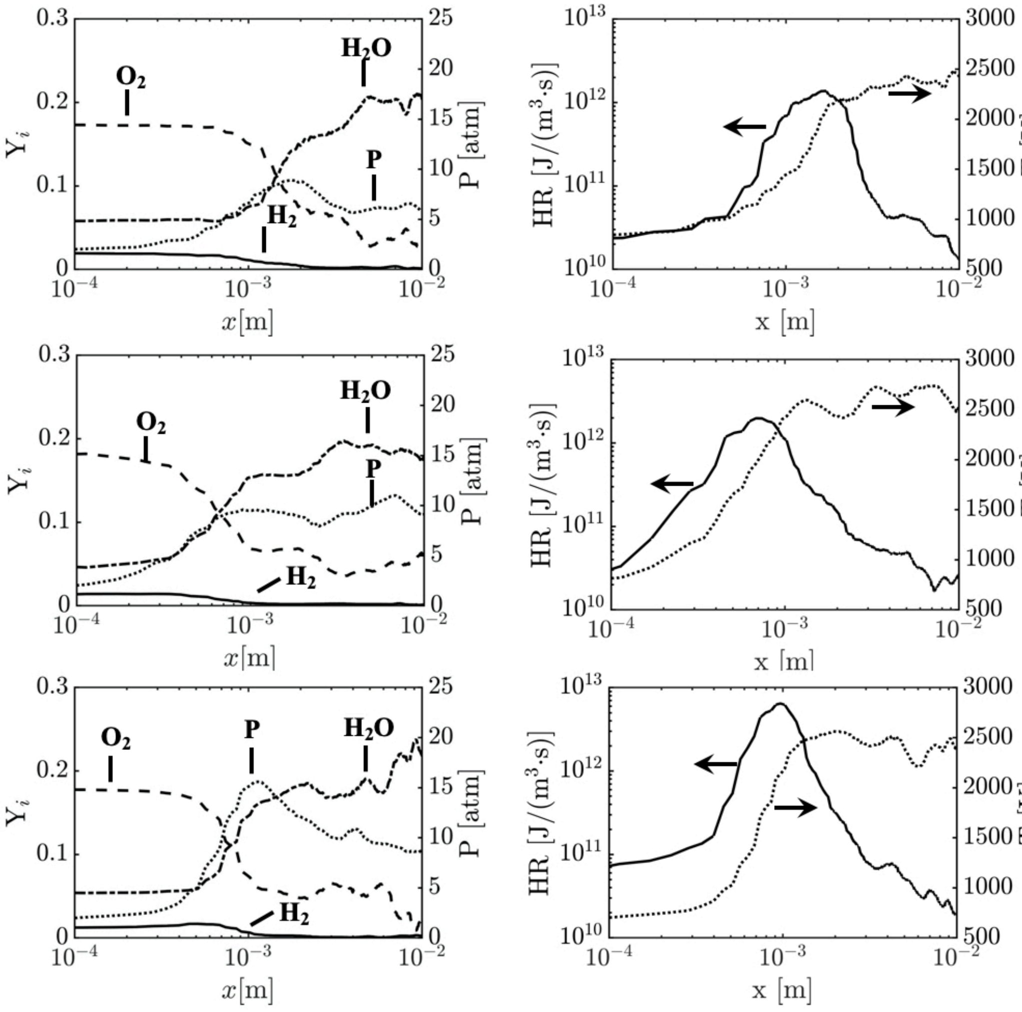

Figure 4.10: One-dimensional shock-normal averaged species and pressure profiles (left), and temperature and heat release profiles (right). x = 0 indicates shock front location. The top, middle, and bottom row correspond to cases 1, 2, and 3, respectively. The data is obtained at the mid-channel diameter 1 cm from the center of the air inlet throat.

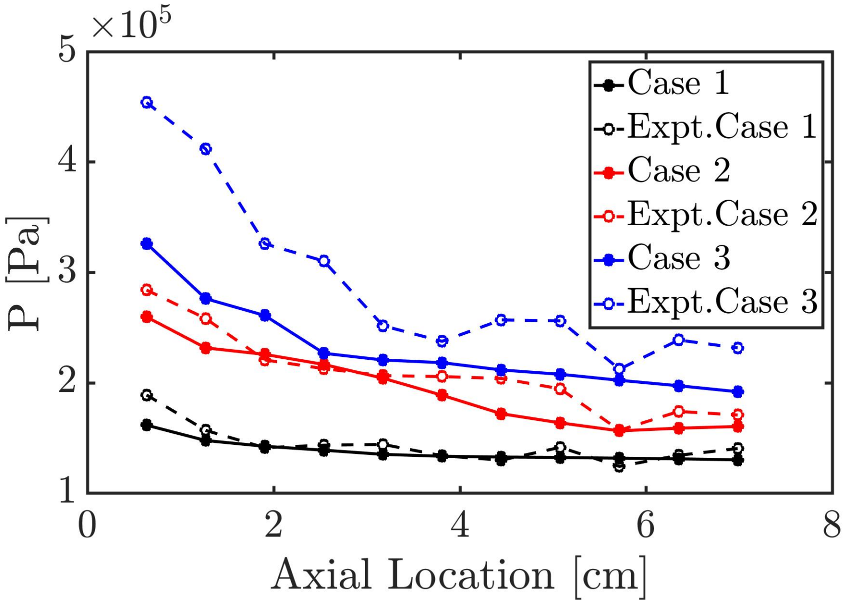

Figure 4.11: Comparison of pressure measurement on the chamber wall between simulation (total pressure boundary) and experiment.

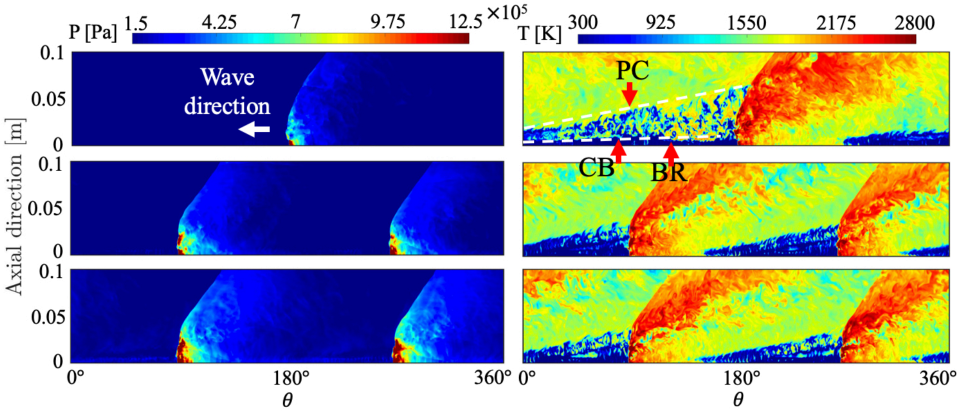

Figure 4.12: Pressure and temperature on the unwrapped plane at the mid-channel with the constant mass flow rate boundary condition. Top: case 1, middle: case 2, bottom: case 3.

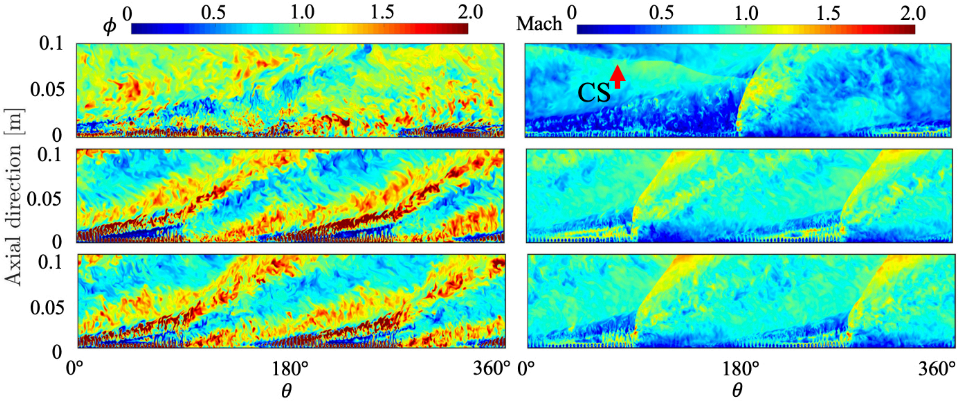

Figure 4.13: Equivalence ratio and mach number on the unwrapped plane at the mid-channel with the constant mass flow rate boundary condition. Top: case 1, middle: case 2, bottom: case 3.

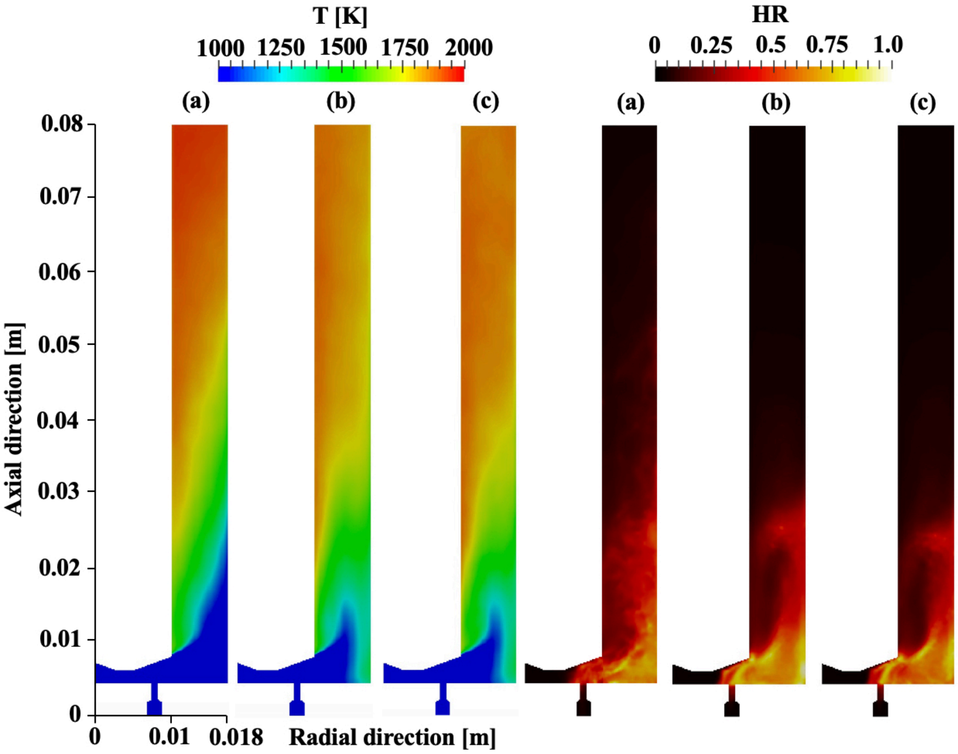

Figure 4.14: Azimuthally-averaged temperature and normalized heat release rate for (a) case 1, (b) case 2, and (c) case 3 with the constant mass flow rate boundary condition.

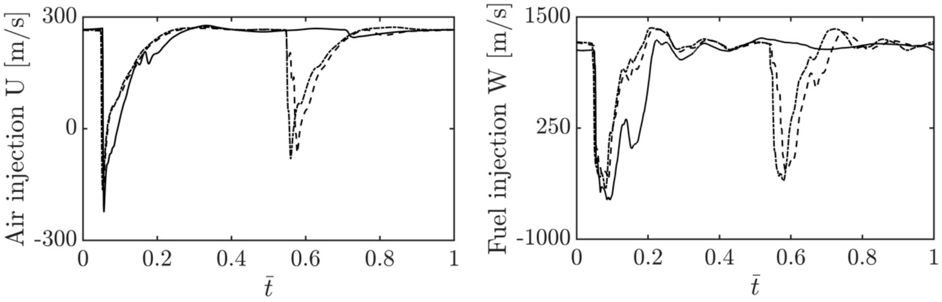

Figure 4.15: Variation in injection velocity with cycle-averaged time for oxidizer and fuel inlets with the constant mass flow boundary condition. The solid line, dashed line, and dotted line show case 1, 2, 3, respectively.

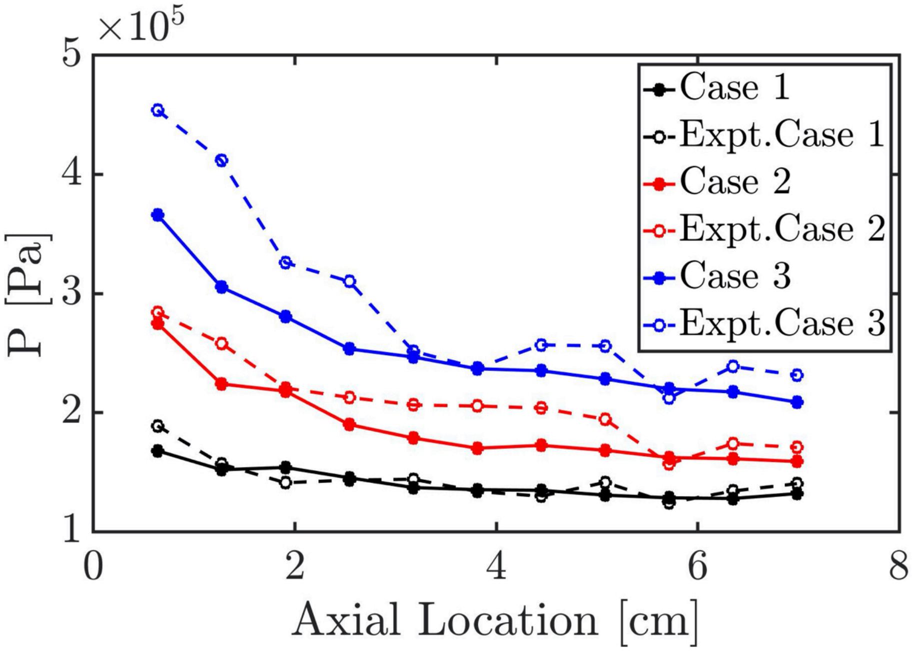

Figure 4.16: Comparison of pressure measurement on the chamber wall between experiment and the simulation with the constant mass flow boundary condition.

CHAPTER V

Simulation of UM Axial Air Inlet Configuration

5.1 Axial Air Inlet

This chapter is to numerically simulate the axial air injector based RDE in order to understand the details of the detonation structure. This configuration [6, 23] has been the object of several experimental studies that include characterization of OH chemiluminescence, OH-PLIF and pressure traces. Here, the detailed simulation approach followed by Cocks and Holley [52] is used, along with multi-step chemical kinetics for hydrogen/air combustion. In the next section, the simulation configuration and numerical details are provided, followed by a discussion of the results.

5.2 Simulation Configuration

The RDE configuration considered in this work is the axial air injection system [23], shown schematically in Fig. 5.1. Fuel is injected using $n = 120$ discrete ports positioned at an angle to the oxidizer stream. For the case simulated, the air mass flow rate is 404.2 g/s, with a global equivalence ratio of 1.01. In the experiment, the detonation chamber exhausts to a larger plenum. In the simulations, this plenum exit (outflow plane) is assumed to be at atmospheric conditions. The flow is subsonic in this region.

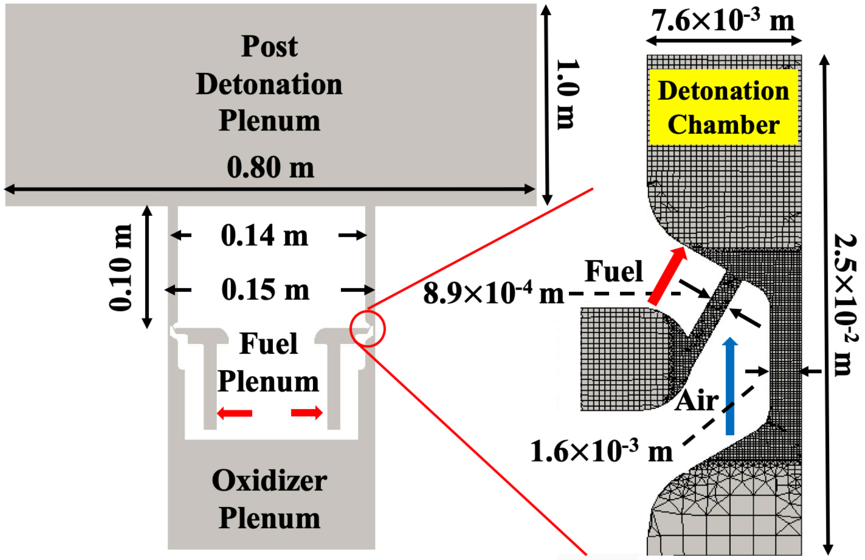

Figure 5.1: (Left) Computational geometry; (Right) Details of the fuel injector and air inlet along with computational mesh.

The simulation domain is shown in Fig. 5.1. Grid points are clustered in the near-injector region to fully resolve fuel-air mixing. The mesh size is approximately 10^{-4}m in the injector region, and 2×10^{-4}m in the region up to 0.4m in the axial direction. A total of 25×10^6 control volumes are present in the entire domain. In order to collect long term statistics needed for the analysis below, the baseline grid was used. For comparison, these resolutions are similar or finer than other full system RDE simulations [52, 79]. The results show that the detonation front is resolved by 10-20 cells in the shock-normal direction. It will also be seen that the reaction zone is distributed along the circumference, similar to prior linear model results [37].

The inflow is described using a constant mass flow rate, with the fluid properties interpolated from within the fluid domain. Adiabatic walls (zero-gradient in temperature) along with no-slip wall boundary conditions are used. The simulation is first run for 15 cycles to ensure statistical stationarity, after which data is collected for 10 cycles. The analysis is based on different types of averaging (Fig. 5.2). For these analyses, the wave front is defined by the location of maximum pressure gradient.

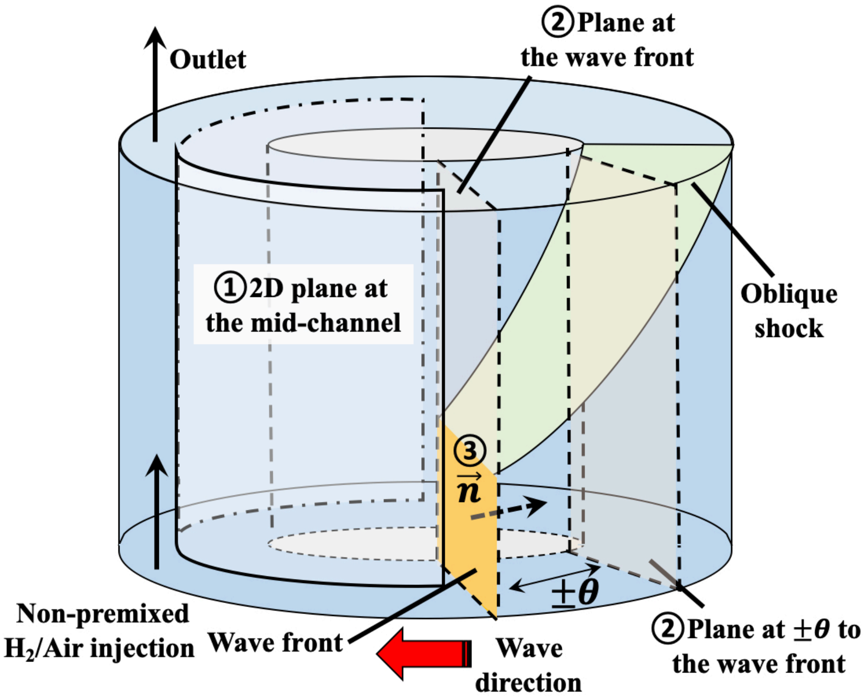

Figure 5.2: Schematic showing the averaging planes used for the analysis in this work.

5.3 Validation

5.3.1 Unwrapped field comparision between expt. and sim.

Figure 5.3 shows the mid-plane of the annulus unwrapped as a two-dimensional field (1 in Fig. 5.2); the images show LIF signal strengths scaled relative to the 98th percentile values of the respective datasets. Compared to ideal two-dimensional simulations [47], the three-dimensional discrete injection results show a much richer flow structure characterized by multiple regions where combustion occurs. The notation followed here is similar to that of Chacon et al. [6, 33]. The wavefront is highly corrugated, which is a result of the turbulence and highly non-uniform fuel-air mixture that is being processed by the wave. This leads to substantial local variations in wave velocity [37, 80], including post-detonation pressures and temperatures.

The reacting flowfield predicted by the computations is qualitatively similar to what was observed experimentally. As observed in experiments in this configuration [6, 33], the fuel-air mixture begins burning at various locations upstream of the deto-

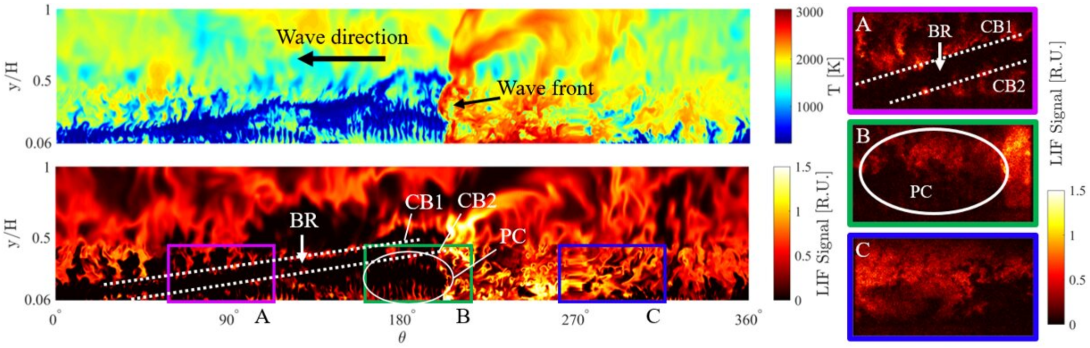

Figure 5.3: (Left) RDE temperature field and numerical synthetic OH-PLIF computed using a two-level model [9] shown as an unwrapped 2D image. Right: OH-PLIF images obtained from experiment, reproduced from [6].

nation wave, an effect that has been termed *parasitic combustion* [33]. This includes a first contact burning region (CB1) at the contact surface between unburnt and burnt gases from the previous cycle, and a second contact burning region (CB2) close to injection where the second deflagration zone is observed. This second region is likely supported by the injector design where flow recirculation around the injectors entrain burnt gases and fuel, leading to rich mixtures in a radical pool that facilitates stabilization (flameholding) of parasitic combustion.

The CB1 and CB2 regions have slightly differing slopes and are separated by a buffer region (BR). The width of the buffer region depends on the relative response time of the injectors, especially the oxidizer injector. The overall effect of these contact burning regions is to partially consume the mixture ahead of the wave through what collectively is referred to as parasitic combustion (PC) [6]. The first order effect is to weaken the detonation wave (lower speed and pressure rise) [33]. These effects are accentuated by the details of the injection process and thus emphasizes its importance.

5.4 Mixing Process with Axial Air Inlet

One of the unique features of RDEs is the time-varying injection of fuel and oxidizer. The high pressure in the post-detonation region blocks or unchokes the flow, leading to a finite recovery time. Figure 5.4 shows the average injection plane velocity for the fuel and oxidizer inlets as a function of cycle-normalized time (i.e., the time taken for the detonation wave to complete one cyle). It is seen that both injectors are nearly blocked as the detonation wave passes (at $\bar{t} \approx 0.4$), and take nearly the rest of the cycle time to reach the steady flow. Since the mass flow rate upstream is fixed, this temporary blocking of certain injectors close to the wave pressurizes the fluid in the plenum, and redirects the flow towards unblocked injectors. The fuel injector is generally more stiff, and relaxes to the full flow faster compared to the oxidizer. This in turns creates local variations in equivalence ratio as a function of cycle time.

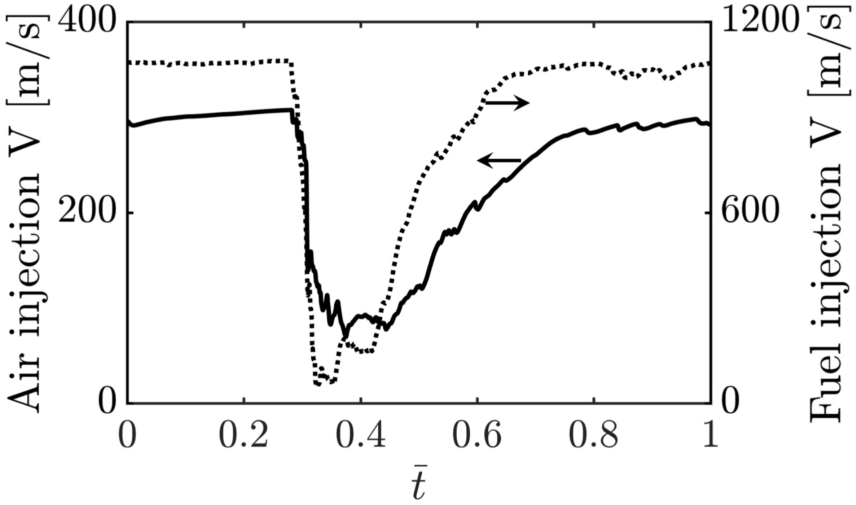

Figure 5.4: Variation in injection velocity with cycle-averaged time for oxidizer and fuel inlets.

The fuel distribution is analyzed in Fig. 5.5, which shows the phase-averaged mixture fraction distribution in the domain. For this purpose, the detonation wave was defined as the location of maximum pressure gradient along a plane aligned with the axial direction. Then, data slices at angular increments of 15° were averaged to obtain the phase-averaged data (2 in Fig. 5.2). Since the fuel ports are discrete, the wave might be located at several instances in between injectors. It is seen that 15° ahead of the wave, the fuel jet is well-developed, and penetrates far downstream. The equivalence ratio in the core of the jet is roughly 5. It is also seen that pockets of rich mixture exist further downstream, roughly at the height where the PC region is found. At the wave front, the sudden pressure rise reduces jet penetration. Further, 30° degrees behind the wave, the jet length remains short, which is consistent with the recovery times seen in Fig. 5.4. In spite of these variations, the peak mixture fraction drops from 1 to roughly 0.1 quickly shows fast but incomplete mixing.

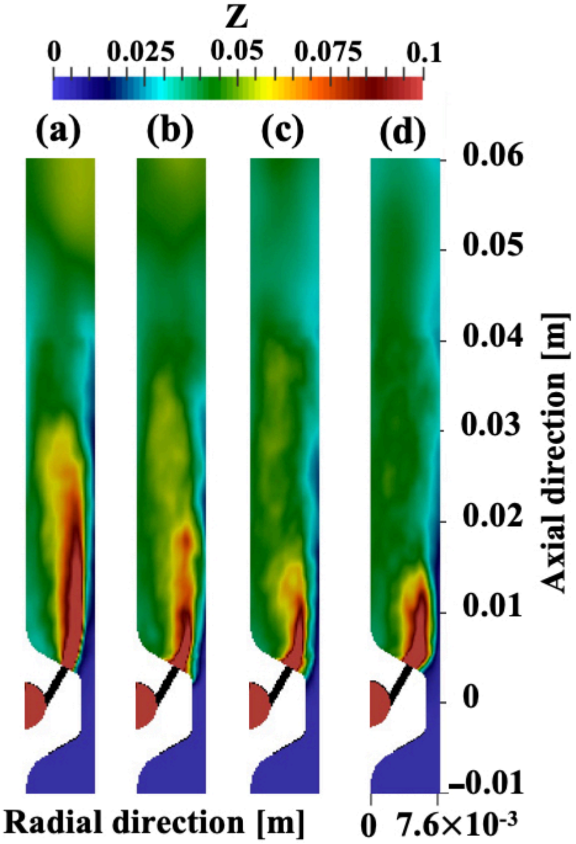

Figure 5.5: Phase-averaged mixture fraction plotted at a) 15° ahead the wave front, b) the wave front, c) 15° behind the wave front, d) 30° behind the wave front.

5.4.1 Wave structure

Figure 5.6 shows the pressure and temperature averaged at the wave front over the entire simulation time (2 in Fig. 5.2). The temperature field shows considerable asymmetry, with peak temperatures found close to the inner wall. As described earlier, the deflagration below CB2 is caused by recirculation of the fuel-air mixture in this region between the fuel jets and the inner wall. This causes sustained high temperature in this region, which is further increased by the passing detonation wave through compression. The pressure field shows much more symmetry except for a small region of high pressure near the outer wall. This result seems counter-intuitive given the fuel distribution shown in Fig. 5.5. The peak pressure in the simulations is substantially lower than the ideal detonation cases. This is indicative not only of the losses due to parasitic combustion, but also the large variations in the detonation structure with time. This inhomogeneity is a result of temporal variations in the shock front, including its sensitivity to the fuel-air stratification and parasitic combustion. As a result, this homogeneity is feasible on an average, but considerable instantaneous fluctuations about the mean exist.

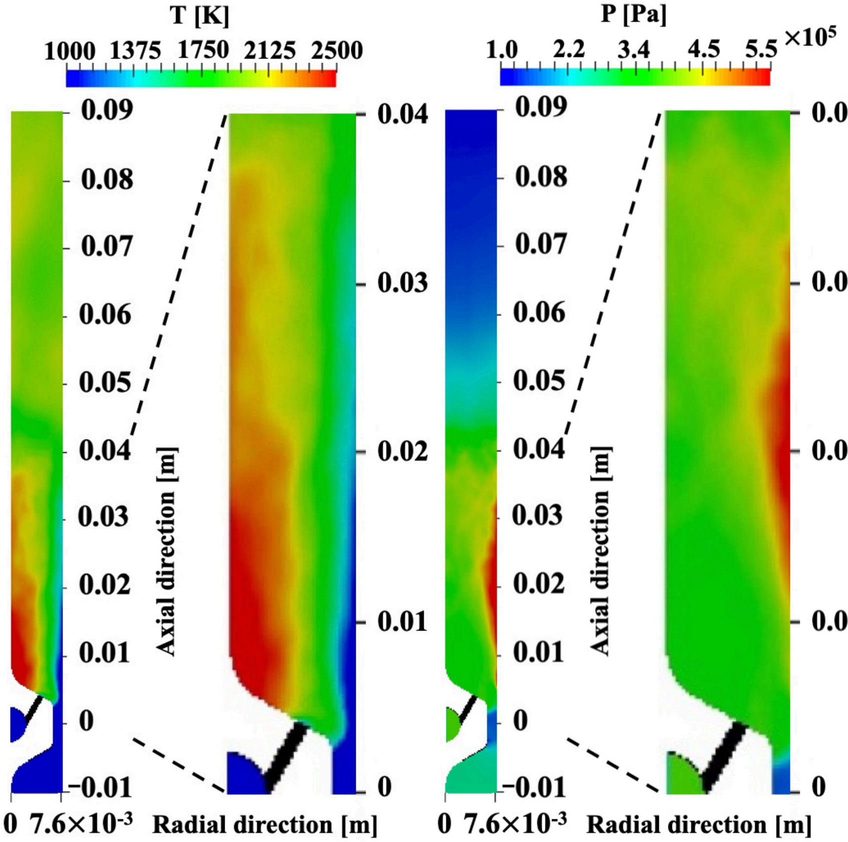

Figure 5.6: Phase-averaged (left) temperature and (right) pressure field at the detonation front.

5.5 Statistical Analysis for Detonation Structure

5.5.0.1 1D profiles across the wave front

In order to understand the overall structure in composition space, unconditional time averages at steady-state conditions are presented. Figure 5.7 shows comparison of experimental data with simulation results for the axial variation of normalized pressure, where the normalization factor is the plenum pressure. It is seen that the simulations predict the decay in pressure across the plenum throat and in the near-field of the injection plane. The simulations predict a stronger detonation wave, which is also reflected in the faster wave speed of 1804 m/s as compared to 1566 m/s in the experiments. But overall, the continued drop in pressure beyond the detonation region is also captured in the simulations.

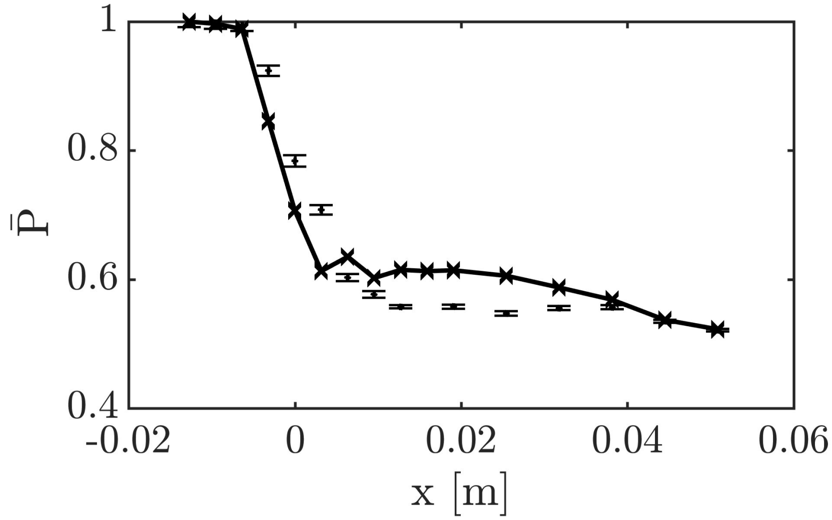

Figure 5.7: Comparison of pressure measurement on the chamber wall with time-averaged simulation data. The simulation and the experiment pressures are normalized by 254 kPa and 296 kPa, respectively. The circle symbol denotes the experimental data and the cross symbol with line denotes the simulation results.

Figures 5.8 and 5.9 show one-dimensional profiles across the shock (based on 3 in Fig. 5.2). At the detonation front, H_2O mass fraction is already high, indicating residual gases from the previous cycle are present in the mixture. It is also seen that the pressure profile shows an inflection point around 4×10^{-4}m, which corresponds to the start of the oxidation process. Hence, the region of gradual O_2 consumption can be considered as the induction zone. The reactions occur over an appreciable length. This further indicates that the fluid reaches chemical equilibrium over timescales comparable to the induction time and is not a jump process. The temperature profile shows a more gradual increase due to the distributed heat release caused by the parasitic combustion and the extended reaction zone behind the shock front. The heat release plot shows that the presence of burnt gases causes sustained heat release behind the shock wave, but the peak exothermicity is reached when fresh gases react past the induction zone.

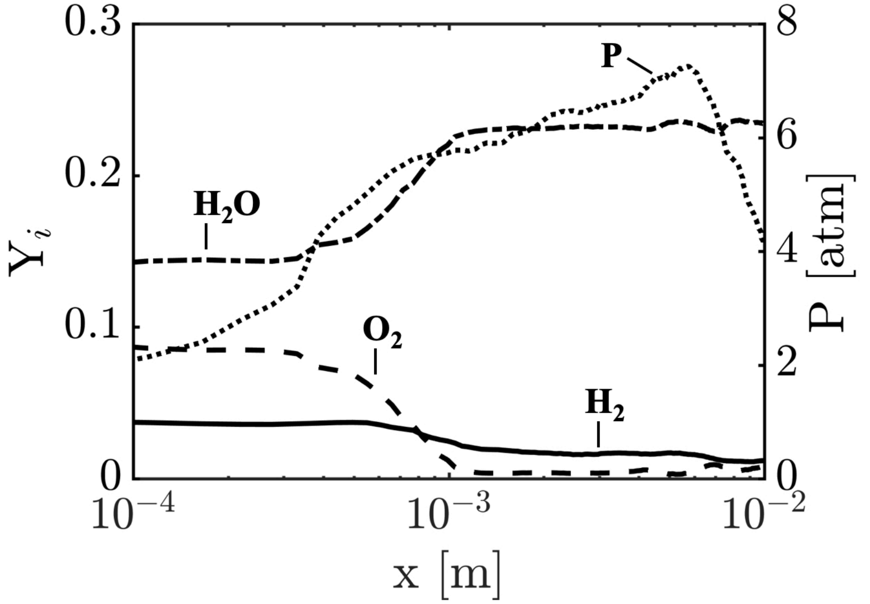

Figure 5.8: One-dimensional shock-normal averaged species and pressure profile. $x = 0$ indicates shock location. The data is obtained at mid-channel 2 cm from the center of the air inlet throat.

5.5.1 Conditional average profile

Conditional averages of key quantities such as temperature and species mass fractions conditioned on mixture-fraction provide insight into the reaction structure of

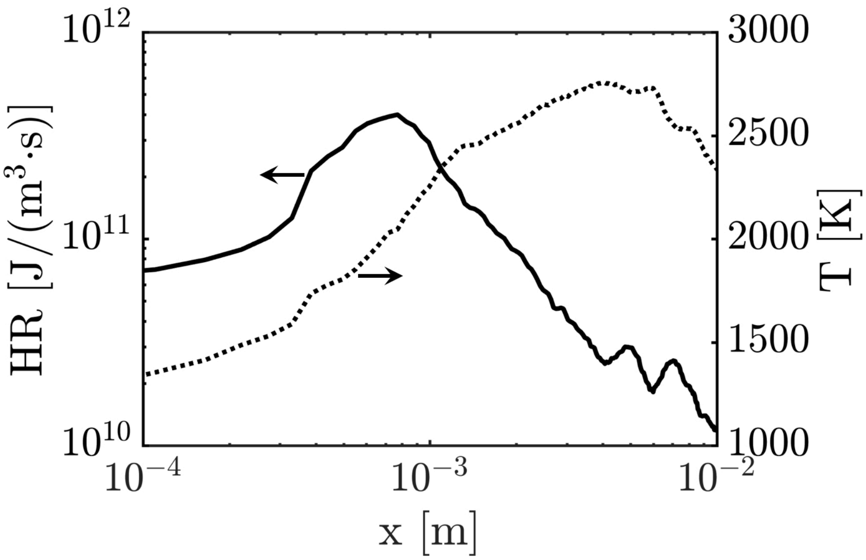

Figure 5.9: One-dimensional shock-normal averaged heat release rate and temperature profile. $x = 0$ indicates shock location. The data is obtained at the mid-channel 2 cm from the center of the air inlet throat.

flames. Figure 5.10 shows the conditional average of temperature at three different locations (at the wave, ±12.5° from the wave) (2 in Fig. 5.2). The averages are obtained over the entire plane shown in Fig. 5.6. It is seen that ahead of the wave, there is already significant heat release leading to a higher temperature than the plenum value of 300 K. The near-stoichiometric value is slightly higher than 1000K, which is higher than the temperature needed for chain branching reactions to be dominant for hydrogen-air chemistry. As a result, the mixture that is being processed by the wave is highly reactive and the conditional averages at and behind the wave are nearly the same. It should be noted that the peak in temperature is at slightly richer mixture fraction values than stoichiometric, which is consistent with the observation that the highest detonation velocities occur for richer mixtures. Figure 5.11 shows the conditional species profiles for the reactants. It is seen that at the wave and behind the wave, there is non-zero oxygen concentration on the rich side, indicating some leakage due to inefficiencies in the mixing process. Ahead of the wave, there is already significant consumption of the fuel and oxidizer, leading to the higher temperatures in the CB1/CB2 region.

Figure 5.12 shows the conditional heat release average. Overall, heat release rates do not show the same structure as the other species profiles discussed above. Instead, much of the heat release is on the lean side, and is significantly higher at the detonation front compared to either ahead or behind the wave. Note that the one-dimensional shock profile shown in Fig. 5.9 covers roughly 2° in azumithal angle. This is an indication that although the reaction structure is quite distributed, the non-ideal detonation wave could be compared to a thickened flame front. Heat release after the wave is confined to a narrow region but it is much more spatially distributed before the wave. This feature has been observed in linear detonation models as well [37, 71].

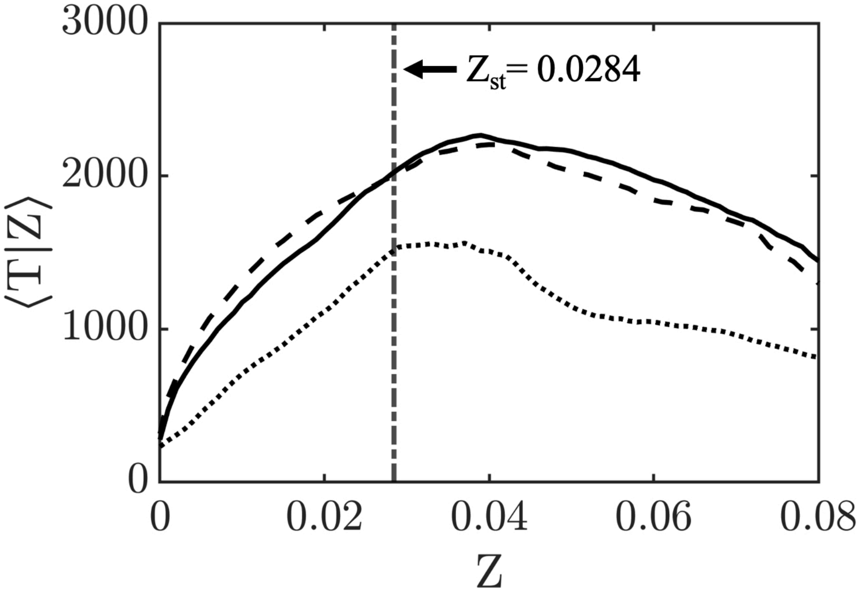

Figure 5.10: Conditional temperature (K) averaged conditioned on mixture fraction. The solid line, dashed line, and dotted line show the wave front, 12.5° behind of the wave front, and 12.5° ahead of the wave front, respectively.

Figures 5.13 show the conditional fluctuations of temperature. First, it is seen that the conditional deviation is quite high, often comparable to the mean values themselves. This indicates strong bi-modal behavior, with intermittent regions of high products and reactants at all locations. The conditional variance of reactants reveals that the near-stoichiometric region has lower fluctuations compared to the

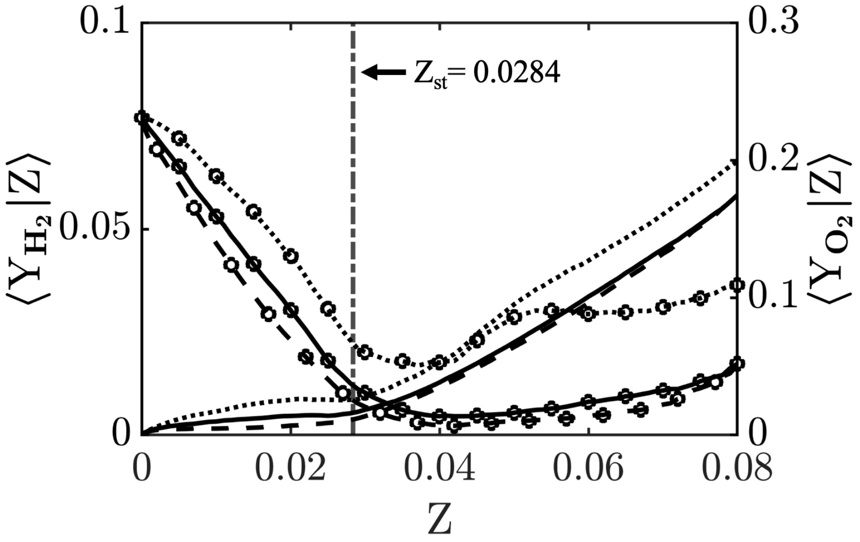

Figure 5.11: Conditionally average species mass fraction conditioned on mixture fraction. The solid line, dashed line, and dotted line show the wave front, 12.5° behind of the wave front, and 12.5° ahead of the wave front, respectively. (Line without markers:$\langle Y_{H_2}|Z\rangle$, line with markers:$\langle Y_{O_2}|Z\rangle$)

region of high heat release on the lean side. Moreover, there is considerable variation at rich conditions, where there is still significant fuel left after the detonation wave. These regions correspond to downstream locations ($>$ 0.03m in Fig. 5.5).

5.6 Mass Flow Rate Effect with an Axial Air Inlet

From this section, two other flow rates - 300 and 700 g/s - will be used to understand the role of mixing on detonation modification. In the experiments, the 700 g/s case exhibited two detonation waves, but this flow condition was reached in the experiments through an unconventional strategy (explained in Sec. 5.8.1). In the simulations, it will be shown that both cases show only a single wave, but the wave structure is modified completely. It will be demonstrated that shear-induced mixing strengthens the wave, leading to propagation that explains the trends observed in the prior studies described above.

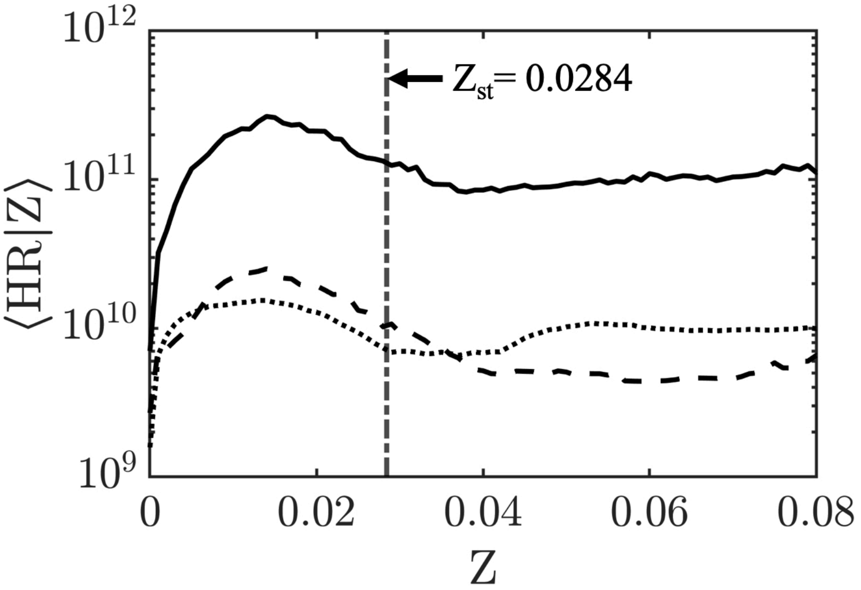

Figure 5.12: Conditionally average heat release (J/(m^3·s)) conditioned on mixture fraction. The solid line, dashed line, and dotted line show the wave front, 12.5° behind of the wave front, and 12.5° ahead of the wave front, respectively.

5.7 Simulation Configuration, Experimental Configuration, and Computational Details

The experimental setup used in the study is the same as was presented by Chacon et al. [23]. The RDC test facility is composed of a modular 154 mm outer diameter RDC, air and fuel supply systems, an enclosed exhaust system, and data acquisition and control systems. For this study hydrogen/air operation is considered.

The RDC used in the study is modular and can house different air and fuel handling configurations (Fig. 5.14). However, in this study we consider only the axial air inlet configuration that has been extensively studied in previous work [6, 23, 33]. This configuration is characterized by an axial air inlet where air flows axially over a smooth symmetric, one-sided contoured surface extending from the central body of the RDC. Fuel is injected from the rear of the contour through 120 discrete evenly spaced injection portholes of diameter 0.89 mm arranged around the circumference

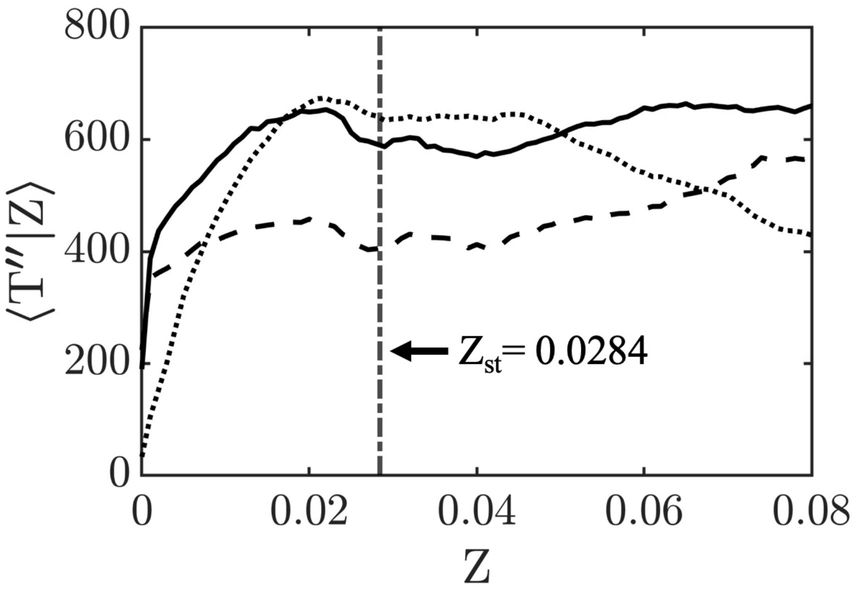

Figure 5.13: Conditional standard deviation of temperature (K) conditioned on mixture fraction. The solid line, dashed line, and dotted line show the wave front, 12.5° behind of the wave front, and 12.5° ahead of the wave front, respectively.

of the contour. The air throat gap is 1.52 mm, providing a throat-to-channel area ratio of $A_t/A_c = 0.2$. The RDC has an outer detonation channel diameter of 154 mm and inner channel diameter of 138.8 mm resulting in a channel gap width of 7.6 mm. The length of the channel, defined as the distance between the axial mid-plane of the air inlet throat and the exit plane, is 104 mm. Past the air inlet constriction, the detonation channel has a constant cross section and directly discharges into an exhaust plenum connected to the exhaust system without any exit constriction.

The main challenge in simulating practical RDC configurations is the complex flow path, combined with the multiscale physics introduced by turbulence interacting with shock waves and chemical reactions. As a result, computational simulations over a large range of operational conditions or for long physical times are prohibitively expensive. Recently, Sato et al. [75] have demonstrated a robust computational solver for modeling such complex RDCs. In order to capture some behaviors of interest, two operating conditions were studied computationally, having mass flow rates of

$\dot{m} = \{300, 700\}$ g/s (see Tab. 5.1). Companion experiments for this study were instead swept across a range of mass flow rates at nearly constant equivalence ratio for extended durations so as to capture a greater range of information than through single operational point tests. This approach has the benefit of being very time efficient compared to individual experimental runs. However it does pose the question of how significant the ramping effect is on the properties of the detonation wave we are trying to investigate. Here we consider the transient taken (approximately 3.5 seconds) to be of a sufficiently long timescale compared to the detonation cycle time (approximately 300 microseconds) such that it had minimal impact on detonation velocity and correspondingly fast processes/measurements. In the experiment discussed here, operation of the device was initiated at an air mass flow rate of approximately 200 g/s of air at an equivalence ratio of 0.6. Following a half second stabilization, the fuel and air flow rates were transitioned over a 3.5 second transient to a final operational condition of approximately 1,000 g/s of air with an equivalence ratio of approximately 0.8. Figure 5.17 shows the mass flow rate and equivalence ratio trajectory taken as a function of time.

This particular $(\dot{m}, \phi)$ trajectory was designed to minimize the variation of equivalence ratio ϕ for the majority of the mass flow rate sweep. In particular, between a mass flow rates of 400 and 1,000 g/s the equivalence ratio remains approximately constant. The relatively small variation in equivalence ratio makes this case a good approach to investigate how the wave speed varies with mass flow rate and the wave splitting process.

The two experimental runs (cases 1 and 3 in Tab. 5.1) operate at different equivalence ratios. In order to ensure that the effect of the equivalence ratio is taken into account, a third simulation (case 2) at an equivalence ratio of 0.75, which is equal to that of the higher mass flow rate case, is also conducted.

The simulations are carried out at constant mass flow rates. As a result, there are

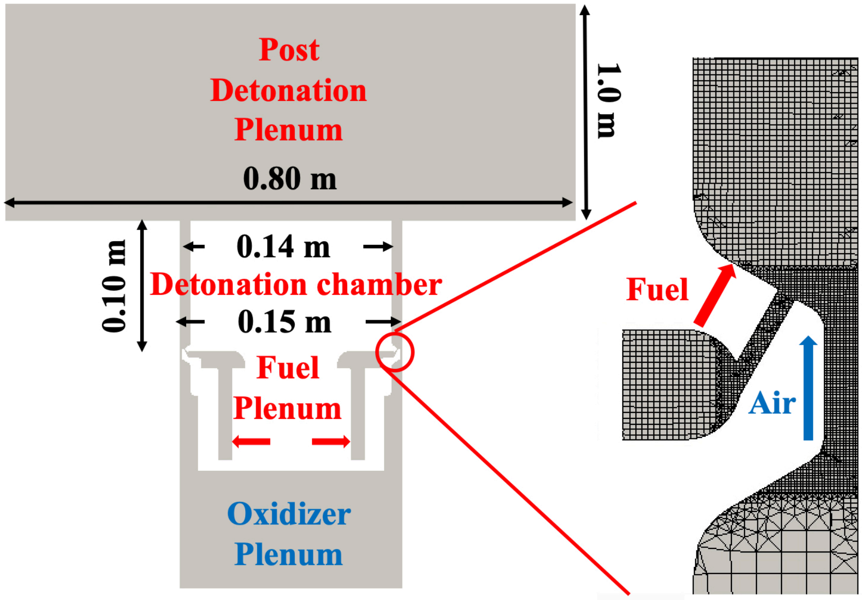

Figure 5.14: Schematic of the simulated the geometry with the detailed grids structure around the discrete fuel injector and the air inlet.

	$\dot{m}_{air}$ [g/s]	ϕ	P^{air}_{plenum} (cold flow) [kPa]	P^{fuel}_{plenum} (cold flow) [kPa]	Fuel injection holes [m]	Air inlet slot [m]	$\bar{P}^{2.54cm}_{Expt.}$ [kPa]	$\bar{P}^{2.54cm}_{Sim.}$ [kPa]	$\frac{D_{Expt.}}{D_{CJ}}$	$\frac{D_{Sim.}}{D_{CJ}}$
Case1	300.88	1.02	187	246	8.9×10^{-4}	1.6×10^{-3}	137	130	0.8	0.9
Case2	300.88	0.75	187	200	8.9×10^{-4}	1.6×10^{-3}	–	124	–	0.87
Case3	700.36	0.75	388	434	8.9×10^{-4}	1.6×10^{-3}	–	226	0.7	0.92

Table 5.1: Details of the test cases as well as the key injector/inlet dimensions.

operational differences from the experimental runs. In this study, governing equations for fluid flow including viscous terms, species transport with diffusion terms, and the energy equation are solved.

The simulations are carried out as follows. First, the jets are developed for 0.4 ms but no chemical reactions are computed. After the jet development process, a one-dimensional detonation profile is patched with a height of 1 cm in the detonation chamber to initiate a detonation wave. To ensure that the flow-field reaches steady state, the computations are run for at least 20 detonation cycles. The data for analysis, which will be discussed from the next section, are collected for 10 cycles after reaching a steady state, which results in at least 30 cycles for each case. All simulations are run on 4000 cores using MPI-based domain decomposition.

5.8 Results and Discussion

5.8.1 Observations from experiments

By monitoring the flow rates through the air and fuel supply lines and by using the high-speed pressure measurements, we are able to correlate the mass flow rate through the RDC with the detonation wave speed and observe the wave splitting process. The relationship between the mass flow rate and wave speed is shown in Fig. 5.15. Between 200 and 400 g/s, both the mass flow rate and equivalence ratio vary significantly (see Fig. 5.16), while from 400 g/s to the end of the transient, the equivalence ratio remains nearly constant at 0.75. Initially the RDC operates in a single detonation wave mode, and the wave speed increases as both $\dot{m}$ and ϕ are increased. The wave speed continues to increase even once the constant equivalence ratio portion is reached, and then the wave splits at about 500 g/s, and the wave speed suddenly drops (from about 1.6 km/s to just over 1.3 km/s). By increasing the mass flow rate further the wave speed increases back up until the system transitions to a three wave operation mode at about 900 g/s. In this mode the wave speed reduces further to about 1.25 km/s. Although the mass flow rate slowly increases in the latter portion of the transient (from 3 to 5 seconds), the wave speed remains nearly constant at about 1.25 km/s for the remainder of the transient. The evolution of the wave system through the transient, including the presence of secondary waves, can also be seen from the waterfall spectrum shown in Fig. 5.17 computed from the high-speed pressure measurement taken at the combustor outer wall at an axial location of $z/H = 0.3$. The behavior observed in this transient run is similar to observations made by Bykovskii et al. [16], where after every wave splitting event, the speed of the wave decreased.

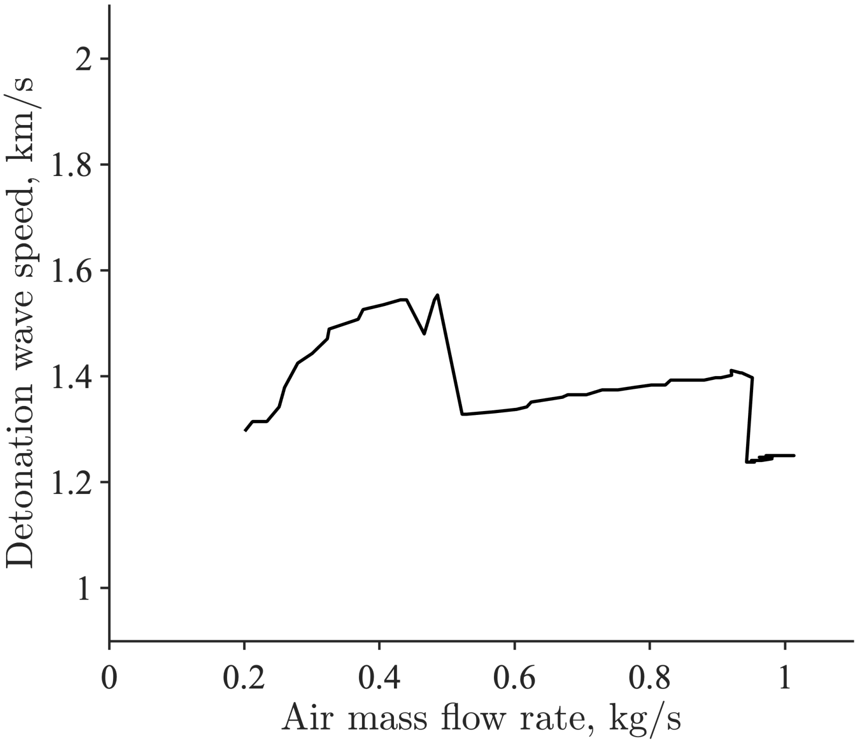

Figure 5.15: Detonation wave speed as a function of mass flow rate during the transient operation. Sudden change in speed indicates transition from 1 to 2 and from 2 to 3 waves.

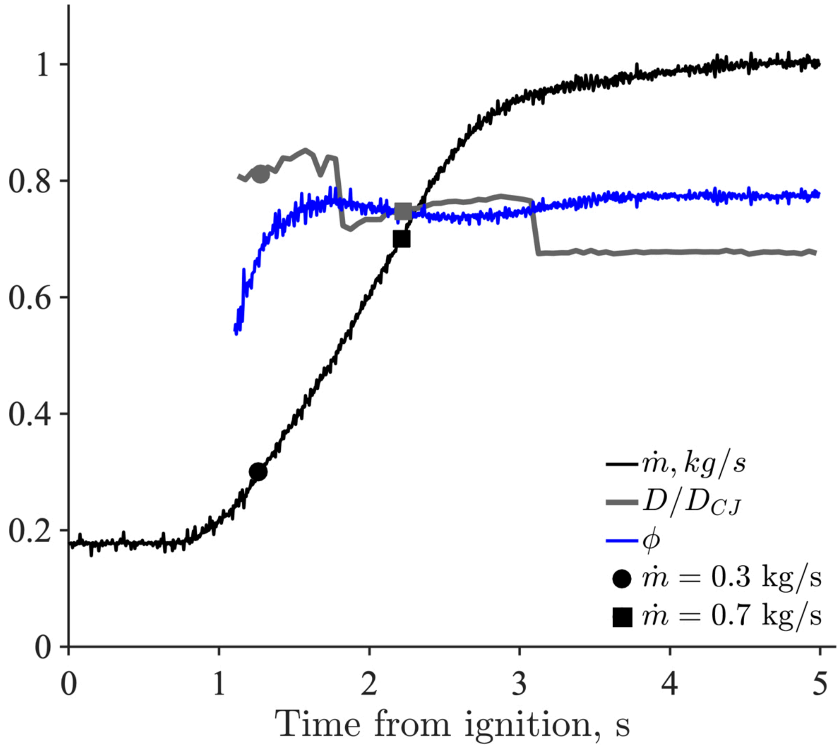

Figure 5.16: Time-history of air mass flow rate, equivalence ratio and wave speed across the duration of the full transient operation.

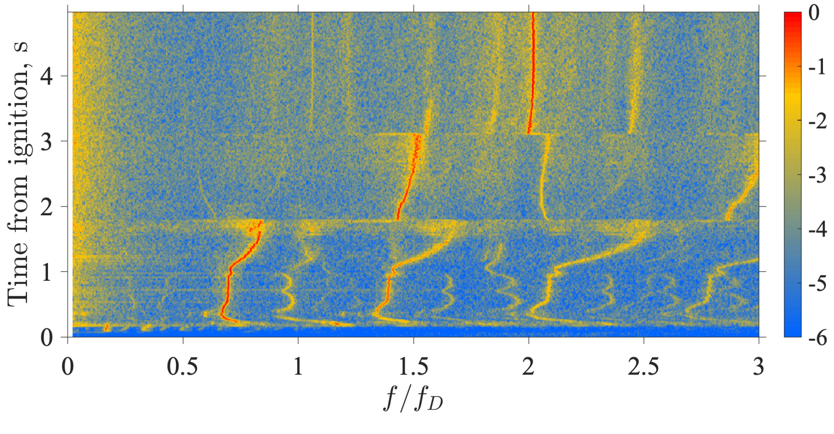

Figure 5.17: Waterfall spectrum from high-speed pressure measurement at $z/H = 0.3$ during the transient operation shown in Fig. 5.16.

5.8.2 Instantaneous flow structure

Figures 5.18 – 5.20 show the instantaneous pressure and temperature profiles for the three cases. In all simulations, a single detonation wave is found to propagate azimuthally in a clockwise direction without any change in the direction of motion. From the side view, it can be seen that the detonation wave is taller for the higher mass flow rate case, as expected due to the increased fill height. Moreover, the shock appears stronger but is also thicker in the shock-normal direction. For the $\dot{m} = 300$ g/s cases (1 & 2 in Tab. 5.1), the variation in equivalence ratio does not affect the detonation height significantly, suggesting that the detonation height is decided by the fill height, with the wave velocity sufficiently low to allow this fill height to be reached. The top view shows that, at least at this instant, the shock wave is stronger near the outer wall compared to the inner wall. In the $\dot{m} = 300$ g/s cases, the temperature profile is roughly homogeneous across the radial direction for $\phi = 1$, while there is strong variation present for $\phi = 0.75$. Similar radial variation can be also seen in the $\dot{m} = 700$ g/s case. Near the outer wall (shown in Fig. 5.20), striations in temperature are seen behind the shock wave, which result from the discrete air injectors.

To further understand the wave structure, an unwrapped slice of the three-dimensional flow is shown in Figs. 5.21 – 5.22 for cases 1 & 3 (case 2 shows similar structure to case 1 and is not discussed here). These plots are extracted along the middle of the channel, and show significant differences. Before discussing the variations, the flow structure is first characterized for the low mass flow case. The flow field prior to the detonation can be divided into three approximate zones: post-detonation products (from the previous cycle), a buffer region (BR) composed of nominally pure fuel or oxidizer depending on the injection response of the two reactant streams, and the fresh fill region. At the boundary between the products and the buffer region, it is possible to stabilize a contact burn (CB1), a localized flame supported by hot products and fresh reactant in the buffer region. Similarly it is possible to stabilize a

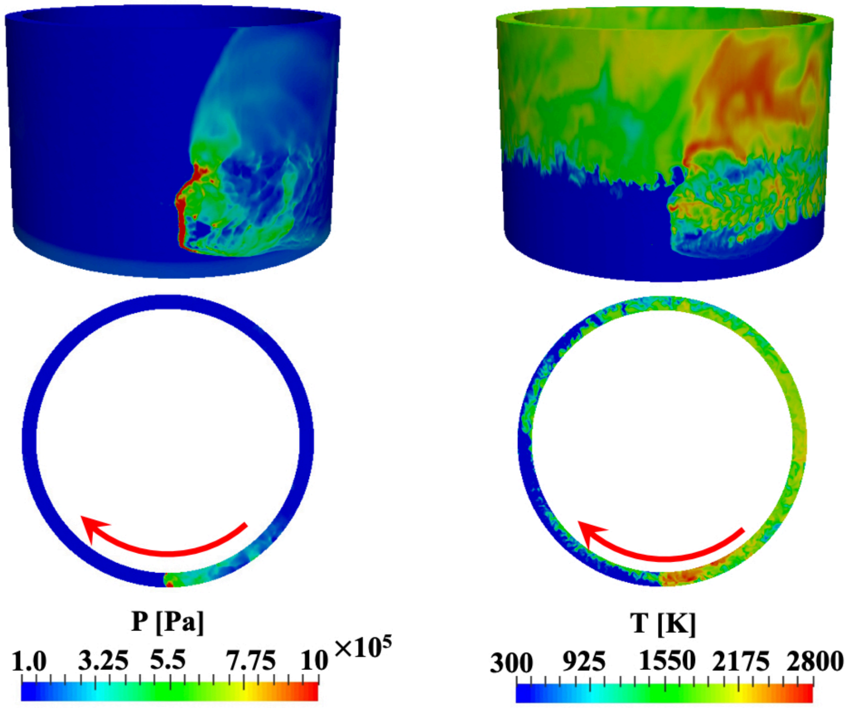

Figure 5.18: 3D view and the top view on the axial cutting plane of pressure and temperature for $\dot{m} = 300$ g/s at $\phi = 1.0$.

contact burn between the buffer region and the fresh fill region (CB2). Lastly it is possible to see in temperature contours that there are significant regions in the fill region that are at elevated temperatures suggesting reaction and a phenomena termed parasitic combustion [33]. Currently we draw distinctions between these zones and features because the supporting mechanisms are not entirely known, may be different, and to some degree independent of one another, as evidenced by CB2 being more intermittent in Fig. 5.21 while being more continuous in Fig. 5.22. In prior two-dimensional numerical studies, contact burning has been identified as a possible source of inefficiency [42, 81] as it is an inherently deflagrative process. However, in most simulations, the detonation wave proceeds at nearly the ideal velocity, indicating that any deflagration in this region does not cause loss of detonation efficiency. However, in this three-dimensional study, deflagrative processes are widespread as evidenced by the increased temperature throughout the fill region. These regions of

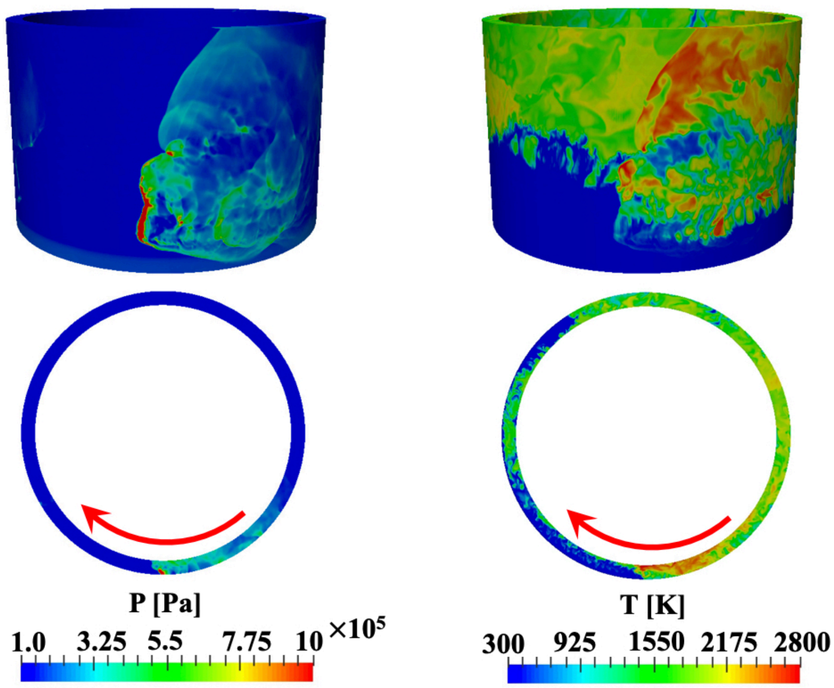

Figure 5.19: 3D view and the top view on the axial cutting plane of pressure and temperature for $\dot{m} = 300$ g/s at $\phi = 0.75$.

parasitic combustion are likely formed primarily due to the nature of the injector used, and the extended recirculation zone generated by the interaction of the fuel and oxidizer jets. Meanwhile, the buffer region is created by the different recovery time scales of the air and fuel injectors. Because the fuel injector is nominally stiffer in this configuration, it recovers faster than the oxidizer injector. The detailed discussion for the injector dynamics can be found in Sec. 5.8.3. This unsteady injection process creates regions that contain fuel-air mixtures that are too rich to burn. As a result, the buffer region is marked by high equivalence ratios and low temperatures.

Based on our definitions above, the two mass flow rate cases show differences in the structure of the three pre-detonation zones. In particular, the $\dot{m} = 300$ g/s case shows a parabolic shape, with the low temperature region showing lower penetration immediately ahead of the detonation front compared to distances farther away. This indicates that contact burning has led to significant deflagrative heat release, which

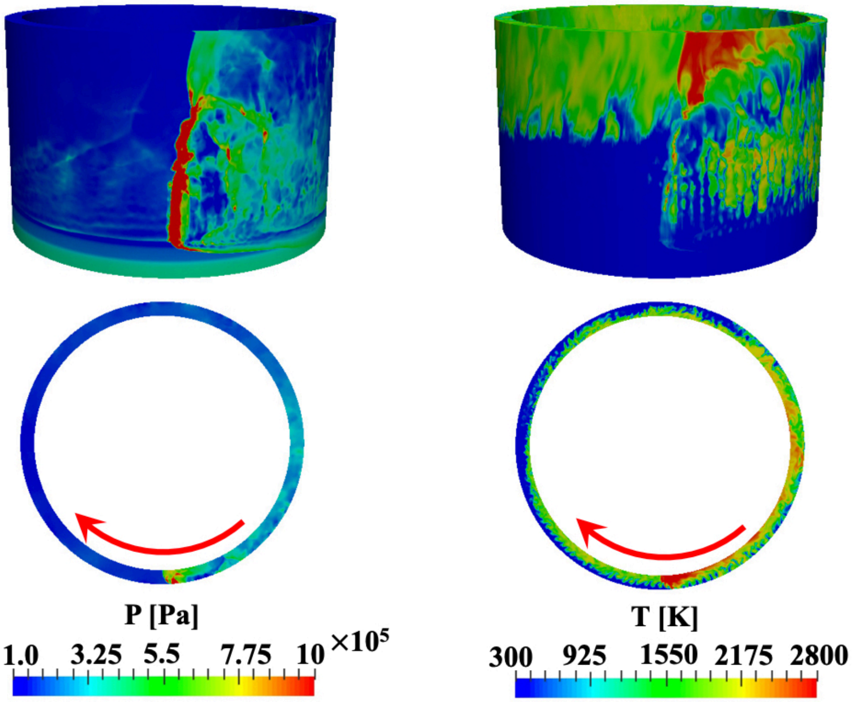

Figure 5.20: 3D view and the top view on the axial cutting plane of pressure and temperature for $\dot{m} = 700$ g/s at $\phi = 0.75$.

increases local temperature, but reduces the fuel available for detonative combustion. Due to the lower fill velocity, CB1 and CB2 are located at distances closer to the base of the channel compared to the $\dot{m} = 700$ g/s case. In the $\dot{m} = 700$ g/s case, BR is nearly a straight line, intersecting the detonation front at its full height. This structure is similar to the two-dimensional structure of RDCs [42, 47]. However, the parasitic combustion region shows increased penetration and higher temperature, indicating higher thermal losses. As a result, the detonation waves are, in some sense, the extreme cases studied by Hayashi et al. [82], with the lower mass flow rate case showing higher deflagrative combustion as compared to the higher mass flow rate case.

Further, consistent with prior studies [16], there is an increase in detonation velocity from 1715 m/s (for $\dot{m} = 300$ g/s) to 1817 m/s (for $\dot{m} = 700$ g/s) for $\phi = 0.75$ as mass flow rate is increased. For the richer condition at $\phi = 1.0$ (case 1), the

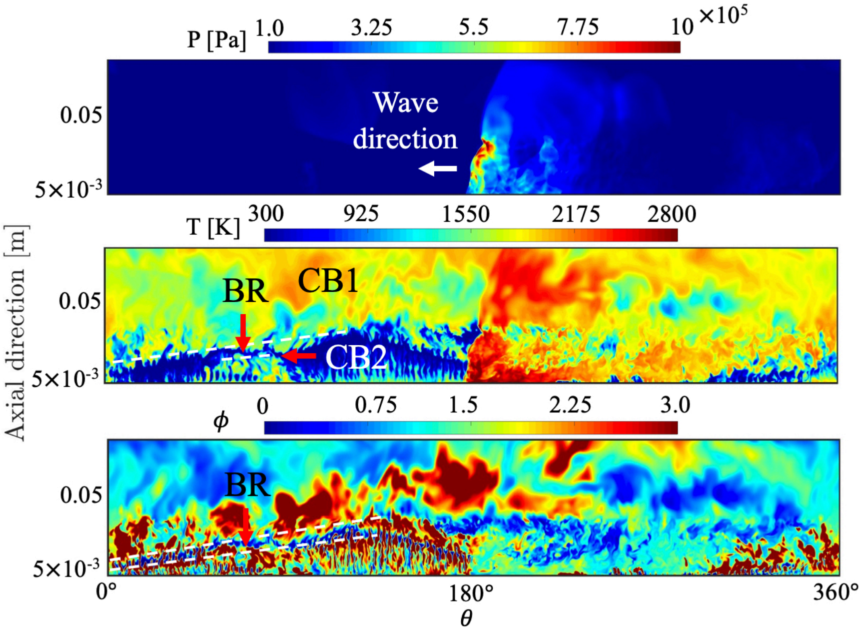

Figure 5.21: Pressure, temperature, and the equivalence ratio on the unwrapped plane at the mid-channel for $\dot{m} = 300$ g/s at $\phi = 1.0$.

wave speed is computed as 1786 m/s, which is higher than $\phi = 0.75$ case. The ratios between the measured wave velocity and the C-J speed are shown in Table 5.1. The simulations overpredict the wave speed by nearly 15% compared to the experimental value. Note that such discrepancies between experiments and simulations have been noted elsewhere as well [52, 83]. One of the possible reasons for this difference is that the experiment run time is over a few seconds, but the simulations are computed for around 10 ms only due to the severe computational cost. Due to this run time difference, the system may not have reached a thermal steady state in the simulations. However, this aspect needs to be explored further.

From the simulations, it is seen that this increase in speed and the averaged pressure in the chamber are also associated with a reduction of parasitic combustion (a known loss mechanism), but significant regions still persist. As a result, for every case, the detonation speed is much lower than ideal C-J speed. However, the wave speed is faster for the $\dot{m} = 700$ g/s case despite the increase in parasitic combustion at the mid-channel as shown in Fig. 5.22. This is because the detonation wave

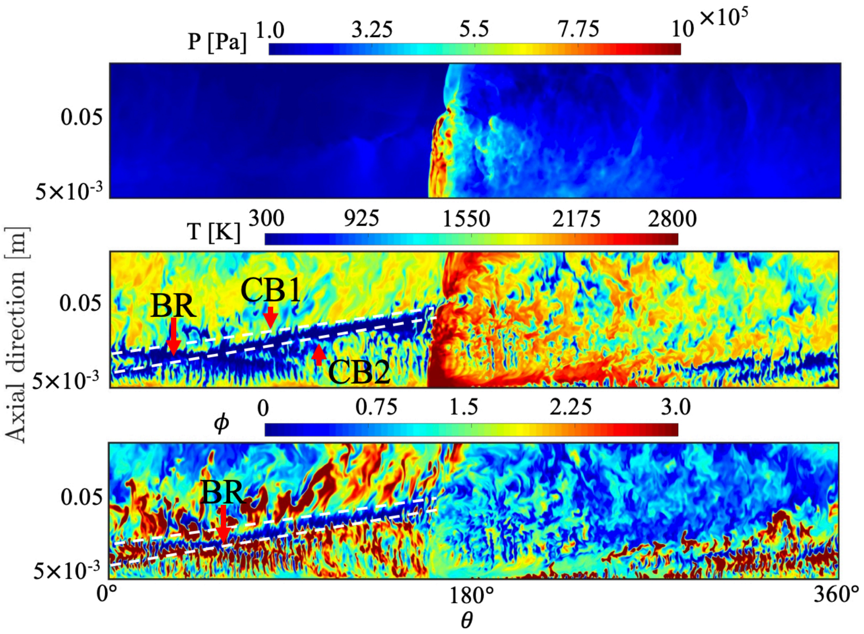

Figure 5.22: Pressure, temperature, and the equivalence ratio on the unwrapped plane at the mid-channel for $\dot{m} = 700$ g/s at $\phi = 0.75$.

propagates near the outer wall, where the mixing is less affected by parasitic combustion [75]. This detail will be discussed in Sec. 5.8.3. From these cases, it is seen that the progress towards wave-splitting is accompanied by an increase in detonation efficiency, possibly driven by a reduction of parasitic combustion that is associated with detonative combustion. In addition, the shock front is more well-defined for the $\dot{m} = 700$ g/s case (Fig. 5.22) as opposed to the $\dot{m} = 300$ g/s case (Fig. 5.21), where the high-pressure region is observed only at the top of the detonation wave and a small region of unburnt gases is present ahead of the detonation wave. In other words, at low mass flow rates, the pressure profile can be highly varying due to the competition between parasitic combustion and fuel-air mixing. The shock structure in the $\dot{m} = 700$ g/s case is similar to the thickened front found in linear model experiments [71] and simulations [37].

5.8.3 Statistical analysis

The above findings can be understood from a mixing standpoint by considering time-averaged statistics. Figure 5.23 shows azimuthally averaged mixture fraction (equivalent to equivalence ratio) and temperature across a radial section of the channel. Overall, average mixture fraction shows similar profiles, indicating that fuel distribution within the chamber is not significantly different. In particular, the fuel jet is deflected upwards (axial direction) by the oxidizer jet, with local fuel-to-air ratios exceeding stoichiometric condition. At the same air mass flow rate, the higher equivalence ratio case shows higher jet penetration, driven by the higher flow rates through the fuel ports. Further downstream, the equivalence ratio decreases with close to stoichiometric values found past 40 mm. However, the temperature profile is highly altered by the change in the equivalence ratio and mass flow rate. In the $\dot{m} = 300$ g/s cases, there exists a small region of high temperature in between the inner wall and the fuel inlet which becomes wider for $\phi = 0.75$. This region is responsible for the recirculation of product gases that results in the parasitic deflagration region bounded between CB2 and the air/fuel injectors (Fig. 5.21). In the $\dot{m} = 700$ g/s case, there is a much larger region of high temperature near the inner wall, which promotes the CB2 deflagration process. Further, the $\dot{m} = 300$ g/s cases show higher temperatures past the detonation height, which indicates continued deflagration and heat release, while the $\dot{m} = 700$ g/s rate indicates lower temperatures at downstream locations.

Figures 5.24 and 5.25 show time-averaged velocity at the exit of the injectors for three cases. For both fuel and air inflows, the peak velocities are roughly the same for the two cases. The response of the fuel injector is not significantly altered by the mass flow rates. Given that the fuel holes are smaller, the injector is generally stiffer than the air injectors. As a result, the response to the detonation wave including the time taken to recover to the full injection velocity is nearly identical for three

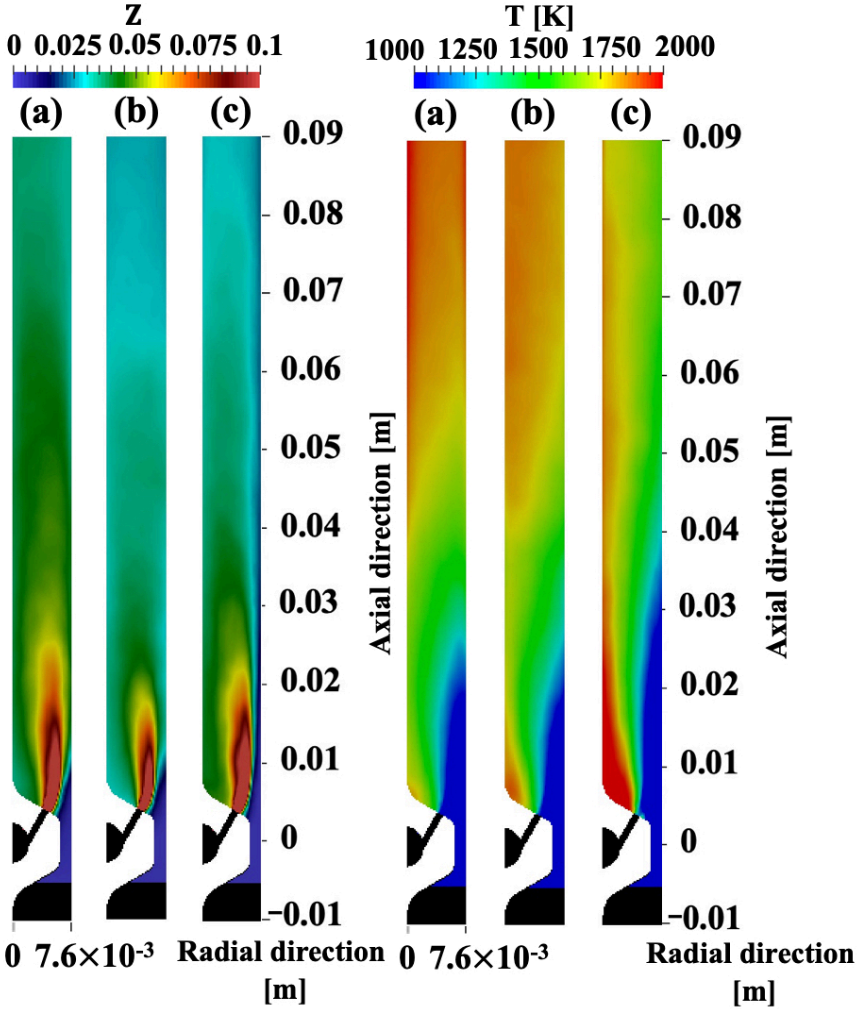

Figure 5.23: Azimuthal averaged mixture fraction and temperature for (a) $\dot{m}$ = 300 g/s at ϕ = 1.0, (b) $\dot{m}$ = 300 g/s at ϕ = 0.75, and (c) $\dot{m}$ = 700 g/s at ϕ = 0.75.

cases. However, the air injector shows considerable differences in the response to the detonation wave. In the $\dot{m}$ = 300 g/s cases, the injectors remain blocked for a longer duration, with a shallow recovery to the fully unblocked state. When the mass flow rate is increased, the blockage time is considerably reduced, with the injector recovering quicker to the full velocity mode. It is seen that the $\dot{m}$ = 700 g/s case causes a second weaker blockage following the first suppression, which implies a three dimensional pressure reflection in the chamber. Moreover, the lowest velocity observed is considerably higher for the $\dot{m}$ = 700 g/s case. Considering that the detonation wave is much stronger, this lower blockage indicates two aspects: a) the higher plenum pressure makes the injector stiffer and reduces the impact of higher detonation pressure and b) stronger detonations lead to a confined region of pressure increase, which allows the injectors to recover faster.

The net effect of differences in the oxidizer and fuel injector response is to alter the axial distribution of oxidizer and fuel depending on operating conditions (i.e., mass flow rate). In the $\dot{m} = 300$ g/s case, there is a time difference between the recovery of the fuel and oxidizer injectors. As a result, even when operating at a globally stoichiometric condition, the fueling rate can be vastly different leading to regions of very high and low equivalence ratios. On the other hand, the faster recovery in the $\dot{m} = 700$ g/s case causes the air injection to be approximately equivalent to the fuel injection process, leading to more uniform fuel-air mixtures. Moreover, the faster recovery increases the oxidizer velocity and the shear-induced mixing of the fuel and air streams. This leads to fine-scale mixing and better mixture preparation for the passing detonation wave.

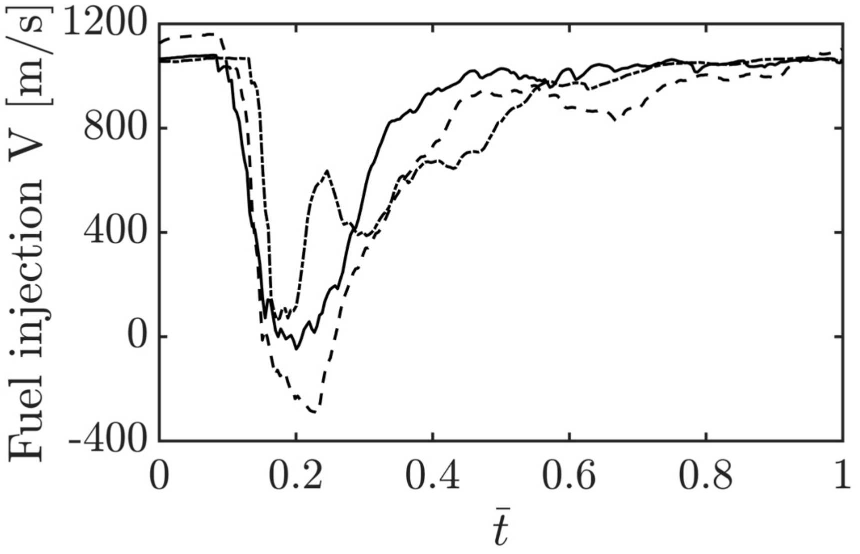

Figure 5.24: Axial fuel injection velocity history for the low and high mass flow rate cases obtained by averaging over multiple detonation cycles. (Solid line) $\dot{m} = 300$ g/s at $\phi = 1.0$, (dashed line) $\dot{m} = 300$ g/s at $\phi = 0.75$, and (dashed-dot line) $\dot{m} = 700$ g/s at $\phi = 0.75$.

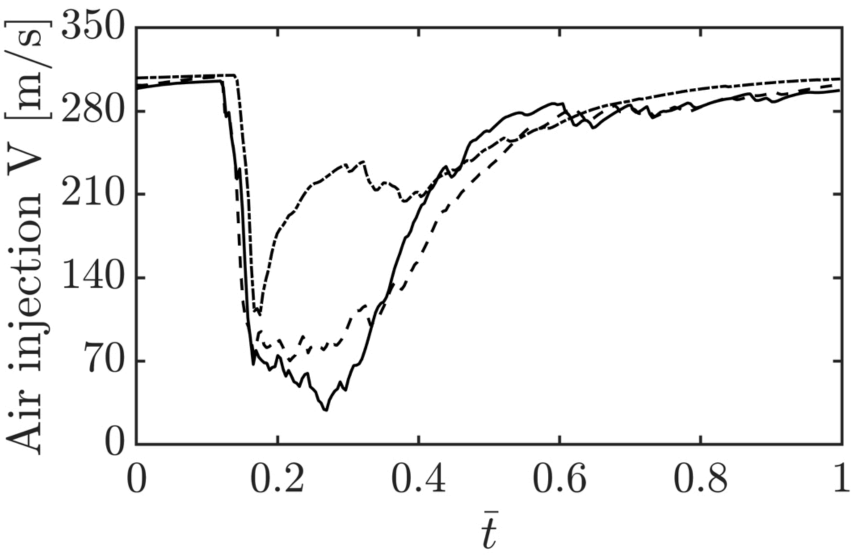

Figure 5.25: Axial air injection velocity history for the low and high mass flow rate cases obtained by averaging over multiple detonation cycles. (Solid line) $\dot{m}$ = 300 g/s at $\phi = 1.0$, (dashed line) $\dot{m}$ = 300 g/s at $\phi = 0.75$, and (dashed-dot line) $\dot{m}$ = 700 g/s at $\phi = 0.75$.

A final analysis regarding heat release location is presented next. Here, the time at which maximum heat release occurs at a particular point in the cross-sectional plane is obtained. For this purpose, consider the schematic shown in Fig. 5.26. Here, the location of detonation front is marked by time $\bar{t} = 0$. For every location on the cross-section, the time at which maximum heat release occurs as a delay with respect to when the detonation wave reaches that point is measured. Negative values indicate that maximum heat release occurs before the wave arrives, while positive values indicate post-detonation maximum heat release. The time is normalized by the detonation cycle time. Figure 5.27 shows this maximum heat release time for the three cases. It is seen that in the $\dot{m}$ = 300 g/s cases, the inner wall region of the lower part of the domain shows peak heat release before the arrival of the wave, while this pre-wave heat release region is pushed farther downstream in the $\dot{m}$ = 700 g/s case. This region signifies deflagrative burning, due to recirculation of product gases and mixing with fresh gases. The faster recovery in the $\dot{m}$ = 700 g/s case pushes this mixing-induced deflagration to downstream locations.

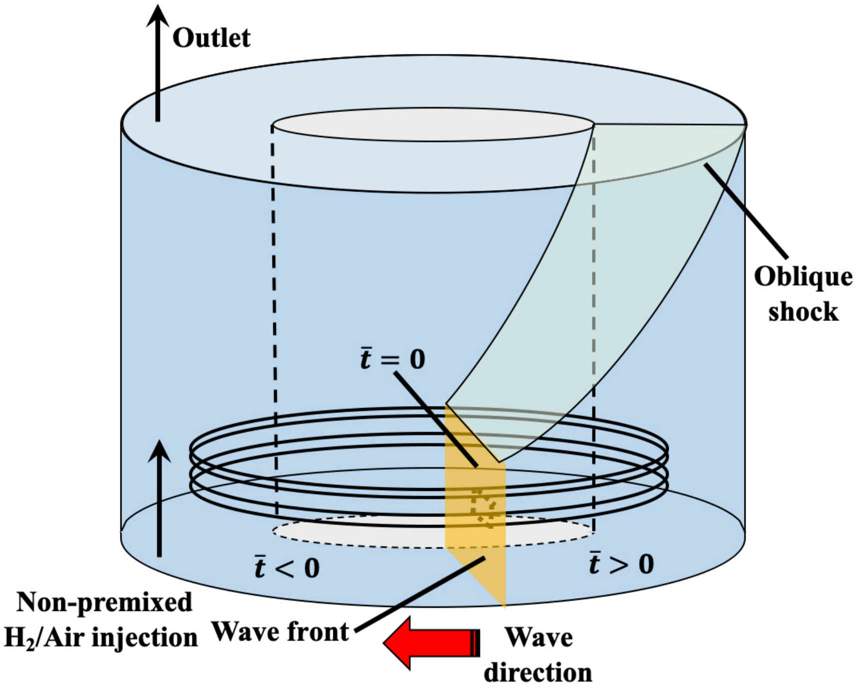

Figure 5.26: Schematic showing the averaging procedure used to obtain the time-delay plots.

The time scale plot only shows the location of the peak value but does not indicate the amount of heat release in pre- and post-detonation regions. As such, it is useful to examine the distribution of the amount of heat release. The normalized and time-averaged heat release plot is also shown in Fig. 5.27. In the $\dot{m} = 300$ g/s cases, heat release is spread across the channel width, while in the $\dot{m} = 700$ g/s case, the presence of the strong detonation wave traversing along the outer wall skews the energy release distribution. It is also found the variation of the equivalence ratio (cases 1 & 2) did not affect the time-averaged heat release. Overall, most of the heat release occurs in the lower half of the domain.

5.9 Conclusion

The axial air injection based RDE design of Chacon et al. [23] for hydrogen/air operation is simulated using detailed chemical kinetics. The RDE flow field shows features that are significantly different from the 2D unwrapped premixed detonations, including the presence of a deflagration region due to recirculation generated by the inlet design. Further, inhomogeneous transport of fuel and air lead to parasitic combustion that directly affect the strength of the detonation process. These features were found to be directly caused by the unsteady response of the injectors to the passing detonation wave. In particular, the recovery of the fuel and oxidizer streams from the shock-induced blockage affected the mixing process. In the composition space, the parasitic combustion effect was shown to manifest as a highly reactive mixture that is processed by the detonation wave. However, the unsteady mixing introduced large fluctuations in composition space, indicating a highly intermittent and stratified fuel-air distribution. Overall, in spite of these variations, the pressure across the wavefront was nearly uniform, but there was considerable spatial asymmetry in temperature with higher values found near the inner wall. Comparisons with experiments show good agreement.

This study demonstrates that stable detonations are achievable in the axial injector system, but to obtain pressure gain or reduce losses, it is essential to optimize the recovery process of the injectors. In particular, premature deflagration is the main source of loss. Consequently, systems that reduce deflagration will potentially achieve higher efficiency.

To study the mass flow effect, two different flow rates were considered. For $\dot{m} = 300$ g/s, the equivalence ratio is varied between 0.75 and 1.0 to see its effect on the mixing and detonation structure. While all simulated cases produced a single wave, the $\dot{m} = 700$ g/s case was closer to the regime where wave splitting has been observed experimentally. Analyses of flow fields, heat release rates, and injector recovery were conducted.

One of the motivations for this work is the observed increase in wave speed with increase in mass flow rate. The experiments corroborated prior observations, indicating that the RDC exhibits similar flow physics. The numerical simulations showed that as mass flow rate is increased, the injector recovery is faster due to the higher plenum pressure. This results in more steady fuel and air injection and better mixing characteristics. The end effect is an increase in the strength of the detonation wave associated with a reduction in parasitic combustion in the fill region. The wave velocity thus increases, even as the detonation height also increases due to a larger refill height.

It is also observed that as wave height increases, autoignition tendency increases in the freshly injected reactants even with minimal mixing of product gases. It is our hypothesis that when such deflagrative burning becomes more dominant, additional weak waves, initially in the form of acoustic waves, could be generated that interact with the main wave to cause splitting of the detonation front. At this point, this process remains merely a hypothesis. Future work will explore the incipient wave splitting process.

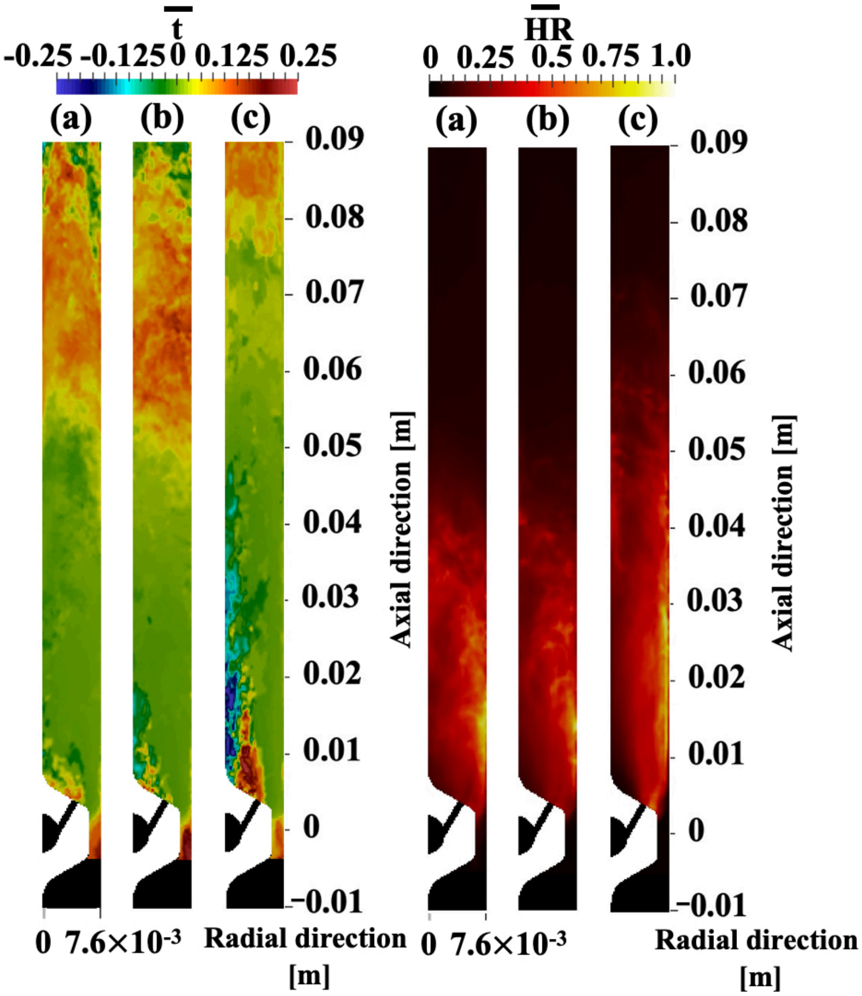

Figure 5.27: (Left) Time delay plot showing maximum heat release at a given cross section point with respect to the detonation wave, and (right) distribution of time-averaged heat release for (a) $\dot{m}$ = 300 g/s at $\phi = 1.0$, (b) $\dot{m}$ = 300 g/s at $\phi = 0.75$, and (c) $\dot{m}$ = 700 g/s at $\phi = 0.75$. The time delay has been normalized by the cycle time of the detonation wave.

CHAPTER VI

Simulation of Ethylene/Air-based RDE

6.1 Hydrocarbon RDEs System

The focus of this study is to obtain insight into the flow features of an ethylene/air-based RDE. The simulation configuration is based on the experiment of Cho et al. [5]. Of particular interest is the detonation wave structure that supports a weak propagation. For this purpose, detailed numerical simulations are conducted. One aspect that requires some discussion is the description of flame kinetics. In most detonation calculations, one step chemical kinetics or reduced order models such as the induction parameter model [7, 84] are used. If the detonations are strong enough such that the propagation speed is close to CJ speed, then such methods have been shown to be reliable in a number of studies. While detailed kinetics models are widely used in combustion simulations, these models have been developed predominantly for deflagrations, and their direct application to detonation calculations still need to be evaluated. To address these issues, the simulations conducted here use both detailed chemical kinetics as well as a detonation-specific reduced order model for ethylene.

6.2 Simulation Configuration

The RDE configuration simulated here is based on the AFRL design used in [5]. This design is similar to the hydrogen/air RDEs used in other related studies [3], but has a larger annulus width to account for the slower ethylene/air chemistry. The wider channel width allows for the triple points to stabilize, which is reflected in the larger cell size for more complex hydrocarbons. Due to this change, the fuel-air mixing structure is different compared to the hydrogen-based RDE. Figure 6.1 shows a schematic of this geometry. The channel width is 22.86 mm, and the area ratio between the oxidizer inlet and the detonation chamber is 0.059 [5]. The air injection slot is 1.778 mm wide. The oxidizer stream and the fuel stream are perpendicular to eat other at the bottom of the chamber.

Several different simulations are conducted here, including the dilution of the fuel with hydrogen to study its impact. A list of simulations is provided in Tab. 6.1. The air mass flow rate is set to 0.7 kg/s for the pure ethylene fuel cases. The total temperature in the air plenum is varied between 300 K-600 K. A total temperature of $T_0 = 300$ K is used for the fuel plenum in every case. The back pressure is 1 atm and 2 atm for the pure ethylene and ethylene with hydrogen addition cases, respectively. The increase in back pressure for the ethylene with hydrogen addition case increases the baseline pressure in the detonation chamber, thereby increasing the detonability of the mixture. The total pressure in each plenum is computed by the choke relation as follows,

$$P_0 = \frac{\dot{m}}{A}\big(1 + \frac{1}{2}(\gamma - 1)\big)^{\frac{\gamma+1}{2(\gamma-1)}}\sqrt{\frac{RT_0}{\gamma}} \tag{6.1}$$

where A is the area, R is the gas constant of each stream, γ is the specific heat ratio, and $\dot{m}$ is the target mass flow rate. When the total temperature of the oxidizer plenum is changed, it affects the total pressure and the post-throat conditions. As a result, the velocity and mixing fields inside the detonation chamber are altered, even for the same mass flow rates. For this reason, changing the total temperature will lead to variations in the combustor behavior that could help understand the detonation features.

To obtain performance related metrics for the RDE, the mass flow rate is computed as

$$\dot{m} = \int_{inlet} \rho u dA_{inj}, \tag{6.2}$$

The net force is obtained as

$$F = \int_{exit} \rho u^2 + (p - p_{back}) dA_{exit}, \tag{6.3}$$

where p_{back} is the imposed back pressure, and u indicates the face-normal velocity. Based on these quantities, the specific impulse is computed as

$$I_{sp} = \frac{F}{\dot{m}_{fuel} g}, \tag{6.4}$$

where g is the gravitational acceleration and $\dot{m}_{fuel}$ is the mass of fuel in a total flow rate of $\dot{m}$.

Composition	P^0_{oxi} [kPa]	P^0_{fuel} [kPa]	T^0_{oxi} [K]	T^0_{fuel} [K]	$\dot{m}_{air}$ [kg/s]	P_{back} [atm]	$W_{Sim.}$ [m/s]	$W_{Expt.}$ [m/s]	$W_{Th.}$ [m/s]	I_{sp} [s]	Chemistry mechanism
C_2H_4/Air	441	292	300	300	0.7	1	1070	1020	1824	1936	Two-step [85]
C_2H_4/Air	509	292	400	300	0.7	1	1171	—	1814	2122	Two-step [85]
C_2H_4/Air	623	292	600	300	0.7	1	—	—	1797	1783	Two-step [85]
C_2H_4:H_2(50:50)/Air	441	420	300	300	0.7	2	1328	—	1857	2271	Detailed [67]

Table 6.1: Details of the simulations and summary of macroscopic results.

A baseline computational grid is generated with the minimum grid spacing of 3 $\times 10^{-4}$ m. A hexahedron-dominant mesh is used. The near-injection region as well as the detonation region contain clustered grid points to resolve the sharp gradients. This mesh spacing is similar to other related studies [73, 86]. The mesh near the injection system is shown in Fig. 6.1. The total number of computational volumes is about 30 million. In this study, heat transfer to the walls is not considered, primarily because the total run time will not allow any meaningful steady state to be reached. Due to the supersonic flow in the domain caused by detonation waves and the short operation time of RDEs (approximately a few seconds), the heat transfer to the wall is neglected in this study. In the post-detonation plenum, the side walls are treated using zero gradient conditions for both velocity and energy. The exhaust outlet uses a zero-gradient condition for both velocity and energy equations. Each simulation takes approximately 1.5 weeks to complete using 3000 CPU cores on NASA Pleiades supercomputer.

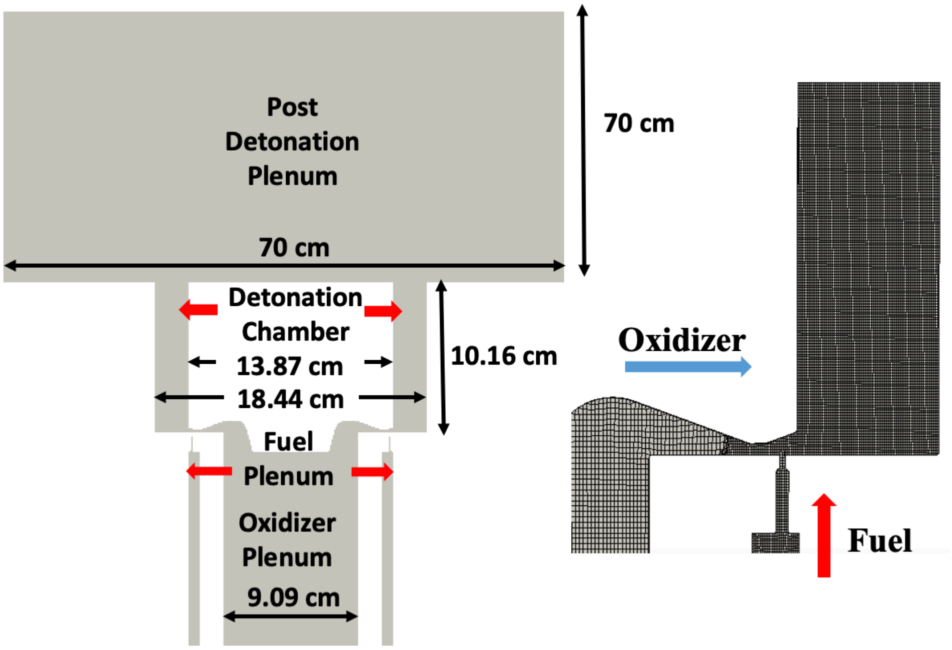

Figure 6.1: (Left) Computational geometry and RDE configuration with dimensions and (right) the fuel and oxidizer injection configuration with computational mesh.

The simulations are performed as follows. Starting with a uniform flow field, the fuel and oxidizer jets are allowed to evolve in the domain without any chemical reactions. Once this development is complete and fully-choked conditions are established for both sets of injectors, a high temperature region is patched within the annulus with gas conditions replicating the one-dimensional post-detonation values (obtained from 1D simulation data). This flow is allowed to evolve for sufficient time until a statistically stationary detonation field is observed. Note that the time required to reach this state is highly dependent on the flow and initial conditions. After reaching this stationary state, the simulation is continued and data is collected for evaluating statistics such as wave velocity or shock structure. The total simulation time for this phase is equivalent to roughly 4-5 cycle periods after reaching steady state operation. In the discussions below, only results from this phase will be presented. In this study, the grid in the mixing region is sufficiently fine to resolve most of the large scale structures. In similar simulations of complex flows [87, 88], it has been found that the contribution from sub-filter models are minimal. For this reason, sub-filter models are not used in this work.

6.3 Deflagrative Mode in the RDEs

The cases with pure ethylene without hydrogen dilution are discussed first since there exists experimental data for direct comparison for one of the cases (Tab. 6.1).

Figures 6.2, 6.3 and 6.4 show the general behavior for different inflow temperatures. While the 300 K and 400 K air cases reveal a visible wave front, it is indistinct for the 600 K air case. The high temperature region behind the front indicates that the wave is sustained due to the chemical reaction for the lower inlet temperature cases. Interestingly, the high pressure region appears farther downstream of the lower wall for the 300 K case compared to the 400 K case. This observation is also reported in the experiment, where the wave front is offset from the base [5].

The equivalence ratio distributions show interesting trends. In the lowest temperature (300 K) and highest temperature (600 K) cases, the fuel is reasonably well mixed across the channel width, with near stoichiometric conditions. On the other hand, the 400 K simulation shows larger variations near the outer wall of the chamber. While these are instantaneous snapshots, this non-mixedness was observed at many time instances, indicating a difference in the mixing behavior of these systems. Moreover, all cases show significant variations in the temperature field across the detonation cross-section, indicating a highly non-uniform detonation process. For instance, the wave appears weaker near the mid-channel while the temperature fields show a clear post-detonation condition at this location. This indicates that the wave is undergoing some radial motion, akin to slapping modes, which sets up a radial entrainment process locally.

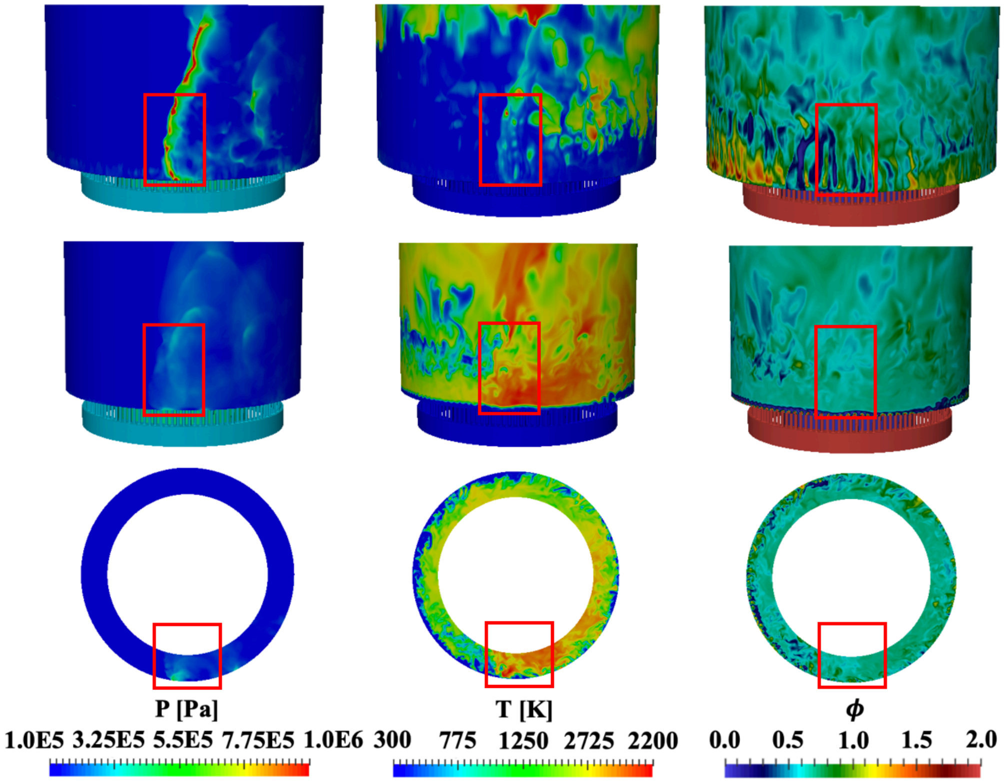

Figure 6.2: Pressure, temperature, and equivalence ratio fields for $T^0_{oxi} = 300$ K. (Top) outer wall, (middle) mid-channel, and (bottom) a cutting plane 2 cm from the chamber bottom.

Figure 6.5 and 6.6 show the species and pressure behavior plotted as a function of distance from the shock front for the 300 K and 400 K air cases. Profiles are extracted along the circumference at mid-channel distance and outer wall at 5 mm from the chamber bottom. Since the wave structure is highly three dimensional and unsteady, six different snapshots are processed to obtain the averaged profiles.

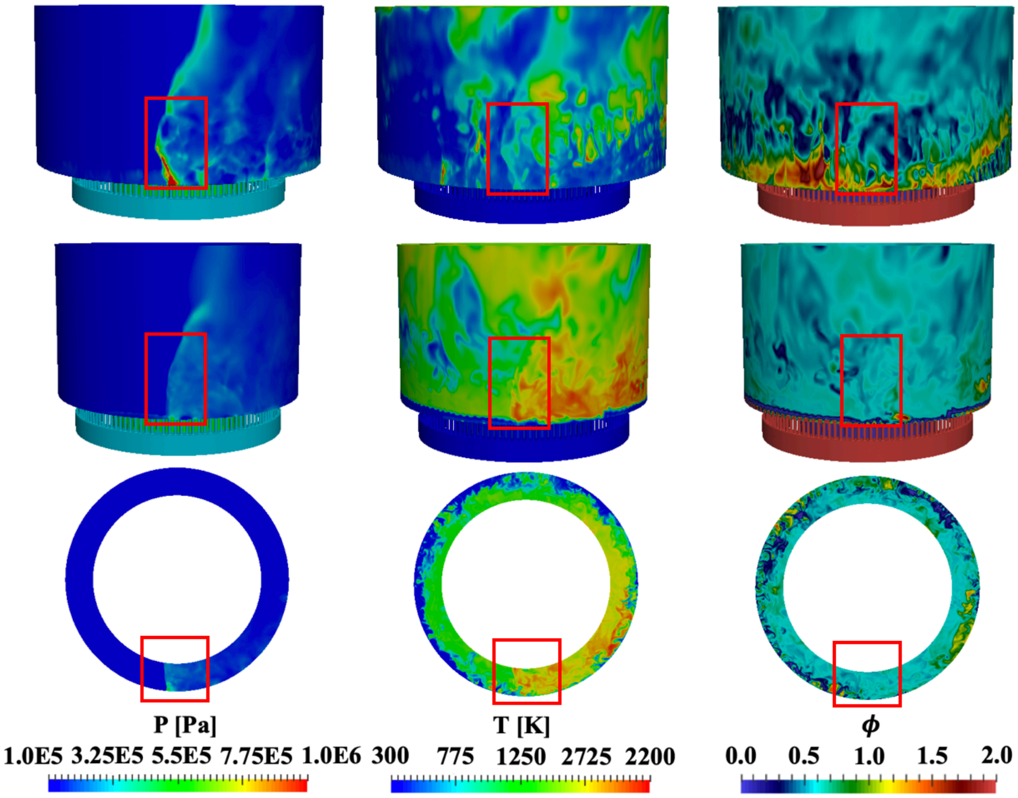

Figure 6.3: Pressure, temperature, and equivalence ratio fields for $T_{oxi}^0 = 400$ K. (Top) outer wall, (middle) mid-channel, and (bottom) a cutting plane 2 cm from the chamber bottom.

Compared to the 1D profile [76], the peak pressure drops significantly for the full system simulation, which is about 60% of the pressure in the ideal case. It is also seen that the pre-detonation pressure is almost 1 atm and close to the exit backpressure. The oxidization process at the mid-channel is much slower and the peak pressure is lower compared to values at the outer wall. Furthermore, there is residual product gases from the previous cycle mixed with fresh gases, leading to partial combustion before the wave arrives. This premature deflagration is one of the reasons for the weak detonation observed here. In fact, the computed wave speed is almost 60% of the CJ velocity as tabulated in the Table 6.1. The CJ velocity is computed for the premixed condition using the global equivalence ratio using T_{oxi}^0 as the temperature of the fresh gases. This low wave speed is also observed in the experiment [5].

Figures 6.7 and 6.8 show the temperature and pressure as a function of distance

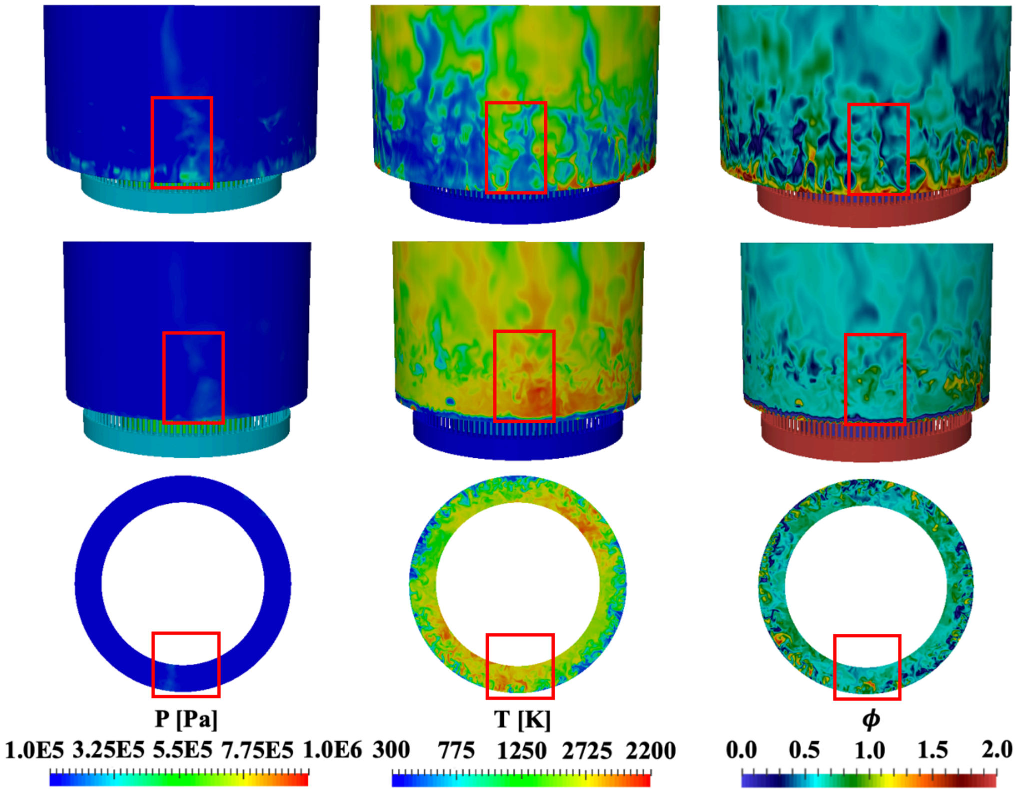

Figure 6.4: Pressure, temperature, and equivalence ratio fields for $T^0_{oxi} = 600$K. (Top) outer wall, (middle) mid-channel, and (bottom) a cutting plane 2 cm from the chamber bottom.

from the shock front for the 300 K and 400 K cases. As observed in the contour images (Fig. 6.2), the 300 K case exhibits higher temperature near the mid-channel compared to that near the outer wall. In fact, the post-wave increase in temperature is extremely weak. On the other hand, the 400 K case shows higher temperature near the outer wall as compared to the 300 K case, and comparable profiles near the mid-channel. In both cases, the temperature is higher near the mid-channel and is sustained for longer distances behind the shock, compared to the outer wall profiles. This is possibly due to larger fluctuations in equivalence ratio near the outer wall. Note that the peak value of the 400 K air case (1800 K) is still much lower than the CJ state value (approximately 2800 K). The 300 K air case does not show a similar increase in this time-averaged temperature profile. In other words, the reaction is not continuously sustained behind the shock at a height of 3 mm from the base of the chamber for the

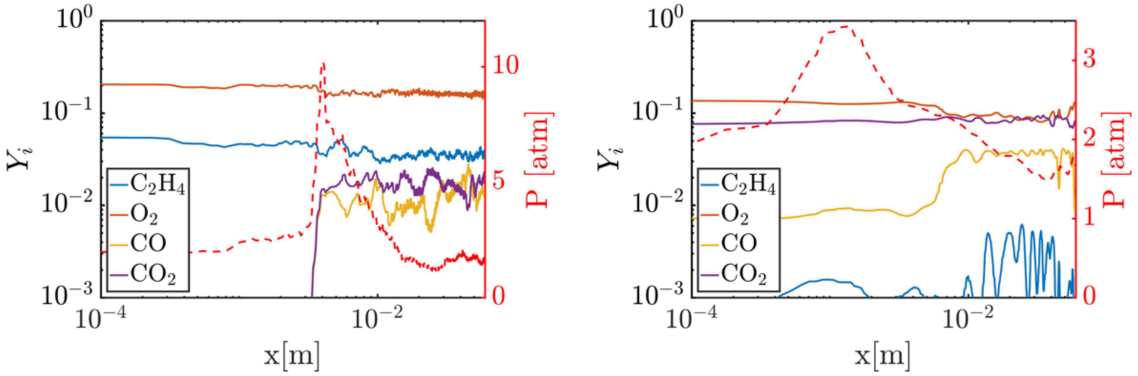

Figure 6.5: Species behavior and pressure profile across the shock for $T^0_{oxi} = 300$ K case. (Left) outer wall and (right) mid-channel.

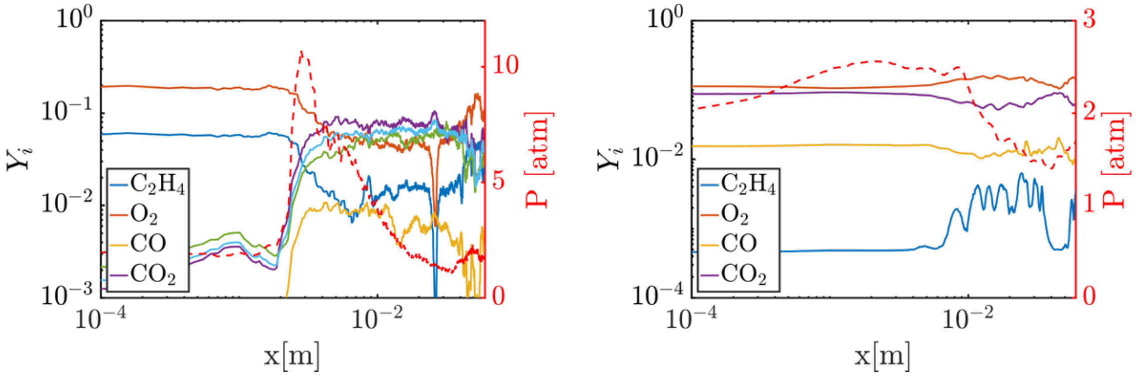

Figure 6.6: Species behavior and pressure profile across the shock for $T^0_{oxi} = 400$ K case. (Left) outer wall and (right) mid-channel.

300 K air case unlike for the 400 K air case. This is also due to the dependency of the mixing process on the air temperature, which will be discussed later. At the the mid-channel, both cases exhibit almost flat temperature profiles along with a smooth pressure rise. This indicates that the reaction happens in the broad region behind the shock (or a strong pressure wave) without a Von Neumann spike as seen in a one-dimensional detonation structure or in practical pulse detonation devices [19].

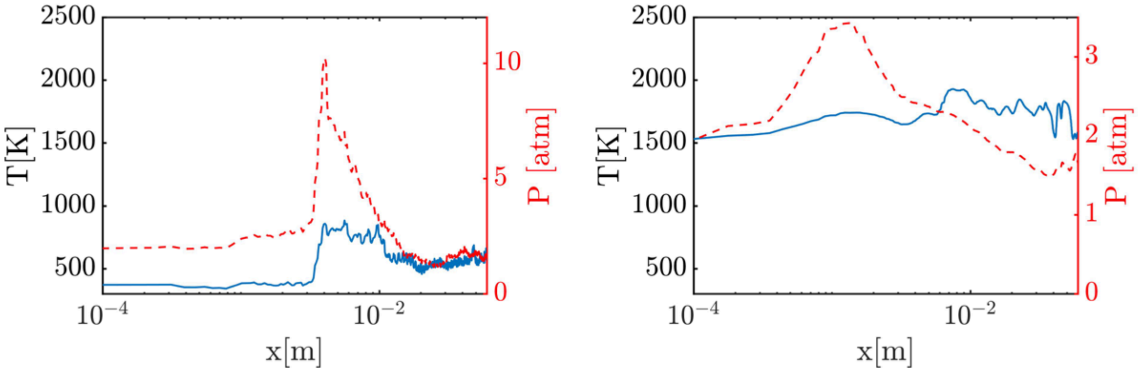

Figure 6.7: Temperature and pressure profiles across the shock for $T^0_{oxi} = 300$ K case. (Left) outer wall and (right) mid-channel.

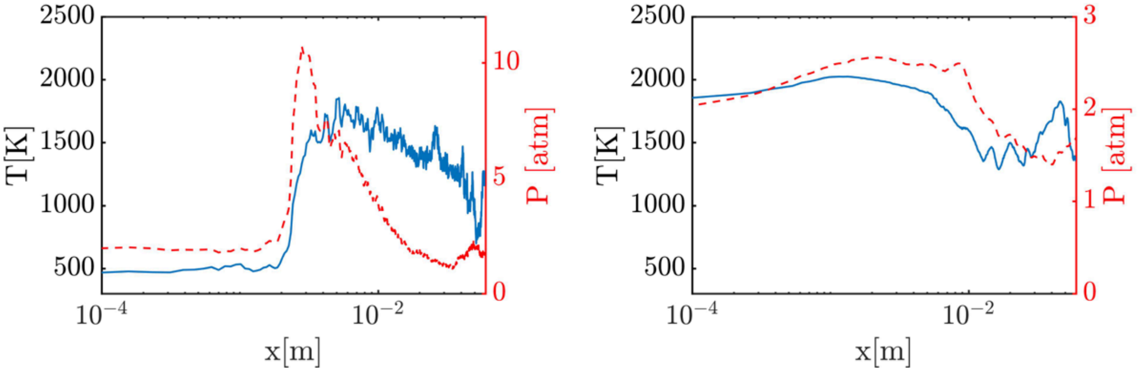

Figure 6.8: Temperature and pressure profiles across the shock for $T^0_{oxi} = 400$ K case. (Left) outer wall and (right) mid-channel.

6.4 Injeciton and Mixing with Ethylene RDEs

To understand the source of this incomplete detonation process, it is useful to analyze the mixing process near the fuel-air injection region. Figure 6.9 shows the time sequence of equivalence ratio for all three cases. Since the mass flow rate is identical for all cases but the inflow density changes, the velocities of the fuel and air streams are different. This creates a difference in the mixing process among the different cases. The 300 K case shows that leaner mixtures form in the lower part of the domain, leading to near stoichiometric values further downstream. Further, the oxidizer stream enters the chamber along the bottom wall and creates a recirculation region supported by the inner chamber wall. Recalling that the detonation wave is weaker near the bottom of the domain for this case (Fig. 6.7), this feature may be attributed to poorer mixing in this region. On the other hand, 400 K and 600 K cases show a more stratified structure in the axial direction. The 400 K case shows that the $\phi = 1.0$ region exists at the chamber bottom near the outer wall while these regions are found near the inner wall for the 600 K case. The interesting point here is that a stable wave cannot be formed for the 600 K air case as shown in Fig. 6.4. These results indicate that a higher degree of stratification leads to a reduction in detonation efficiency. Prior canonical simulations [89] show that stratification alters the detonation cell size and propagation features. Given this result, the current set of observations is not surprising. It is interesting that even when the air inflow is heated (600 K), the lack of adequate mixing can lead to unstable wave propagation.

Figure 6.10 shows the time history of the injection velocity for the fuel and oxidizer injector. The velocity is measured at the center of each injector on its exit plane. The time is normalized by the time required for a detonation wave to complete one cycle. Since the wave velocity cannot be calculated for the 600 K case, the wave speed of the 400 K case is used to normalize the time of the 600 K case. For all the cases, the velocity of the oxidizer injector is almost constant during the operation. This indicates that the wave in the chamber is too weak to affect the oxidizer injection behavior. This behavior is different from prior studies of hydrogen/air RDEs [3, 73], where the strong wave feedback into the oxidizer plenums would lead to periodically unchoked flow. More importantly, burnt gases from the detonation chamber could travel into the feed plenums, leading to changes in the ignition characteristics of the reactant gases. Here, however, the injection velocity recovers immediately after a wave passes through, thereby minimizing any flow back into the feed plenums.

Another useful metric in analyzing detonation performance is the heat release rate

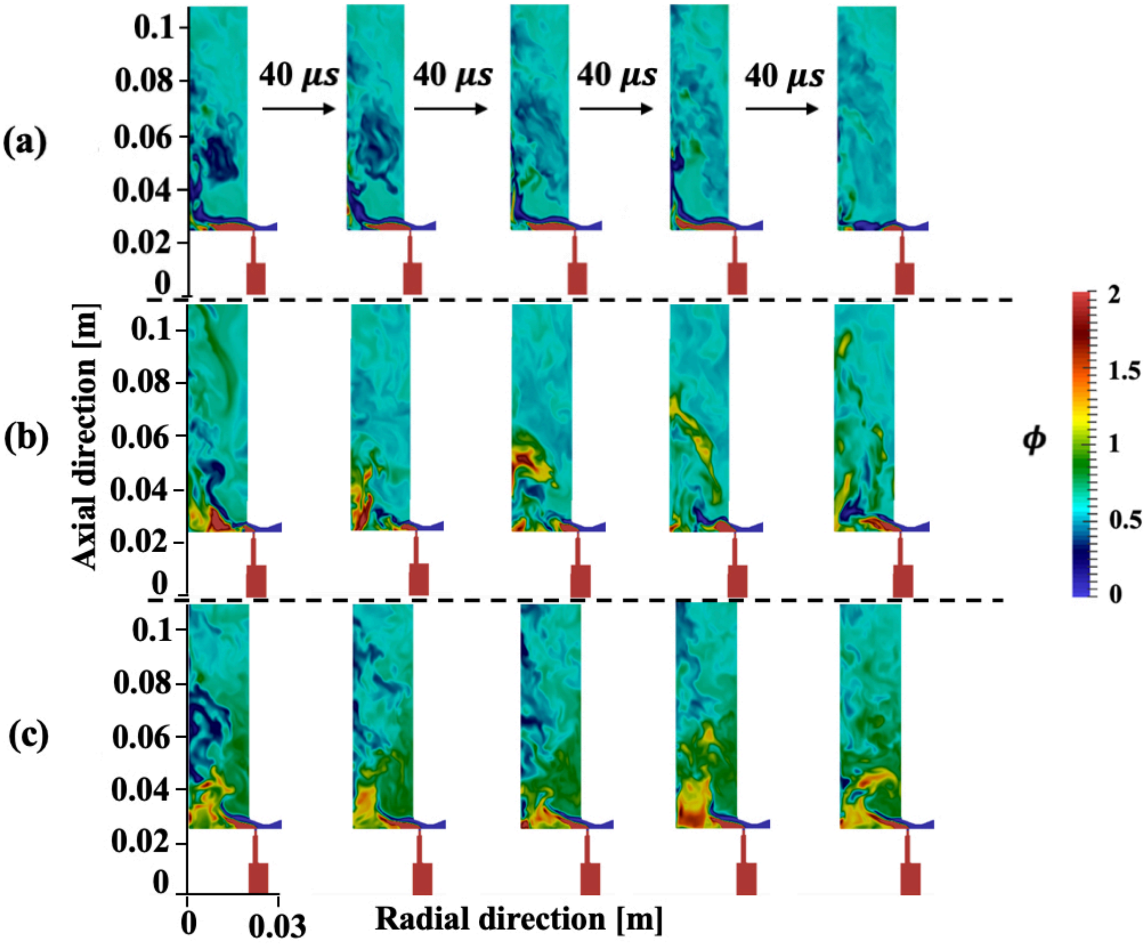

Figure 6.9: Time history of equivalence ratio at a cutting plane at the injector location for: a) $T^0_{oxi} = 300$ K, b) $T^0_{oxi} = 400$ K, and c) $T^0_{oxi} = 600$ K air cases. The time shifts from the left figure to the right figure by 40 μs between each frame.

plotted as a function of pressure. In such pressure gain devices, the design goal is to support heat release at higher pressures. However, due to mixing inefficiencies and the finite rate of chemical reactions, achieving this ideal scenario is difficult. Figure 6.11 shows the heat release fraction for the three cases. In spite of the differences in spatial structure, all three cases produce similar heat release rates. While the peak pressure behind the wave can be significantly higher than the baseline pressure of 1 atm, much of the heat release happens in the 1-3 atm pressure range. This suggests that the compression wave is detached from the heat release region, and that the shock wave itself is not a continuous planar front but marked by small regions of compression waves. To complete the picture, Fig. 6.12 shows the Rankine-Hugoniot (R-H) plot obtained from the pressure and specific volume at each grid point in the domain as a scatter plot. It is important to recognize that this data does not signal the progression of a single fluid element in the pressure-specific volume space (which is the original intent of R-H representation), but only shows the instantaneous states of the fluid inside the domain. It is seen that only the 400 K case shows fluid states with high degree of compression, corresponding to a detonation process. The other cases show lower pressure in much of the domain. These results can then be compared to the macroscopic quantities evaluated in Tab. 6.1. As expected, the 400 K case shows a higher specific impulse, due to the presence of high pressure regions within the domain.

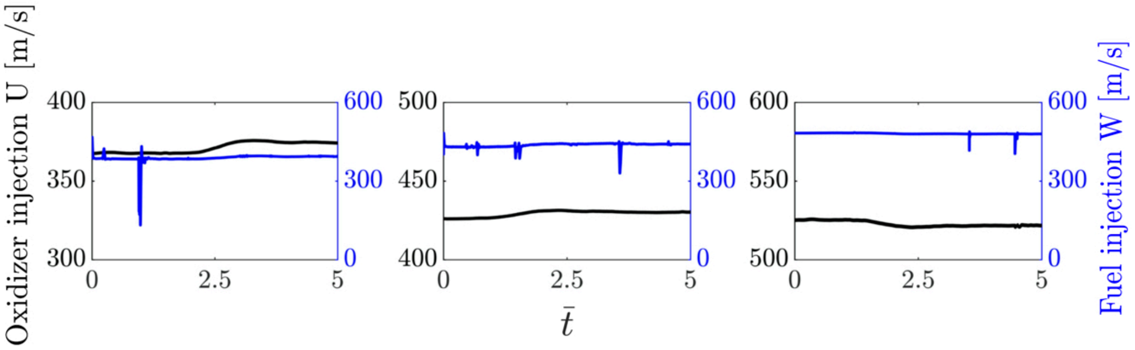

Figure 6.10: Time history of the injection velocity for (left) $T^0_{oxi} = 300$ K, (middle) $T^0_{oxi} = 400$ K, and (right) $T^0_{oxi} = 600$ K cases.

6.5 Dilution with Hydrogen

In this section, the case of ethylene fuel with hydrogen addition is discussed. Due to the higher reactivity of hydrogen, this configuration should, in theory, be a more detonable system. Table 6.1 shows the inflow conditions for this case, which has 50% hydrogen by volume in the fuel. However, it was found that the backpressure

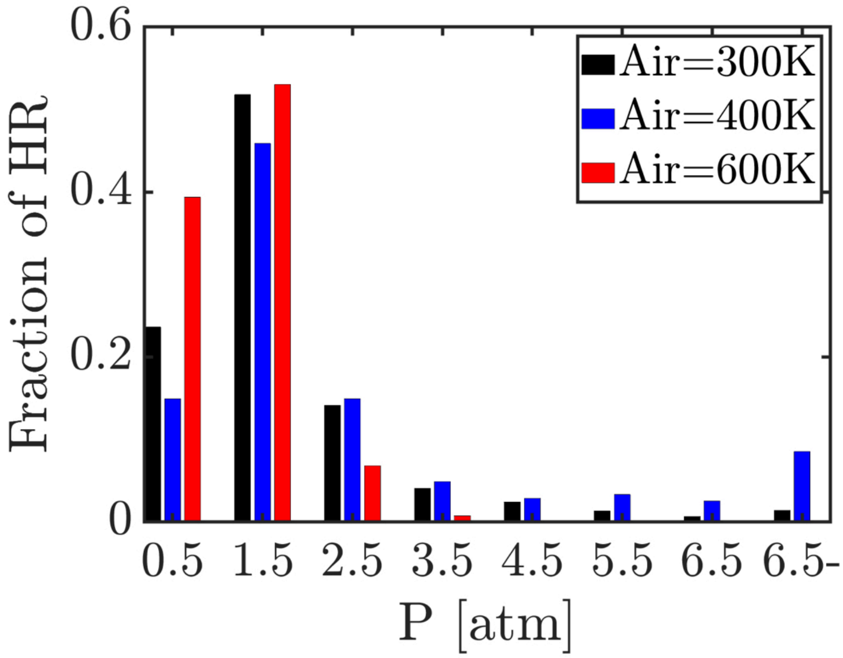

Figure 6.11: Heat release rate fraction plotted as a function of the local pressure for each case.

needs. to be increased to 2 atm to ensure substantial change in detonation behavior compared to the pure ethylene cases.

This case shows considerable variations in the detonation structure before reaching a stable condition. In Figure 6.13, the pressure field at three different instances are shown. For the first 5 cycles, the strong wave mode (left column) and the weak wave mode (middle column) are both observed as the system transitions between these structures. In the strong wave mode, the high pressure locally appears at the wave front and the detonation wave is nearly planar, close to an ideal detonation wave. On the other hand, the weak wave mode reveals a curved wave front with the relatively low pressure increase. After several such transitions, the system reaches the stable mode as shown (right column). In the stable mode, the high pressure region appears along the wave front. Compared to the pure ethylene case, the detonation wave is taller with no standoff from the base of the channel. It is important to note that the wave is weaker for all observed modes at the middle of the channel. This trend

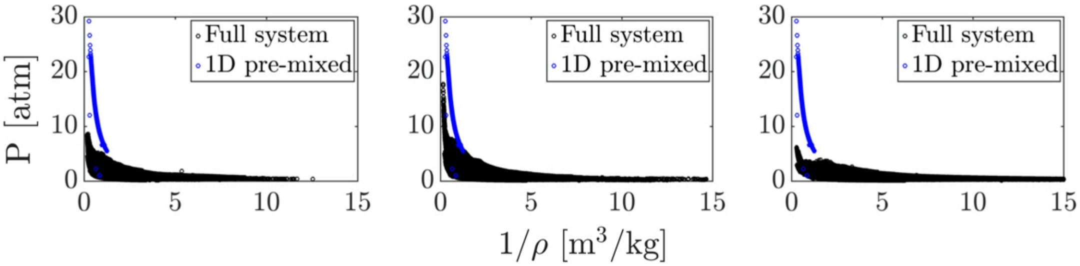

Figure 6.12: Pressure vs. specific volume relation for (left) $T^0_{oxi} = 300$ K, (middle) $T^0_{oxi} = 400$ K, and (right) $T^0_{oxi} = 600$ K cases.

is similar to that observed for the pure ethylene case. The bottom row of Fig. 6.13 shows the axial cutting place data at 2 cm from the chamber bottom. The detonation front is always stronger near the outer wall, but is characterized by a planar structure for the strong wave mode, and a more curved front for the stable and weak modes.

These differences in detonation structures are found to be directly related to the local mixing effectiveness, similar to that in the pure ethylene cases. Figure 6.14 shows the equivalence ratio distribution for the same time instances shown in Fig. 6.13. It can be seen that the three states contain significantly different fuel dispersion processes. In particular, the stable mode exhibits relatively low stratification. The fact that the system transitions back and forth between the strong and weak modes shows that the fuel-air mixing is vastly altered by the passing detonation wave, and the system responds at time scales that are longer than the cycle period. Such long term unsteadiness has been observed in other studies as well [26, 90].

Since the wave is relatively strong compared to the pure ethylene cases, the injection dynamics are also different as seen in the previous section. Figure 6.15 shows the time history of the injection velocity at the exit of fuel and oxidizer injectors. The time is normalized by the 1 cycle time scale based on the wave speed tabulated in Table 6.1. The time history is taken in the stable wave mode after unsteady transition period between the strong and weak wave modes. It is seen that there is a reduc-

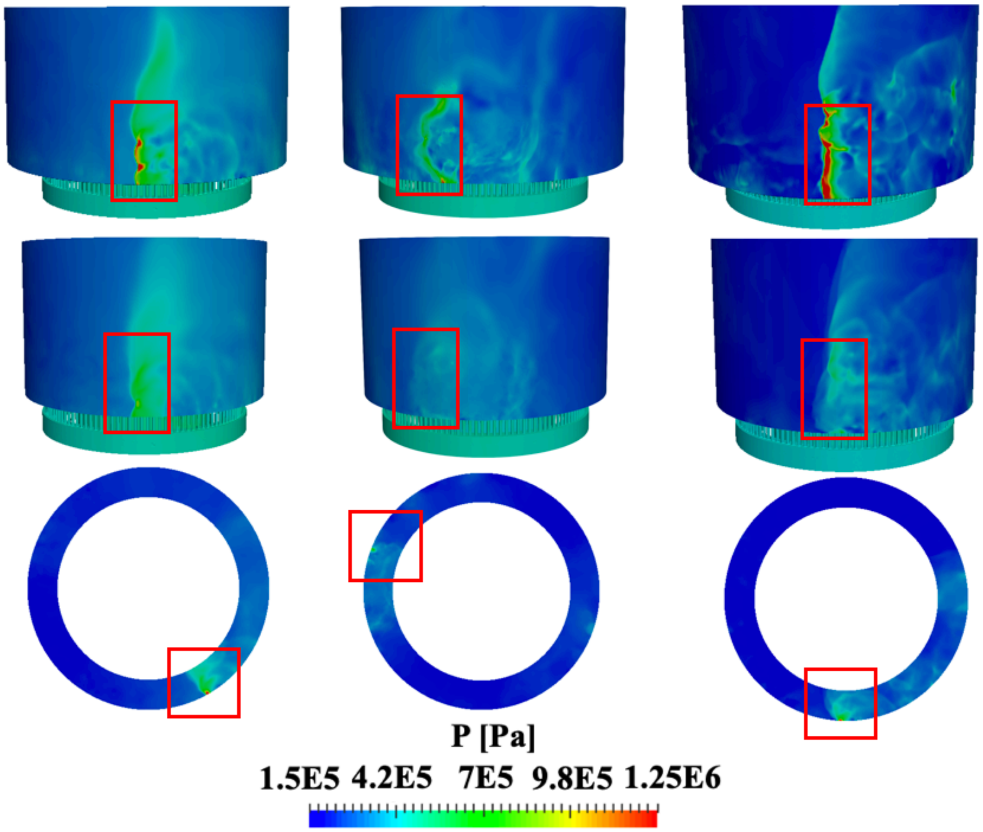

Figure 6.13: Pressure field for the C_2H_4:H_2 (50:50) mixture case showing the strong, weak and steady state wave structure. (Top) outer wall, (middle) mid-channel, and (bottom) cutting plane 2 cm from the chamber bottom.

tion in flow rates every time a wave passes over the injector. The oxidizer injector smoothly recovers to the original state in approximately half a cycle time scale after the flashback while the fuel flow recovers with larger fluctuations. Despite the differences in the recovery time scale for the fuel and oxidizer injection, the cycle-averaged analysis reveals that both of the injectors recover the choked flow in $\bar{t} = 0.5$ after the passage of the wave.

Figure 6.16 shows the heat release rate as a function of pressure. Even though the detonation wave is stronger, heat release still occurs at relatively low pressures, dictated by the back pressure. indicating a non-ideal detonation process. Similar to the pure ethylene case, the Rankine-Hugoniot plot (Fig. 6.15) shows lower local pressure in comparison to an ideal detonation wave. Although hydrogen addition

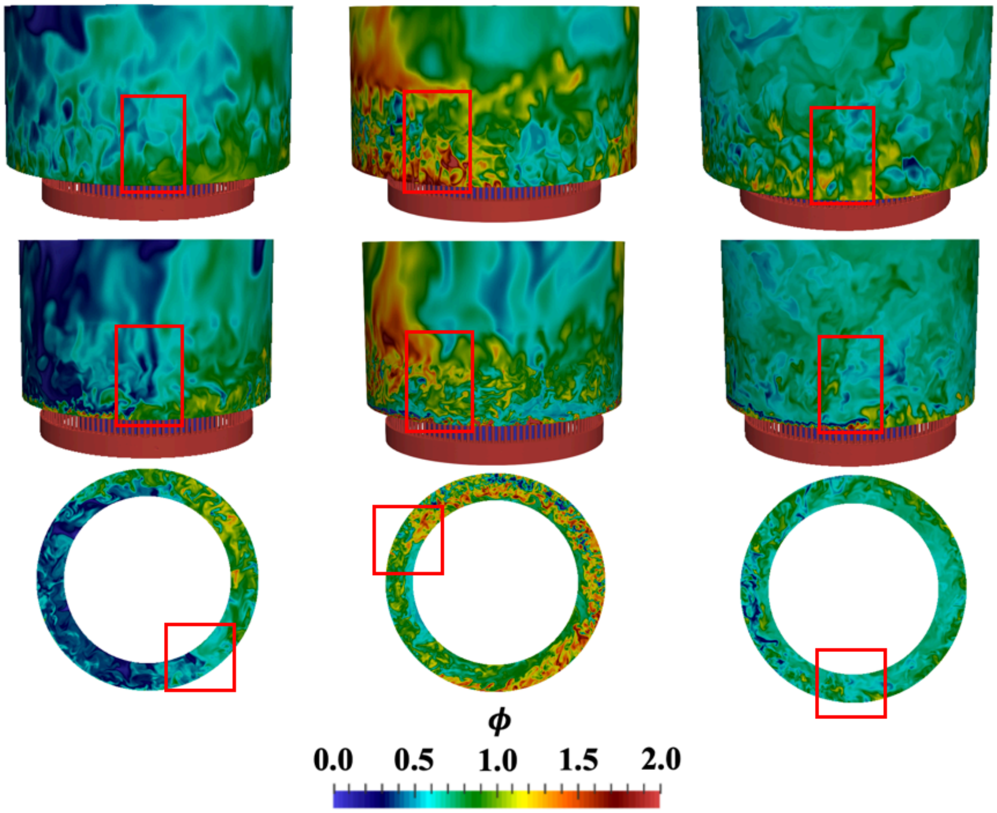

Figure 6.14: Equivalence ratio field for the C_2H_4:H_2 (50:50) mixture case for the strong, weak and steady state wave structures. (Top) outer wall, (middle) mid-channel, and (bottom) cutting plane 2 cm from the chamber bottom.

increased detonability, the system is still not functioning as an ideal pressure gain system, with much of the heat release controlled by the slower oxidation process of ethylene. Of course, increasing the hydrogen content of the fuel will ensure stronger detonations and move the system towards higher pressure heat release. However, such strong detonations can also lead to increased backflow into the feed plenums.

6.6 Summary and conclusion

Detailed simulations of ethylene-based RDEs were conducted for a range of operating conditions with both pure ethylene and hydrogen-diluted fuel streams. The simulations showed that the experimentally observed wave suppression might be re-

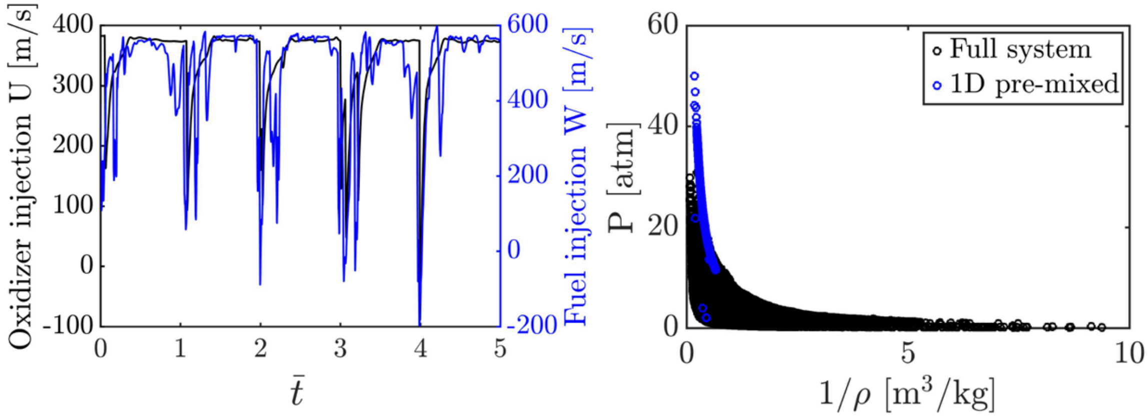

Figure 6.15: (Left) time history of the flow velocity at the injector exit and (right) pressure vs specific volume relation for the C_2H_4:H_2 (50:50) mixture case.

lated to the existence of multiple combustion modes. In the case with hydrogen dilution, it was observed that the combustor switches between a strong and weak mode, but still resulting in propagation speeds that are much lower than the ideal wave speeds. It is hypothesized that the two modes arise due to different phenomena: the strong mode is formed when the mixing and detonation processes reach a synchronized state, while the weak mode dominates when the mixing processes are trying to recover after the passage of a detonation wave. While these features are present even in pure hydrogen RDEs, the strong detonation waves observed there dominate the energy conversion process. Due to the relatively weak detonability of ethylene, the time to recovery is much longer. In the pure ethylene-based operation, only the weak mode is observed. As a result, fuel oxidation occurs through deflagration, supported by the slow axial velocity in the domain. The transverse injection aids mixing, while the weak azimuthal wave propagation consists of a trailing reaction region that enables ignition. Overall, the pressure rise in these pure-ethylene systems is not high, reaching up to 3-4 times the baseline pressure.

These simulations support the experimental observations, but this does not guarantee that both simulations and experiments produce particular flow features for the

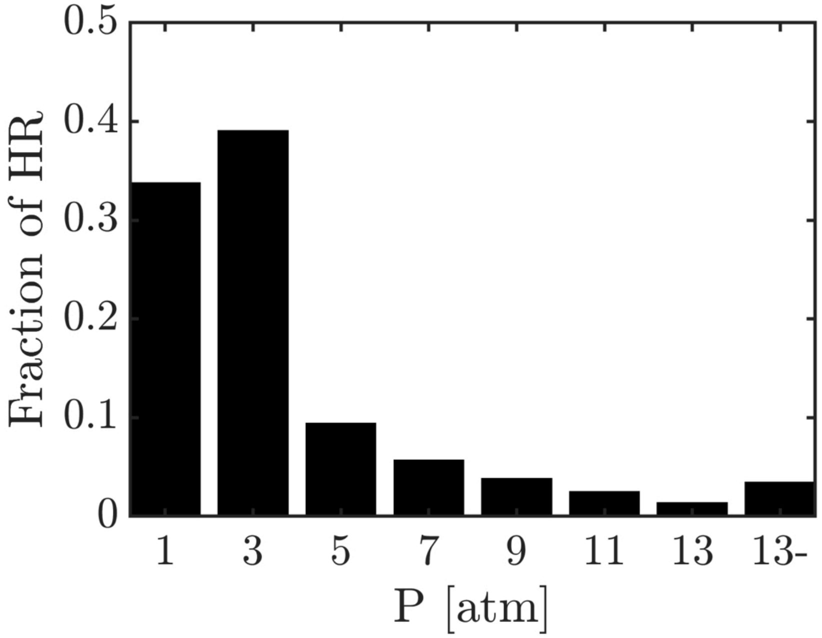

Figure 6.16: Heat release rate fraction plotted as a function of the local pressure for the C_2H_4:H_2 (50:50) mixture case.

same reasons. While more high-fidelity experiments are necessary for validation, these simulations can be used to determine the characteristics of these weakly-detonating waves. It is interesting that although these waves are weak, they stabilize over many cycles by inducing a broad, deflagrative reaction zone.

CHAPTER VII

Conclusions and Future Directions

7.1 Conclusions

The objective of the dissertation is 1) to develop a reliable and highly scalable solver that enables the full system RDE calculations, and 2) to provide high-fidelity simulation data set to the RDE community to accelerate the design optimization process. A FVM solver is developed using the open source framework, OpenFOAM and Cantera, in this study. The developed solver, UMdetFOAM, has been rigorously verified with canonical and experimental configurations. UMdetFoam has capabilities to deal with any complex geometry and chemical mechanisms. As a result, it gives a new capability to the RDE community to assess the detailed physics in a realistic configuration with minimal assumptions. To address the detailed dynamics of the system with a variety of injection schemes and fuels, a radial air inlet, an axial air inlet, and hydrocarbon chemistry are studied in this work.

Prior experiments have shown that RDEs operate under mixing-limited conditions, which leads to spurious losses. For instance, a deflagration region ahead of the detonation wave is known to be present due to interaction of products from the previous wave with fresh gases. However, the details of this deflagration process, and its impact on wave dynamics have not been studied before. Simulations in this study reveal that the combustor exhibits a parasitic combustion (PC) region and a buffer region that separates burnt gases from the parasitic combustion region. Mixture stratification is observed in the PC region that causes incomplete combustion. These regions are present in all the combustors studied, but with differing importance.

Furthermore, the high-resolution RDE simulations in this work enabled the extraction of time-averaged profiles relative to the wave front. It is shown that the peak pressure at the wave is significantly reduced due to the pre-heated mixture ahead of the wave. This would cause lower pressures after the wave, which will impact the net work that can be extracted from the system. It is also shown that the heat release rate distribution is extended before the shock front.

In summary, the analysis conducted in this work provides an unprecedented understanding of the dynamics of the RDE system that cannot be obtained using simplified simulations or even with the state-of-the-art experiments.

7.2 Future Challenges and Recommendations

This study provides a comprehensive data set to the RDE community to accelerate the design process. There is a need for a research strategy moving forward. Below, immediate research paths which were not pursued here due to time limitations are outlined.

7.2.1 Nozzle Exit Effect on the Dynamics in the Chamber

Most of the studies are conducted with the constant area ratio from the bottom of the detonation chamber to the exit. For a practical design, considering a nozzle geometry at the exit of the chamber is important for extracting thrust from the system. However, a nozzle geometry also would cause the pressure reflection from the exit that would contaminate the flow-field in the chamber. Furthermore, if a nozzle at the exit reaches the choke condition, the mass flow rate from the exit is restricted that might push back the gases in the chamber into the plenum system. In other words, there is a possibility that flashback is caused by a nozzle geometry that is attached at the exit. Investigating this nozzle effect is critical not only to improve the performance of the RDEs but also to ensure safe operation.

7.2.2 Liquid Fuel Effect on the Detonation Structure in RDEs

For aeronautical applications of RDEs, liquid fuel will need to be used due its higher energy density. Liquid fuel will add additional complexity to the RDE dynamics as follows: 1) the diameter of the droplet will affect the detonabilty. Therefore, efficient injection method needs to be investigated to understand the impact of droplets on RDE stability; 2) a wide distribution of droplet diameters will locally alter the evaporation rate, fuel-air ratio, and the deflagration characteristics. In order to account for these effects, multi-phase description of the flow is necessary. Moreover, models for interaction of shock waves with liquid fuel jets are necessary.

7.2.3 NOx production in RDE systems

In general, RDEs generate higher fluid temperature inside the combustor. Since NOx formation is highly sensitive to temperature, it is feasible that RDEs will generate much higher amount of pollutants compared to conventional gas turbines. Prior studies using simplied geometries have concluded that such pollutant formation is minimal. However, those studies did not include the impact of turbulent mixing, and the presence of parasitic combustion regions that can promote such nitrogen oxidation through high residence time and comparatively large temperatures. As a result, a detailed understanding of the NOx generation process in realistic RDEs is critical.

7.3 Outlook

Although the design process has so far been reliant on expensive experimental campaigns, the availability of predictive computational tools can vastly accelerate the optimization of such complex devices. In this context, massively parallel codes that can leverage emerging supercomputing architectures can result in fast turnaround times of less than a few hours for even complex geometries. The next generation of supercomputers will utilize graphics processing units (GPUs) as the main computing unit. Since such GPUs use fundamentally different architecture compared to conventional computers, it is necessary to rethink CFD tools for such new systems. At the same time, the availability of such vast computational resources provide an opportunity to extend computing beyond forward predictions at pre-defined operating conditions. In fact, the entire design process can be constructed on the supercomputers by exploring the design space in an efficient manner.

At the same time, there are still considerable differences between experiments and simulations, as demonstrated in Chapters IV-VI. This suggests that additional efforts into understanding measurement errors, grid convergence, and chemistry model effects are necessary. Due to the harsh conditions inside RDEs, limited measurements are possible. As a result, a closely linked program that combines experimental and computational studies is necessary to advance RDE design.

Radical changes to gas turbines is necessary to counter the growing environmental threat, and addressing the issue of carbon-neutral sustainability. The detonation cycle and the RDE provide a near term solution for this globally important problem.

BIBLIOGRAPHY

BIBLIOGRAPHY

[1] Zhou, R., Wu, D., and Wang, J., "Progress of Continuously Rotating Detonation Engines," *Chinese Journal of Aeronautics*, Vol. 29, No. 1, 2016, pp. 15–29.

[2] Kailasanath, K., "Review of Propulsion Applications of Detonation Waves," *AIAA Journal*, Vol. 38, No. 9, 2000, pp. 1698–1708.

[3] Rankin, B. A., Richardson, D. R., Caswell, A. W., Naples, A. G., Hoke, J. L., and Schauer, F. R., "Chemiluminescence Imaging of an Optically Accessible Non-premixed Rotating Detonation Engine," *Combustion and Flame*, Vol. 176, 2017, pp. 12–22.

[4] Chacon, F. and Gamba, M., "Development of an optically accessible continuous wave Rotating Detonation Engine," *2018 AIAA Aerospace Sciences Meeting*, 2018, p. 0405.

[5] Cho, K. Y., Codoni, J. R., Rankin, B. A., Hoke, J., and Schauer, F., "High-Repetition-Rate Chemiluminescence Imaging of a Rotating Detonation Engine," AIAA Paper 2016-1648, (2016).

[6] Chacon, F. and Gamba, M., "OH PLIF Visualization of an Optically Accessible Rotating Detonation Combustor," AIAA Paper, 2019-4217, (2019).

[7] Schwer, D. A. and Kailasanath, K., "Assessment of Rotating Detonation Engines with Fuel Blends," AIAA Paper 2017-4942, July 2017.

[8] Batten, P., Clarke, N., Lambert, C., and Causon, D. M., "On the choice of wavespeeds for the HLLC Riemann solver," *SIAM Journal on Scientific Computing*, Vol. 18, No. 6, 1997, pp. 1553–1570.

[9] Daily, J. W., "Laser induced fluorescence spectroscopy in flames," *Prog. Energy and Combust. Science*, Vol. 23, No. 2, 1997, pp. 133–199.

[10] Shepherd, J. E. and Kasahara, J., "Analytical Models for the Thrust of a Rotating Detonation Engine," *California Institute of Technology, GALCIT Report FM2017.001*, 2017.

[11] Lu, F. and Braun, E. M., "Rotating Detonation Wave Propulsion: Experimental Challenges, Modeling, and Engine Concepts," *Journal of Propulsion and Power*, Vol. 30, No. 5, 2014, pp. 1125–1142.

[12] Schwinn, K., Gejji, R., Kan, B., Sardeshmukh, S., Heister, S., and Slabaugh, C. D., "Self-sustained, high-frequency detonation wave generation in a semi-bounded channel," *Combustion and Flame*, Vol. 193, 2018, pp. 384–396.

[13] Wolański, P., "Application of the continuous rotating detonation to gas turbine," *Applied Mechanics and Materials*, Vol. 782, Trans Tech Publ, 2015, pp. 3–12.

[14] Wolański, P., Kalina, P., Balicki, W., Rowiński, A., Perkowski, W., Kawalec, M., and Łukasik, B., "Development of gasturbine with detonation chamber," *Detonation Control for Propulsion*, Springer, 2018, pp. 23–37.

[15] Stechmann, D. P., Heister, S. D., and Sardeshmukh, S. V., "High-pressure Rotating Detonation Engine Testing and Flameholding Analysis with Hydrogen and Natural Gas," AIAA Paper 2017-1931, (2017).

[16] Bykovskii, F. A., Zhdan, S. A., and Vedernikov, E. F., "Continuous Spin Detonations," *Journal of Propulsion and Power*, Vol. 22, No. 6, 2006, pp. 1204.

[17] Frolov, S., Dubrovskii, A., and Ivanov, V., "Three-dimensional numerical simulation of the operation of a rotating-detonation chamber with separate supply of fuel and oxidizer," *Russian Journal of Physical Chemistry B*, Vol. 7, No. 1, 2013, pp. 35–43.

[18] Heiser, W. H. and Pratt, D. T., "Thermodynamic cycle analysis of pulse detonation engines," *Journal of Propulsion and Power*, Vol. 18, No. 1, 2002, pp. 68–76.

[19] Kailasanath, K., "Recent Developments in the Research on Pulse Detonation Engines," *AIAA Journal*, Vol. 41, No. 2, 2003, pp. 145–159.

[20] Lisanti, J. C. and Roberts, W. L., "Design of an Actively Valved and Acoustically Resonant Pulse Combustor for Pressure-gain Combustion Applications," AIAA Paper 2016-0899, January 2016.

[21] Kailasanath, K., "The Rotating-detonation-wave Engine Concept: a Brief Status Report," AIAA Paper 2011-580, January 2011.

[22] Kasahara, J. and Frolov, S., "Present status of pulse and rotating detonation engine research," *25th international colloquium on the dynamics of explosions and reactive systems, paper*, Vol. 304, 2015.

[23] Chacon, F. and Gamba, M., "Detonation Wave Dynamics in a Rotating Detonation Engine," AIAA Paper 2019-0198, (2019).

[24] Prakash, S., Raman, V., Lietz, C., Hargus, W. A., and Schumaker, S. A., "High Fidelity Simulations of a Methane-Oxygen Rotating Detonation Rocket Engine," *AIAA Scitech 2020 Forum*, 2020.

[25] Gaillard, T., Davidenko, D., and Dupoirieux, F., "Numerical optimisation in non reacting conditions of the injector geometry for a continuous detonation wave rocket engine," *Acta Astronautica*, Vol. 111, 2015, pp. 334–344.

[26] Wilhite, J., Driscoll, R. B., St. George, A. C., Anand, V., and Gutmark, E. J., "Investigation of a Rotating Detonation Engine Using Ethylene-air Mixtures," AIAA Paper 2016-1650, January 2016.

[27] Anand, V. and Gutmark, E., "Rotating detonation combustors and their similarities to rocket instabilities," *Prog. Energy and Combust. Science*, Vol. 73, 2019, pp. 182–234.

[28] Wolański, P., "Detonative propulsion," *Proc. Combust. Inst.*, Vol. 34, No. 1, 2013, pp. 125–158.

[29] Bluemner, R., Bohon, M. D., Paschereit, C. O., and Gutmark, E. J., "Experimental study of reactant mixing in model rotating detonation combustor geometries," *Flow, Turbulence and Combustion*, Vol. 102, No. 2, 2019, pp. 255–277.

[30] Anand, V., George, A. S., and Gutmark, E., "Amplitude modulated instability in reactants plenum of a rotating detonation combustor," *International Journal of Hydrogen Energy*, Vol. 42, No. 17, 2017, pp. 12629 –12644.

[31] Nakagami, S., Matsuoka, K., Kasahara, J., Matsuo, A., and Funaki, I., "Experimental study of the structure of forward-tilting rotating detonation waves and highly maintained combustion chamber pressure in a disk-shaped combustor," *Proc. Combust. Inst*, Vol. 36, No. 2, 2017, pp. 2673–2680.

[32] Rankin, B. A., Fotia, M. L., Naples, A. G., Stevens, C. A., Hoke, J. L., Kaemming, T. A., Theuerkauf, S. W., and Schauer, F. R., "Overview of performance, application, and analysis of rotating detonation engine technologies," *Journal of Propulsion and Power*, 2016, pp. 131–143.

[33] Chacon, F. and Gamba, M., "Study of Parasitic Combustion in an Optically Accessible Continuous Wave Rotating Detonation Engine," AIAA Paper, 2019-0473, (2019).

[34] Chacon, F., Duvall, J., and Gamba, M., "Evaluation of pressure rise and oscillation in a rotating detonation engine," AIAA Paper 2018-0405, (2018).

[35] Kindracki, J., Wolański, P., and Gut, Z., "Experimental research on the rotating detonation in gaseous fuels–oxygen mixtures," *Shock waves*, Vol. 21, No. 2, 2011, pp. 75–84.

[36] Prakash, S. and Raman, V., "The effects of mixture preburning on detonation wave propagation," Submitted to Proceedings of the Combustion Institute.

[37] Prakash, S., Fiévet, R., Raman, V., Burr, J., and Yu, K. H., "Analysis of the Detonation Wave Structure in a Linearized Rotating Detonation Engine," *AIAA Journal*, 2019, pp. 1–15.

[38] Wolański, P., "Rotating detonation wave stability," 23rd 23rd International Colloquium on the Dynamics of Explosions and Reactive Systems, (2011).

[39] Sato, T., Chacon, F., Gamba, M., and Raman, V., "Mass flow rate effect on a rotating detonation combustor with an axial air injection," Submitted to Shock Waves, 2019.

[40] Zhou, R., Wu, D., and Wang, J., "Progress of Continuously Rotating Detonation Engines," *Chinese J. of Aero.*, Vol. 29, No. 1, 2016, pp. 15 – 29.

[41] Cocks, P. A. T., Bruno, C., Donohue, J. M., and Haas, M., "IDDES of a Dual-Mode Ethylene Fueled Cavity Flameholder with an Isolator Shock Train," *51st AIAA Aerospace Sciences Meeting*, No. AIAA-2013-0116, 2013.

[42] Schwer, D. and Kailasanath, K., "Numerical investigation of the physics of rotating-detonation-engines," *Proceedings of the Combustion Institute*, Vol. 33, No. 2, 2011, pp. 2195–2202.

[43] Oran, E. S., Weber., J. W., Stefaniw, E. I., Lefebvre, M. H., and Anderson., J. D., "A Numerical Study of a Two-Dimensional H2-O2-Ar Detonation Using a Detailed Chemical Reaction Model," *Combust. Flame*, Vol. 113, No. 1–2, 1998, pp. 147 – 163.

[44] Boris, J. P. and Book, D. L., "Flux-corrected transport. I. SHASTA, a fluid transport algorithm that works," *J. Comput. Phys*, Vol. 11, No. 1, 1973, pp. 38 – 69.

[45] Yang, B. and Pope, S. B., "An Investigation of the Accuracy of Manifold Methods and Splitting Schemes in the Computational Implementation Combustion Chemistry," *Combust. Flame*, Vol. 112, 1998, pp. 16.

[46] Clifford, L., Milne, A., TurÃ¡nyi, T., and Boulton, D., "An Induction Parameter Model for Shock-Induced Hydrogen Combustion Simulations," *Combust. Flame*, Vol. 113, No. 1â2, 1998, pp. 106 – 118.

[47] Schwer, D. and Kailasanath, K., "Fluid Dynamics of Rotating Detonation Engines with Hydrogen and Hydrocarbon Fuels," *Proc. Combust. Inst.*, Vol. 34, No. 2, 2013, pp. 1991–1998.

[48] LeVeque, R. J., *Finite Volume Methods for Hyperbolic Problems*, Cambridge University Press, 2002.

[49] Masselot, D., Fiévet, R., and Raman, V., "Effect of Equivalence Ratio and Turbulence Fluctuations on the Propagation of Detonations," AIAA Paper 2017-0374, January 2017.

[50] Wolański, P., "Detonative propulsion," *Proceedings of the Combustion Institute*, Vol. 34, No. 2, 2013, pp. 125–158.

[51] Meng, L. and Jian-Ping, W., "Three Dimensional Simulation for the Effects of Fuel Injection Patterns in Rotating Detonation Engine," *23rd ICDERS*, 2011.

[52] Cocks, P. A., Holley, A. T., and Rankin, B. A., "High Fidelity Simulations of a Non-premixed Rotating Detonation Engine," AIAA Paper 2016-0125, 2016.

[53] Yellapantual, S., Tangirala, V., Singh, K., and Haynes, J., "A numerical study of H2-air rotating detonation combustor," *26th International Colloquium on the Dynamics of Explosions and Reactive Systems*, 2017.

[54] Yi, T.-H., Lou, J., Turangan, C., Choi, J.-Y., and Wolanski, P., "Propulsive performance of a continuously rotating detonation engine," *J. Propul. Power*, Vol. 27, No. 1, 2011, pp. 171–181.

[55] Schwer, D. and Kailasanath, K., "Feedback into mixture plenums in rotating detonation engines," *50th AIAA Aerospace Sciences Meeting*, 2012, p. 617.

[56] Eude, Y., Davidenko, D., Falempin, F., and Gökalp, I., "Use of the adaptive mesh refinement for 3D simulations of a CDWRE (continuous detonation wave rocket engine)," *17th AIAA International Space Planes and Hypersonic Systems and Technologies Conference*, 2011, p. 2236.

[57] Yee, H. C., "A class of high resolution explicit and implicit shock-capturing methods," 1989.

[58] Toro, E. F., Spruce, M., and Speares, W., "Restoration of the contact surface in the HLL-Riemann solver," *Shock Waves*, Vol. 4, No. 1, 1994, pp. 25–34.

[59] "The Open Source CFD Toolbox http://openfoam.org," 2016.

[60] Van Leer, B., "Towards the ultimate conservative difference scheme. V. A second-order sequel to Godunov's method," *J. Comput. Phys.*, Vol. 32, No. 1, 1979, pp. 101–136.

[61] Greenshields, C. J., Weller, H. G., Gasparini, L., and Reese, J. M., "Implementation of Semi-discrete, Non-staggered Central Schemes in a Colocated, Polyhedral, Finite Volume Framework, for High-speed Viscous Flows," *International J. for Numerical Methods in Fluids*, Vol. 63, No. 1, 2010, pp. 1–21.

[62] Goodwin, D. G., Moffat, H. K., and Speth, R. L., "Cantera: an object-oriented software toolkit for chemical kinetics, thermodynamics, and transport processes," https://www.cantera.org, 2017. Version 2.3.0.

[63] Powers, J. and Paolucci, S., "Accurate spatial resolution estimates for reactive supersonic flow with detailed chemistry," *AIAA JOURNAL*, Vol. 43, No. 5, MAY 2005, pp. 1088–1099, AIAA 43rd Aerospace Sciences Meeting and Exhibit, Reno, NV, JAN 10-13, 2005.

[64] Shimizu, H., Tsuboi, N., and Hayashi, A., "Study of detailed chemical reaction model on hydrogen–air detonation," *39th AIAA aerospace sciences meeting and exhibit, Reno, AIAA paper*, Vol. 478, 2001, p. 2001.

[65] Irvin Glassman, Richard A. Yetter, N. G. G., *Combustion*, 5th Edition, Academic Press, New York, 2014.

[66] Jachimowski, C. J., "Analytical study of the hydrogen-air reaction mechanism with application to scramjet combustion," Tech. rep., National Aeronautics and Space Administration, Hampton, VA (USA). Langley Research Center, 1988.

[67] Varatharajan, B. and Williams, F., "Ethylene Ignition and Detonation Chemistry, Part 2: Ignition Histories and Reduced Mechanisms," *Journal of Propulsion and Power*, Vol. 18, No. 2, 2002, pp. 352–362.

[68] Petersen, E. L. and Hanson, R. K., "Reduced kinetics mechanisms for ram accelerator combustion," *Journal of Propulsion and power*, Vol. 15, No. 4, 1999, pp. 591–600.

[69] Schwer, D. and Kailasanath, K., "Numerical investigation of rotating detonation engines," *46th AIAA/ASME/SAE/ASEE Joint Propulsion Conference & Exhibit*, 2010, p. 6880.

[70] Schwer, D. A., Corrigan, A. T., and Kailasanath, K., "Towards Efficient, Unsteady, Three-dimensional Rotating Detonation Engine Simulations," AIAA Paper 2014-1014, January 2014.

[71] Burr, J. and Yu, K., "Detonation Wave Propagation in an Open Channel with Transverse Jets," AIAA Paper 2017-4908. (2017).

[72] Yao, S., Liu, M., and Wang, J., "Numerical Investigation of Spontaneous Formation of Multiple Detonation Wave Fronts in Rotating Detonation Engines," *Combustion Science and Technology*, Vol. 187, No. 12, 2015, pp. 1867–1878.

[73] Sato, T., Voelkel, S., and Raman, V., "Detailed Chemical Kinetics Based Simulation of Detonation-Containing Flows," American Society of Mechanical Engineers, Paper GT2018-75878, June (2018).

[74] Sato, T. and Raman, V., "Analysis of Detonation Structures with Hydrocarbon Fuels for Rotating Detonation Engines Applications," 2019, Submitted to Journal of Propulsion and Power.

[75] Sato, T., Chacon, F., White, L., Raman, V., and Gamba, M., "Mixing and detonation structure in a rotating detonation engine with an axial air inlet," Submitted to Proc. Combust. Int., 2019.

[76] Sato, T. and Raman, V., "Detonation Structure in Ethylene/Air-based Non-premixed Rotating Detonation Engine," Submitted to Journal of Propulsion and Power.

[77] Sato, T., Fabian, C., James, D., Mirko, G., and Venkat, R., "Dynamics of rotating detonation engines with a pintle-type injector," Dynamics of rotating detonation engines with a pintle-type injector, 24th ISABE Conference, (2019).

[78] Sato, T., Voelkel, S., and Raman, V., "Analysis of Detonation Structures with Hydrocarbon Fuels for Application Towards Rotating Detonation Engines," Analysis of detonation structures with hydrocarbon fuels for application towards rotating detonation engines, AIAA Paper 2018-4965, 2018, AIAA Paper 2018-4965, 2018.

[79] Lietz, C., Desai, Y., Munipalli, R., Schumaker, S. A., and Sankaran, V., "Flowfield analysis of a 3D simulation of a rotating detonation rocket engine," Flowfield analysis of a 3D simulation of a rotating detonation rocket engine, AIAA Paper, 2019-1009, 2019, AIAA Paper, 2019-1009, 2019.

[80] Prakash, S., Fiévet, R., and Raman, V., "The Effect of Fuel Stratification on the Detonation Wave Structure," AIAA Paper 2019-1511, (2019).

[81] Zhou, R. and Wang, J.-P., "Numerical investigation of flow particle paths and thermodynamic performance of continuously rotating detonation engines," *Combustion and Flame*, Vol. 159, No. 12, 2012, pp. 3632–3645.

[82] Hayashi, A. K., Kimura, Y., Yamada, T., Yamada, E., Kindracki, J., Dzieminska, E., Wolanski, P., Tsuboi, N., Tangirala, V., and Fujiwara, T., "Sensitivity analysis of rotating detonation engine with a detailed reaction model," AIAA Paper 2009-0633, (2009).

[83] Lietz, C., Desai, Y., Hargus, W. A., and Sankaran, V., "Parametric investigation of rotating detonation rocket engines using large eddy simulations," AIAA Paper, 2019-4129, (2019).

[84] Li, C., Kailasanath, K., and Oran, E. S., "Detonation Structures Behind Oblique Shocks," *Physics of Fluids*, Vol. 6, No. 4, 1994, pp. 1600–1611.

[85] Varatharajan, B., Petrova, M., Williams, F., and Tangirala, V., "Two-step Chemical-kinetic Descriptions for Hydrocarbon–oxygen-diluent Ignition and Detonation Applications," *Proceedings of the Combustion Institute*, Vol. 30, No. 2, 2005, pp. 1869–1877.

[86] Marcantoni, L. G., Tamagno, J., and Elaskar, S., "Two-dimensional Numerical Simulations of Detonation Cellular Structures in H2O2Ar Mixtures with OpenFOAM®," *International Journal of Hydrogen Energy*, Vol. 42, No. 41, 2017, pp. 26102–26113.

[87] Chong, S. T., Hassanaly, M., Koo, H., Mueller, M. E., Raman, V., and Geigle, K.-P., "Large Eddy Simulation of Pressure and Dilution-jet Effects on Soot Formation in a Model Aircraft Swirl Combustor," *Combustion and Flame*, Vol. 192, 2018, pp. 452–472.

[88] Chong, S. T., Raman, V., Mueller, M. E., and Im, H. G., "The Role of Recirculation Zones in Soot Formation in Aircraft Combustors," American Society of Mechanical Engineers, Paper GT2018-76217, June 2018.

[89] Prakash, S., Fievet, R., and Raman, V., "The Effect of Fuel Stratification on the Detonation Wave Structure," AIAA Paper 2019-1511, (2019).

[90] Ye-Tao, S. and Jian-Ping, W., "Change in Continuous Detonation Wave Propagation Mode from Rotating Detonation to Standing Detonation," *Chinese Physics Letters*, Vol. 27, No. 3, 2010, pp. 034705.